

Diss. ETH No. 16037

Control-Oriented Modeling of NO Emissions of SI Engines

A dissertation submitted to the
SWISS FEDERAL INSTITUTE OF TECHNOLOGY
ZÜRICH

for the degree of
Doctor of Technical Sciences

presented by
Daniel Brand
Dipl. Masch.-Ing. ETH

born 2. March 1973
citizen of Trachselwald BE

accepted on the recommendation of
Prof. Dr. L. Guzzella, examiner
Prof. Dr. K. Boulouchos, co-examiner

2005

contact: daniel.brand@alumni.ethz.ch

L^AT_EX2 ϵ

page size: DIN A5

documentclass: book

standard character size: 10 pt

packages: amsmath, caption, graphicx, harvard, here,

latexsym, natbib, epsfig, supertab

Daniel Brand

2005

ISBN 3-9522686-4-X

To Miranda, with love

Preface

This thesis is based on my research performed at the Measurement and Control Laboratory of the Swiss Federal Institute of Technology (ETH) in Zurich between 2000 and 2005. Part of the work was funded by DaimlerChrysler AG, Germany.

I wish to thank my advisor, Professor Dr. Lino Guzzella, for the initiation of the project and the support throughout the course of my work at the Laboratory. Thanks are further due to Dr. Chris Onder for his most valuable support.

Furthermore, I would like to thank Professor Dr. Konstantinos Boulouchos for accepting to be my co-examiner and for his much appreciated advice. I am grateful to Professor Dr. Lars Eriksson. He provided me many helpful hints and programming tools, which proved to be very useful throughout my work.

I wish to express my appreciation to Heinz Neumann, Rainer Müller, and Ulrich Springer and to the DaimlerChrysler AG for the financial and technical support.

I owe a lot to the staff at the Measurement and Control Laboratory, in particular to Daniel Matter, Oskar Brachs, Hansueli Honegger, and Jan Prikryl for their help with the test bench hardware. Special

thanks go to Brigitte Rohrbach for reviewing the text and for the many suggestions that helped to make it more consistent. I am also grateful to Claudia Wittwer who managed all the administrative issues.

Most importantly, I would like to express my gratitude to my friends at the Laboratory who helped with fruitful discussions. Their friendship made the time at the Swiss Federal Institute most enjoyable. In particular I would like to name Peter Spring, Simon Frei, Ognyan Yanakiev, André Niederberger, and Antonio Sciarretta.

This thesis could not have been accomplished without the support of my parents throughout all the years.

Contents

Abstract	xii
Zusammenfassung	xiv
Abbreviations, Acronyms, Symbols, Subscripts	xxi
1 Introduction	1
1.1 Motivation	1
1.2 Formation of NO in IC Engines	3
1.3 Previous Work	8
1.4 Objectives	11
1.5 Contributions of the Thesis	11
1.6 Approach	12
1.7 Organization of the Text	19
2 Experiments	21
2.1 Engine and Test Bench Hardware	21
2.2 Data Acquisition	23
2.3 Operating Points	25
2.4 Data Sets	25

3	In-Cylinder Pressure	29
3.1	Heat-Release Profile	32
3.2	In-Cylinder Pressure	43
3.3	Crankshaft and Piston Model	45
3.4	Phase of the Angular Velocity	47
3.5	Calibration	50
3.6	Flame Speed Correction	50
3.7	Comparison to Sliding Mode Observer (SMO)	64
4	Burned Gas Temperature	75
4.1	Reference Process Simulation	75
4.2	Control-Oriented Model	85
5	NO Formation	103
5.1	Extended Zeldovich Mechanism	104
5.2	Equilibrium Assumption	104
5.3	Simplified ODE	106
5.4	Steady-state Validation	109
6	Calculation Time	119
6.1	Organization of the Calculations	119
6.2	Real Time	120
6.3	Detailed Calculation Time	121
7	Summary and Conclusions	123
A	Step-by-Step Calibration	125
A.1	Required Experimental Data	125
A.2	Calibration Procedure	127
B	Heat-release Analysis	131

C	Thermodynamic Properties	137
C.1	Properties of a Single Species	139
C.2	Mole and Mass Specific Properties	140
C.3	Gibbs Function	141
C.4	Atom Balance	142
C.5	Composition of the Gas	144
C.6	Sensitivity of the Equilibrium Composition	146

Abstract

Beginning with the first emission legislation for cars in California in the early 1970s the combination of stoichiometric combustion and exhaust gas aftertreatment using the three-way catalytic converter (TWC) became predominant. That concept enabled the industry to stay within the limits imposed by the increasingly demanding emission legislation throughout the world until today and it holds still further potential to comply with even more stringent laws to come.

The oil price shock in the mid-1970s and an increasing general awareness for environmental issues directed engine research towards the search for improvements in fuel efficiency. A key to improved fuel efficiency is the reduction of the throttling losses, for instance by running the engine at lean fuel/air equivalence ratios.

However, allowing the engine to run at off-stoichiometric operation requires new, more complex exhaust gas aftertreatment systems to comply with the constraints set by the emission legislation. Common to many of the new aftertreatment systems is the need for exact information on the exhaust gas composition for efficient control of the system.

The contribution of this thesis is to provide a physics-based control-oriented model for the estimation of the engine-out NO emission. The approach consists of (a) mapping the model parameters at nominal

operating conditions and (b) calculating the engine-out NO emissions in the neighborhood of the nominal operating conditions based on the model. The model uses the feedback of the crankshaft angular velocity for the adaption of the model parameters.

The model reflects all essential influences on the NO formation, while the simulation time was reduced to about 15 milliseconds on a standard PC¹. This makes it possible to estimate the engine-out NO emission for each cycle in parallel to the experiment for engine speeds as high as 6000 rpm. The estimated NO emissions are available with a time delay of one engine cycle, which is less than the transport delay of the exhaust gas from the exhaust port to the exhaust gas aftertreatment system.

The model has been validated using measured data obtained from a V6 3.2-liter SI engine. The model shows good accuracy in a large operating range.

¹Pentium 4, 2.2 GHz processor

Zusammenfassung

Beginnend mit der ersten Emissionsgesetzgebung in Kalifornien in den frühen 70er Jahren hat sich die Kombination von stöchiometrischem Betrieb des Ottomotors und der Abgasreinigung durch den 3-Wege-Katalysator weltweit durchgesetzt. Dieses Konzept war geeignet, mit den immer strenger werdenden Gesetzgebungen Schritt zu halten. Es birgt heute noch genügend Potenzial, um zukünftigen Anforderungen an das Emissionsverhalten genügen zu können.

Die Ölkrise und ein generell steigendes Bewusstsein für Fragen des Umweltschutzes lenkten die Anstrengungen der Forschung auf die Steigerung des Wirkungsgrades von Verbrennungsmotoren. Ein geeignetes Mittel dazu ist die Entdrosselung des Motors, zum Beispiel indem der Motor bei magerem Luft-Brennstoffverhältnis betrieben wird.

Allerdings müssen bei nicht-stöchiometrischem Betrieb des Ottomotors neue, komplexere Abgasreinigungssysteme zum Einsatz kommen, damit die Emissionsgrenzwerte weiterhin eingehalten werden können. Eine Gemeinsamkeit dieser neuen Systeme ist, dass die Zusammensetzung der Abgase bekannt sein muss, um einen effizienten Betrieb des Abgasreinigungssystems sicherstellen zu können.

Der Beitrag der vorliegenden Dissertation ist ein physikbasiertes Modell für die Schätzung der NO-Rohemissionen eines Ottomotors.

Das Vorgehen besteht aus den folgenden zwei Schritten: (a) Die Parameter des Modells werden für eine Anzahl Referenzbetriebspunkte kalibriert. (b) In der Umgebung der Referenzbetriebspunkte werden die NO-Emissionen mit Hilfe des Modells berechnet. Das Modell benutzt die gemessene instationäre Kurbelwellendrehzahl für die Parameteradaption.

Das Modell bildet alle relevanten Einflüsse auf die NO-Bildung ab. Es wurde aber soweit vereinfacht, dass die Simulationszeit etwa 15 Millisekunden auf einem heute üblichen PC beträgt². Dies ermöglicht es, das Modell parallel zum Experiment laufen zu lassen und zwar bis zu einer Motordrehzahl von 6000 Umdrehungen pro Minute. Die Resultate des Modells liegen mit einer Zeitverzögerung von einem Verbrennungszyklus vor, was weniger ist als die Transportzeit des Abgases vom Auslass bis zum Abgasreinigungssystem.

Für die Validierung wurden gemessene Daten von einem 3.2-Liter V6 Ottomotor verwendet. Das Modell zeigt eine hohe Genauigkeit in einem grossen Betriebsbereich.

²Pentium 4, 2.2 GHz Prozessor

Nomenclature

Abbreviations, Acronyms, Names

BDC	bottom dead center
ca	crank angle
deg	degree
DFT	discrete Fourier transformation
DSP	digital signal processor
EGR	exhaust gas recirculation
IC	initial condition
ivc	inlet valve close
NEDC	new European driving cycle
ODE	ordinary differential equation
PM	particulate matter
PP	peak pressure
PPL	peak pressure location
rpm	revolutions per minute
sa	spark advance

SI	spark ignition
SMO	sliding mode observer
TDC	top dead center
TWC	three-way catalytic converter

Decorations

\hat{x}	estimated values of the quantity x
x^0	reference value of the quantity x
[]	concentration measured in kmol m^{-3}
$\langle \rangle$	concentration measured in ppm

Subscripts

b	burned
e	equilibrium
em	exhaust manifold
f	fuel
fr	fresh gas
im	inlet manifold
r	reciprocating, residual gas
u	unburned

Symbols

A	amplitude, reaction constant
a	constant in the Vibe function, constant proportional to the burned mass, adaption-activation flag

A_p	piston surface area
B	bore, reaction constant
b	constant proportional to the unburned mass
C, C', C''	constants
C_0, C_1, C_2	constants in Woschni's heat transfer correlation
c_e	equilibrium concentration
c_m	mean piston speed
c_v	mass specific heat capacity at constant volume
c_p	mass specific heat capacity at constant pressure
$c_{\Delta p}$	pressure compensation for the change of the combustion phasing
$c_{\Delta T_{ad}}$	temperature compensation for the change of the combustion phasing
C_φ	phase shift
D, D', D''	constants
d	disturbance
d_{min}	minimum distance
E	activation energy
e	piston offset
f	polynomial for the calculation θ_d , function describing the crank-slider kinematics, frequency
f_1, f_2	non-linear system dynamics of the SMO
G	transfer function
G_b, G_d	lumped operating-point dependent constants for the calculation of θ_d, θ_b
g	polynomial for the calculation of θ_b
h	mass specific enthalpy, clearance height

h_c	heat-transfer coefficient
H_b, H_d	lumped geometry constants for the calculation of θ_d, θ_b
I_{cr}	rotational inertia of the crankshaft
J	time-varying rotational inertia, cost function
k	correcting gain of the theoretic adiabatic temperature rise
k_{1+}, k_{2+}, k_{3+}	reaction constants
k_{1-}, k_{2-}, k_{3-}	reaction constants
k_b	correcting gain of the rapid burning angle
k_d	correcting gain of the flame development angle
k_i	integrator gain
K_P	SMO switching gain
k_p	proportional gain
k_{sf}	correcting gain of θ_d and θ_b
K_ω	SMO switching gain
L	length of the connecting rod
L_{tor}	moment arm
M	center of the circle
m	mass
m_v	Vibe function form parameter
n	engine speed, mole number
P, p	in-cylinder pressure
p_f	fired in-cylinder pressure
p_m	motored in-cylinder pressure
p_1	in-cylinder pressure at 80 degrees before TDC
p_2	in-cylinder pressure at 80 degrees after TDC

Q_{ch}, Q_f	heat released by the combustion of the fuel
Q_{ht}	heat transferred to the cylinder wall
Q_{LHV}	lower heating value
R	correlation coefficient, radius, gas constant
R_c	composition rate
\tilde{R}_d	proportional decomposition rate
S	stroke, sensitivity
s	state variable in the adaption rule
S_l	laminar flame speed
T	temperature, torque
T_1	temperature at 80 degrees before TDC
T_{fric}	friction torque
T_{grav}	gravity torque
T_i, T_{ind}	indicated torque
T_l, T_{load}	load torque
T_n	net torque
T_r	torque due to reciprocating masses
T_w	temperature of the cylinder wall
U	internal energy
u	mass specific internal energy
V	volume
V_c	compression volume
V_d	displaced volume
W	work
X	generic signal in the frequency domain
x	position of the piston, generic signal in the time domain
x_b	normalized heat-release profile,

	burned mass fraction
x_r	residual gas mass fraction
α	non-linear gain, constant describing the flame speed
α_1, α_2	Kalman feedback gains
β	constant describing the flame speed
ΔC_φ	calibrated phase difference
ΔT_{ad}	adiabatic temperature rise
$\Delta T_{ad,th}$	theoretic adiabatic temperature rise
$\Delta\theta$	crank angle interval
η	saturation limit
θ	crank angle
θ_{50}	crank angle position when 50% of the mass is burned
θ_{80}	crank angle position when 80% of the combustion time has elapsed
θ_b	rapid burning angle
θ_d	flame development angle
θ_{ce}	combustion end
θ_{cs}	combustion start
θ_{sa}	spark advance
κ	polytropic coefficient
λ_0	gain for non-linear pressure correction
λ_p	$\lambda_p = 2L/S$
μ	dynamic viscosity
ν	kinematic viscosity
ρ	density
τ_r	characteristic reaction time
ϕ	fuel/air equivalence ratio

φ	phase
φ_ω	phase in the spectrum of the crankshaft angular velocity
φ_{T_n}	phase in the spectrum of the net torque
ω	instantaneous crankshaft angular velocity
$\tilde{\omega}$	estimation error of the crankshaft angular velocity

Matrices, Vectors, and Scalar Signals

A	system matrix
C	output matrix
e	error signal
F	system matrix
G	input matrix
H	matrix containing Kalman feedback gains
r	reference signal
u	input signal
x	vector of state variables
y	output signal

Chapter 1

Introduction

Readers who are familiar with the subject of this thesis may skip the introduction or may consider reading the section in which the objectives of the thesis are highlighted (page 11) and in which the organization of the text is detailed (page 19).

1.1 Motivation

There are two main application fields where *control-oriented* models for the estimation of the engine-out NO emissions are desirable: Optimization of the engine operating conditions and real-time applications for control purposes. Additionally, NO models offer information about in-cylinder pressure and temperature.

Optimization of the Engine Operating Conditions

Modern spark-ignited combustion engines may be understood as multiple-input multiple-output systems. The input into the system consists of the throttle angle, the injected fuel mass, the spark advance,

the load torque, etc. The output consists of the torque, the emissions such as CO₂, CO, HC, NO, PM, noise, vibrations, etc.

During engine development and calibration, the overall engine behavior has to be optimized. Usually, the upper limits for emissions such as CO, HC, NO, and PM are given by legislation, while an optimal compromise between high torque, low CO₂ emissions (fuel consumption), low vibrations, and noise has to be found.

An experimental search for this optimum is very time-consuming as the following simple calculation shows: Assume that the NO emissions depend on engine speed, inlet manifold pressure, spark advance, fuel/air equivalence ratio, and EGR rate only. With a choice of five support points for each variable, 3.125 measurements are necessary to determine a complete map for the NO emissions. This immediately shows that a model for the NO emissions is helpful in the search for the desired optimum.

Real-Time Applications

Future control strategies of combustion engines will possibly allow the engine to run at a lean fuel/air equivalence ratio, in order to increase their part load efficiency. But the trade-off costs of these fuel savings include more complex exhaust gas aftertreatment systems, such as NO_x traps. These new exhaust gas aftertreatment systems accumulate the NO emitted from the engine during lean operation. After a certain time period, the accumulator has to be purged. The control of this filling-emptying cycle requires the NO emission data of the engine as input. This is the point at which it is desirable to have a model that delivers on-line calculations of the engine-out NO emissions.

Additional Benefits from an NO Emission Model

As will be shown later in this text, modeling emissions of NO comprises modeling the in-cylinder temperature and pressure. The in-cylinder pressure is of interest for the feedback control of the spark advance, while the in-cylinder temperature is useful for the determination of the engine-out temperature of the exhaust gas.

1.2 Formation of NO in IC Engines

In the literature three different paths for the formation of NO in internal combustion engines are described: (1) Thermal formation of NO, (2) prompt formation of NO, and (3) formation of NO from fuel-bound nitrogen. The dominant part of engine-out NO emissions has been assigned to the thermal formation of NO [34], [13], [12].

The variables controlling the thermal formation of NO are the in-cylinder gas temperature, the availability of oxygen, and the pressure, as well as the residence time in locations with favorable temperatures and oxygen concentrations for the formation of nitric oxides. These variables define the equilibrium concentration of NO as well as the composition and decomposition rates of NO. The equilibrium concentration ranges from 0 to 10'000 ppm for those temperatures and pressures prevailing in the combustion chamber, while the characteristic time constant for NO formation ranges from 10^{-6} to 10^0 seconds (see Figs. 1.1 and 1.2). The characteristic time constant has to be compared to the duration of a typical combustion process, which is on the order of 1 to 10 milliseconds, depending on the engine speed.

During the combustion process, the equilibrium concentration of NO reaches values as high as 6000 ppm. Due to the relatively slow kinetics of the formation of NO, this level is not attained by the NO concentration. Towards the end of the combustion, the equilibrium con-

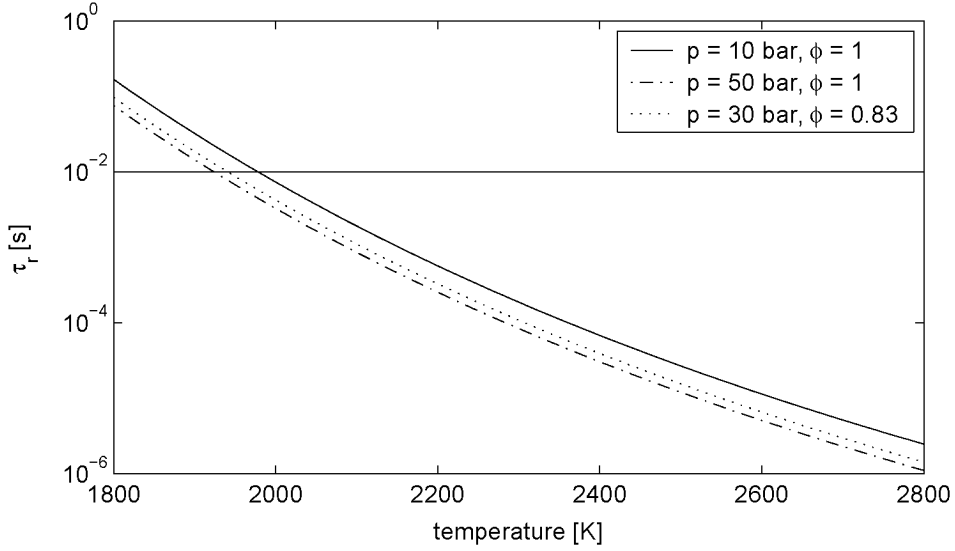


Figure 1.1: Characteristic reaction time of the NO formation. The solid horizontal line at $\tau_r = 10$ ms indicates the duration of a typical combustion process at moderate engine speeds. The data shown is calculated based on [24] and [34]

centration of NO falls to relatively moderate levels due to the falling in-cylinder temperature and pressure. Again, due to the slow NO kinetics, the decomposition of the NO unfortunately does not reach the equilibrium concentration. In fact, as described in [34], the characteristic time constant $\tau_r = \frac{[NO]_e}{d[NO]/dt}$ for the decomposition of NO becomes long enough that the concentration of NO virtually "freezes" at a non-equilibrium concentration. The transient NO equilibrium concentration, the characteristic time constant, and the current NO concentration during a typical combustion are depicted in Fig. 1.3.

Modeling the phenomena described above requires a simulation of the transient thermodynamic process, which takes into account the internal energy of the gas, the piston work, and the heat transfer to the cylinder wall. Due to the high sensitivity of the formation of NO to the temperature of the gas (see Fig. 1.2), the spatial distribution of the temperature has to be modeled as well. This implies that one

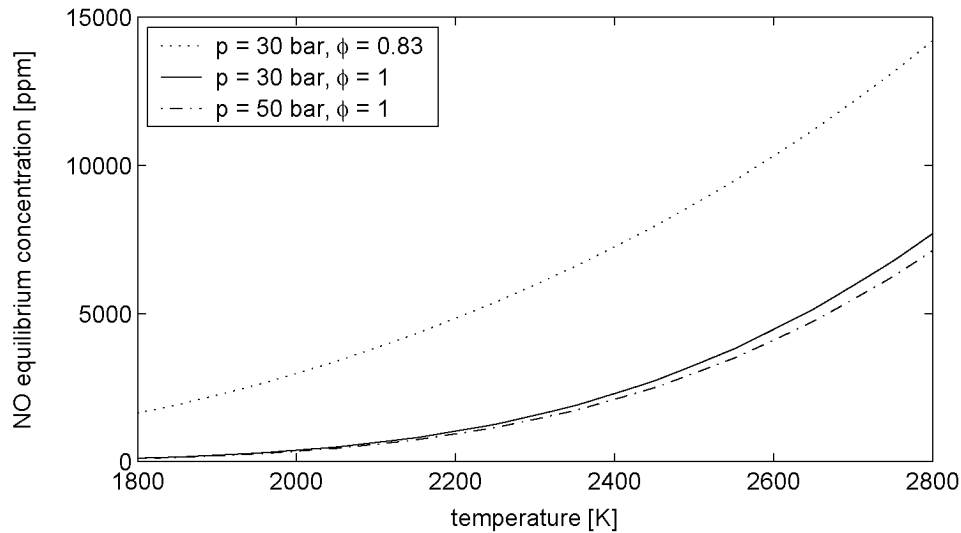
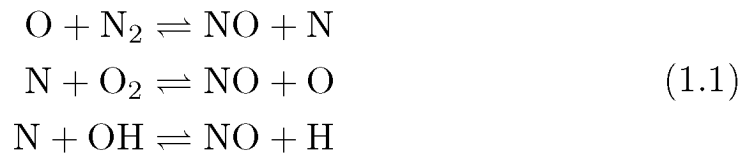


Figure 1.2: NO equilibrium concentrations calculated based on [24]

has to differentiate at least between a zone with burned and a zone with unburned gas. Despite the progress in computational power, the numerical integration of the differential equations describing the thermodynamic and kinetic processes is still time-consuming.

Fortunately, since the relevant reactions for the formation of NO do not release any significant amount of heat, so that the process simulation and the formation of NO may be treated sequentially. The dominant chemical reactions for the thermal NO formation have been found by Zeldovich [65] and Lavoie [43]. They are usually referred to as *Extended Zeldovich Mechanism*.



The concentration levels of the species N, O, OH, and H depend on many other chemical reactions. At least a dozen reactions can be formulated that contribute considerably to the concentrations of

these species. The characteristic time constants of these reactions are short compared to the one of the NO formation. One exception is the formation rate of N, which is comparable to the formation rate of NO. In order to avoid having to find the numerical solution of a large and stiff set of differential equations for the concentrations of the species, it is often assumed that all species except NO and N are at their equilibrium concentration levels. For N, often a small but constant concentration is assumed (N is treated as a "steady-state" species) and for the concentration of NO the three chemical equations of the Extended Zeldovich Mechanism have to be solved.

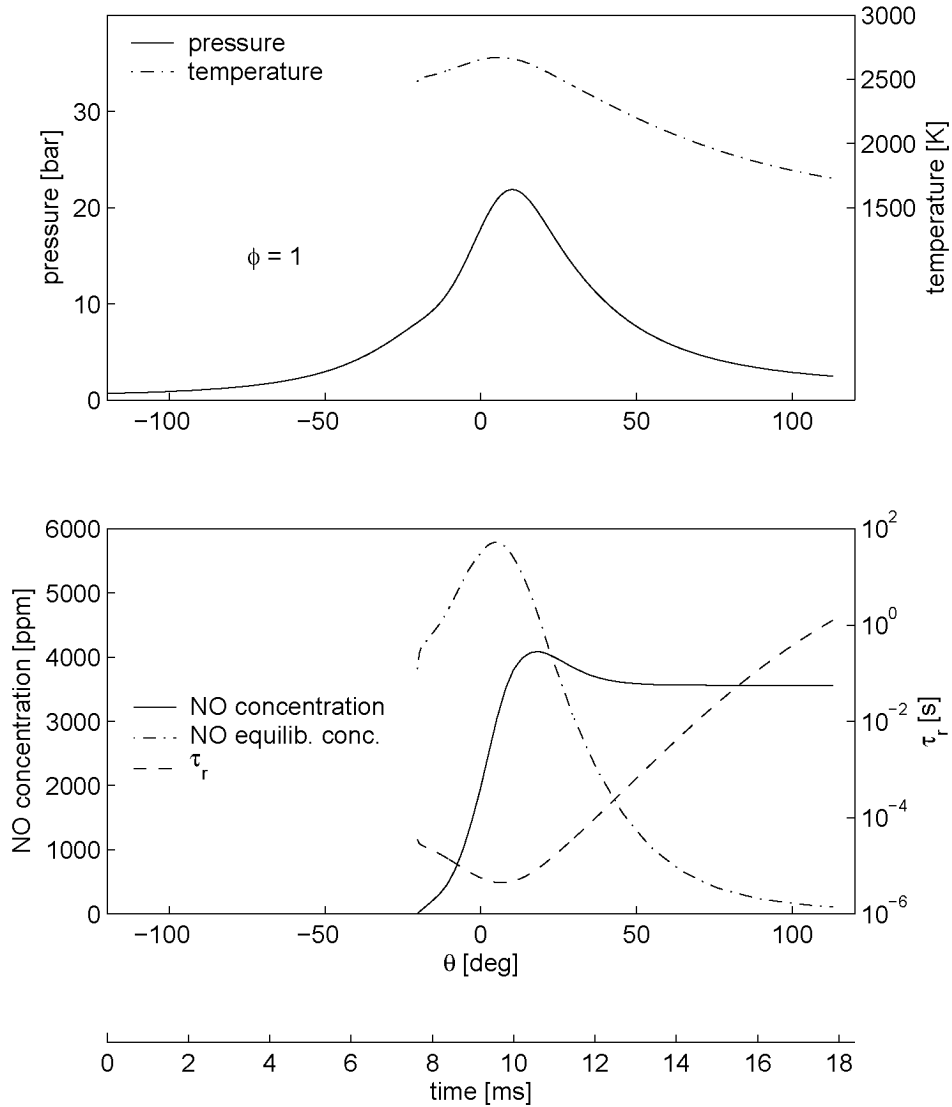


Figure 1.3: The upper graph shows the temperature of the burned gas and the pressure during stoichiometric combustion. The graph at the bottom shows the transient concentration of NO, the equilibrium concentration of NO, and the characteristic time of the NO formation over both the crank angle and time

1.3 Previous Work

As pointed out in Sect. 1.2, modeling of the formation of NO entails cycle simulation and the simulation of the chemical kinetics. This section references previous work done in those fields. The first subsection cites publications that propose NO emission models incorporating both cycle simulation and the chemical kinetics of the NO formation. The second subsection cites publications that contribute to various aspects of NO emission modeling. The citations are not limited to spark-ignition engines, since many aspects apply to the combustion of fuel and air in general.

1.3.1 NO Formation Models for IC Engines

Early work in NO emission modeling for spark-ignition engines was presented in [43], where NO emissions from spark-ignition engines were measured and compared to simulated data. The authors used a 0-dimensional multi-zone model for the pressure and temperature of the cylinder charge. For the chemical kinetics they employed two chemical equations derived in [65] and added a few more equations. Among the equations used in [43], a set of three chemical equations known as Extended Zeldovich Mechanism is recognized as the most important contributor to the formation of engine-out NO emissions. In [11] the findings of [43] were refined and the parameters influencing the NO formation were analyzed. In [41] and [10], NO emission modeling was extended to stratified-charge engines. In [42], various findings of the earlier contributions mentioned above are summarized. A step-by-step description of internal combustion engine modeling can be found in [52].

During the last two decades, many contributions to the modeling of NO emissions of spark-ignition engines using 0-dimensional cycle simulations have been published ([51], [59], [66], [56]).

Growing computational power made it possible to combine models of thermodynamics, fluid dynamics and chemical kinetics. In 1985 KIVA, a code for transient 3-dimensional chemically reactive fluid flows, was published [49]. This code has been used extensively by the scientific community to investigate the interaction between fluid motion, fuel evaporation and combustion chemistry in high temporal and spatial resolution. A large number of investigations have thus been based on the KIVA code (e.g. [21], [1], [39]).

Engine manufacturers demand computationally easily tractable models either for engine calibration or for real-time calculations as part of engine control algorithms. In order to avoid the time-consuming calculations required by the models mentioned above, attempts have been made to calculate the formation of NO based on engine operating parameters or on the basis of features of measured pressure traces using neural networks or similar approaches (e.g. [61], [60], [31], [6], [40]).

1.3.2 Indirect Contributions to Models of NO formation

In-Cylinder Pressure Estimation

The thermodynamic state of the in-cylinder charge is the origin of the engine performance and emissions and is therefore of particular interest. In this context a large amount of work has been done to reconstruct the in-cylinder pressure from measurements of the ion current, the instantaneous crankshaft velocity, or the angular acceleration of the engine block, since direct measurement of the in-cylinder pressure is not feasible (in terms of costs) for production-type engines, as yet.

In [26], [25], and [4] an analytical pressure model and ion current measurements have been used to reconstruct the in-cylinder pressure. In [15] a similar model has been employed together with crankshaft

angular velocity measurements. In [55] and [7] the measurement of the instantaneous crankshaft angular velocity is used together with a pressure model in the frequency domain to obtain the cylinder pressure. In [33] the instantaneous crankshaft angular velocity was used to reconstruct the indicated torque by Kalman filtering. The authors of [57] and [58] use time domain models together with the measured instantaneous crankshaft velocity. Another approach is proposed in [29] and [30], where specific properties of the measured crankshaft velocities are used to combine the pressure trace from a library of base functions. Finally, the authors of [8] propose a model that calculates the in-cylinder pressure from engine block angular acceleration.

Acceleration of the Numerical Simulation

Driven by the demand for fast algorithms for engine calibration or on-line applications, measures have been taken to reduce calculation time for process simulations. In [3] an analytic solution for the mean in-cylinder temperature and pressure is presented. In [22] the mean in-cylinder temperature derived with a 0-dimensional 1-zone model is split into the burned and the unburned gas temperature using the ideal gas law. In [23], [24] two methods for the rapid calculation of the chemical equilibrium are presented.

So far, models that have the potential to run in real-time have been presented for the instantaneous in-cylinder pressure and the mean indicated pressure. Further, models for NO emission prediction are readily available for off-line applications. But there is still the need for easy-to-evaluate, control-oriented models that calculate on-line the engine-out NO emissions based on in-cylinder pressure and temperature. The work presented in this text is to contribute to such a model.

1.4 Objectives

The aim of the work described in this text is to develop an NO emission model for homogenous SI engines, which can be employed for optimization tasks and real-time applications as sketched earlier in this chapter. Particularly, the following goals are pursued:

1. The model captures the influence of engine speed, the inlet manifold pressure, the spark advance, and the fuel/air equivalence ratio on the engine-out NO emissions. Due to its physics-based nature, the model needs little calibration effort.
2. The model has the capability to extrapolate the NO emission behavior of the engine to operating conditions beyond the range of the calibration data set.
3. The model can be evaluated fast enough for real-time¹ applications.
4. The accuracy of the model is comparable to the accuracy of models that are based on maps or adjustable functions (see e.g. [5], [6]).

1.5 Contributions of the Thesis

A physics-based, control-oriented model for the estimation of the engine-out NO emission of a SI engine has been developed. The model captures the influence of engine speed, inlet manifold pressure, spark advance, and fuel/air equivalence ratio on the engine-out NO emissions.

¹In the context of this text, real-time means a model evaluation time of less than approximately 40 ms. The evaluation starts at the end of the cycle for which the NO emissions have to be estimated and is finished before the end of the next cycle. The model runs on a standard PC using MATLAB.

1. In order to compensate for disturbances, the model comprises a new adaption scheme for the instantaneous in-cylinder pressure using the measurement of the instantaneous crankshaft angular velocity.
2. The stability and the robustness of the adaption scheme are verified using the circle criterion.
3. For the estimation of the burned gas temperature, a simplified method has been developed. It relies on the adiabatic flame temperature rather than on the enthalpy and the trapped mass of the gas in the cylinder. This eliminates a source of error common to many process simulations.
4. The NO formation model is derived from the Extended Zeldovich Mechanism. It is simplified such that it results in a single linear, first-order differential equation, which is convenient to integrate.
5. Each component of the engine-out NO emission model is developed with a focus on the model's control purpose. Therefore, each is simplified to the extent that on-line evaluation becomes feasible, while the physics-based nature of the model is preserved as far as possible.

1.6 Approach

Models for NO prediction known from literature can be split into two groups: Either they are formulated using a mathematical relation that can be fitted to measured data obtained from a specific engine (e.g., table lookup, Artificial Neural Networks, or polynomials). Or they belong to the second category, which consists of models based on physical first principles, such as energy and mass balances.

The models of the first category can be fitted with high accuracy to measured data obtained from a specific engine – if enough tuning parameters are supplied. In most cases such models evaluate fast and are apt to work in a real-time environment. Their first shortcoming is that they produce unexpected results if they are presented inputs from another engine than the one for which they have been calibrated or if the inputs are taken from an operating regime not taken into account in the calibration of the model. A second shortcoming of those models is that they require a broad data set to calibrate the large number of parameters.

The second category of models is able to describe the general behavior of an engine. The few physically motivated parameters can be adjusted using few measurements only. Because of the generality of the principles that were applied while developing the model, such models can predict the engine behavior that lies beyond the range of the calibration data or they can be transferred to other engines. Their shortcoming is that often these models are not able to reproduce the engine behavior in sufficient detail or that their mathematics are too complex to be evaluated on real-time systems.

For this work an approach was chosen that brings the strengths of both model categories together: The generality, the ease of calibration, and the ability to extrapolate the engine behavior of the models that are based on physical first principles and the accuracy and suitability for real-time applications of parametric models. The four objectives formulated in Sect. 1.4 are addressed as follows: A model based on physical and semi-empirical principles ensures that the calibration effort remains small, it has the ability to extrapolate the engine behavior, and it provides the possibility to be applied to similar engines. The model is simplified to the extent that real-time applications become possible, while the essential input-output relations are maintained. The accuracy of the model is enhanced by

calibrating the model parameters for a number of reference operating points.

In order to describe the approach in more detail, the terms *operating point*, *operating variable*, *operating condition*, *nominal operating condition*, and *reference map* have to be defined for the context of this text.

Operating point An operating point is defined by the engine speed n and the inlet manifold pressure p_{im} .

Operating variable Engine operating variables are engine speed, inlet manifold pressure, spark advance, fuel/air equivalence ratio, residual gas mass fraction, engine block temperature, etc. The engine operating variables define the course of the combustion, e.g., pressure and temperature as a function of time.

Operating condition The operating condition is defined by setting each engine operating variable to a specific value.

Nominal operating condition The nominal operating condition is where all engine operating variables are set to their nominal values. The nominal values are the set points at which the engine normally is intended to operate.

Reference map The model is calibrated for each operating point with nominal operating conditions. The model parameters associated with those operating conditions are stored in the reference map.

Now it is possible to describe the modeling approach of the thesis more precisely. First, a model has been developed that predicts the in-cylinder pressure and the temperature of the burned gas. Based on

these results, the model calculates the engine-out NO emissions. The model is derived from physical first principles and semi-empirical approaches. Then the model is simplified in order to reduce the numeric burden. Attention is paid to preserving the essential input-output behavior of the model.

Then the model is calibrated using a set of reference operating points with nominal operating conditions (see Fig. 2.3). The operating points are equally distributed² over the operating range that is covered by the NEDC driving cycle. For calibration, measurements are taken at each of these operating points. The calibrated model parameters are stored in reference maps which serve as support to ensure high accuracy.

In a second step, the engine operating variables spark advance and fuel/air equivalence ratio are varied starting from their nominal values at one single operating point in the center of the operating range. The variations comprise four different spark advance and four different fuel/air equivalence ratio settings (see Fig. 2.4). The measured data from these variations serve to calibrate the model, such that it is able to correct the engine-out NO emissions due to any deviation of the engine operating variables from their nominal values at each operating point in the whole operating range.

With this procedure it is possible to derive a physics-based model that needs little calibration effort, but offers high accuracy throughout the whole operating range of interest and with good extrapolation capabilities to operating conditions not contained in the calibration data set.

²The reference operating points are aligned to a grid with knots at 1000, 2000, and 3000 rpm and 0.30, 0.50, and 0.65 bar inlet manifold pressure.

1.6.1 Evaluation of the Model

For a given combination of engine speed and inlet manifold pressure, the model parameters and nominal operating variables are interpolated from maps. The model is then used to calculate the NO emissions due to deviations of the current operating conditions from nominal conditions (see Fig. 1.4).

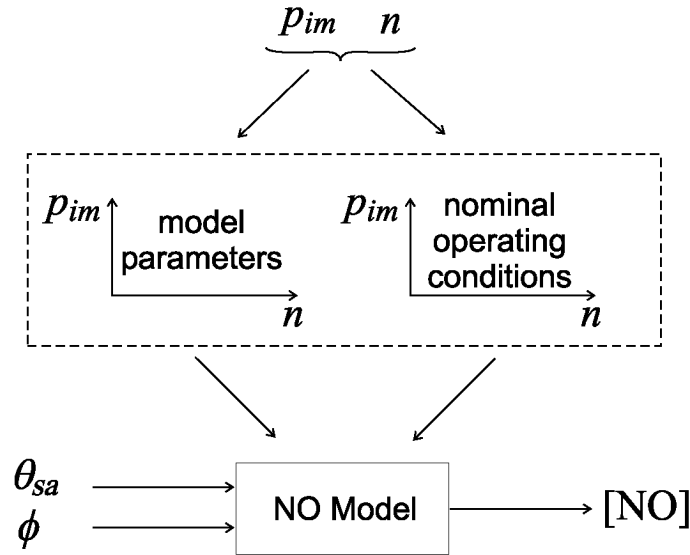


Figure 1.4: Approach for the model evaluation

1.6.2 Calibration of the Model

The calibration of the model involves the following two steps:

1. Generation of the reference maps: Measurement data has to be obtained from the engine at a grid of inlet manifold pressure and engine speed values, while running the engine at nominal operating conditions. Measured signals are: spark advance, fuel/air equivalence ratio, in-cylinder pressure, NO emissions, including engine speed and inlet manifold pressure. Those are stored in

reference maps. Values stored in the reference map are denoted by the superscript ⁰.

2. Calibration of the model parameters: Measurement data has to be obtained from the engine at various fuel/air equivalence ratio and spark advance settings at a representative operating point. From this data optimal model parameters are determined.

1.6.3 Structure of the Model

The NO emission model consists of three distinct submodels:

1. The in-cylinder pressure estimation model incorporating a combustion model. The in-cylinder pressure estimation method uses the feedback of the measured crankshaft angular velocity for the adaption of the model parameters.
2. The submodel for the burned gas zone used to calculate the burned gas temperature.
3. The submodel for the NO formation which computes the engine-out NO emissions.

The structure of the NO emission model with its submodels is depicted in Fig. 1.5.

1.6.4 Cylinder Pressure Estimation

The cylinder pressure algorithm consists of two parts: A pressure estimation and a parameter adaption part. In the pressure estimation path the normalized heat-release profile x_b is calculated using a reference heat-release profile and calculated deviations from it. The deviation of the current heat-release profile is calculated using an approach similar to the one presented in [18]. The transient in-cylinder pressure is then computed using results from [53] and [45].

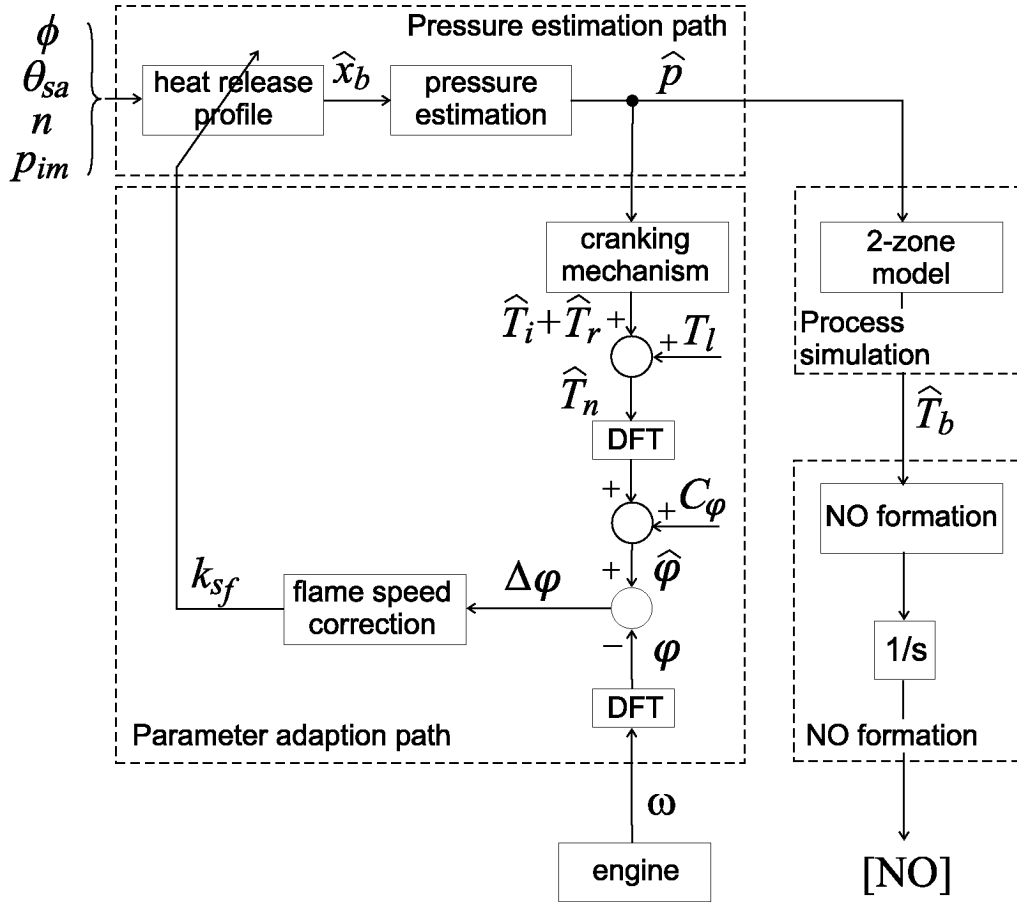


Figure 1.5: Signal-flow graph of the NO estimation model with its sub-models.

In the parameter adaption path, the indicated torque is calculated based on the in-cylinder pressure. The torque due to the oscillating masses is considered in the computation. The net torque driving the crankshaft is then the sum of indicated torque and the torque due to the oscillating masses. Integrating the net torque yields the crankshaft angular velocity. Finally, a Fourier transformation is used to extract the phase at the engine firing frequency from the spectrum of the crankshaft angular velocity. Additionally, the transient crankshaft angular velocity is measured and also processed to extract the phase

at the engine firing frequency. The difference between measured and calculated phase is used to correct the heat-release profile.

1.6.5 Burned Gas Temperature

As mentioned earlier, the nitric oxide is assumed to form in the hot burned gas zone behind the flame front. The in-cylinder volume therefore has to be split into two zones at least, separated by the flame front. Using simplifying assumptions, a mathematical formulation of the temperature of the burned gas is derived, which avoids numerical integration. A full 0-dimensional 2-zone model is used to justify the results of the simplified model.

1.6.6 NO Formation

For the formation of NO, the assumption is typically made that all species except for NO are at their chemical equilibrium. The equilibrium species concentrations of N, O, H, and OH, but also of NO, are precomputed as functions of temperature, pressure, and fuel/air equivalence ratio and stored in maps. Only the Extended Zeldovich Mechanism is taken into account as a formation mechanism of NO. Using the precomputed information, it can be condensed into one differential equation. Numerical integration of this differential equation is not time critical. Rather the interpolation from the precomputed maps needs careful numerical treatment, as will be shown.

1.7 Organization of the Text

After this first introductory chapter the organization of the thesis is as follows:

Chapter 2 outlines the experimental setup.

- Chapter 3** introduces a control-oriented model for the estimation of the in-cylinder pressure of a homogeneous SI engine. The measured crankshaft angular velocity is used to adapt the model parameters. Furthermore, the model is compared to a benchmark pressure estimation method.
- Chapter 4** details the calculation of the burned gas temperature and volume in the combustion chamber of the homogeneous SI engine.
- Chapter 5** describes a control-oriented model for the NO formation in the combustion chamber of the homogeneous SI engine.
- Chapter 6** provides a detailed list of the cpu time needed to calculate the various modules of the NO estimation model.
- Chapter 7** furnishes a summary and draws conclusions from the material presented.
- The Appendix** offers a step-by-step calibration procedure for the NO estimation model, states the governing equations for the heat-release analysis, and provides the details for the calculation of the thermodynamic properties of the gas.

Chapter 2

Experiments

The measurement data used for calibration and validation of the model was obtained from a DaimlerChrysler M112 E32 engine connected to a Schenk eddy current brake.

2.1 Engine and Test Bench Hardware

The test bench consists of the engine, the eddy current brake, a set of flywheels, the exhaust gas analyzer, and appropriate measurement and control equipment. The engine and the eddy current brake are connected through the clutch, the gearbox, and a connecting shaft. The flywheels are driven by a belt. Figure 2.1 shows the setup of the test bench and its main components. Figure 2.2 shows a photograph of the engine mounted on the test bench, together with the eddy current brake and the data acquisition equipment.

The eddy current brake allows a brake torque of 150 Nm and a power of 70 kW. The allowable engine speed is limited by the drive belt and the flywheels. Although the limitations of the test bench do not allow the exploration of the whole operating range of the engine, it

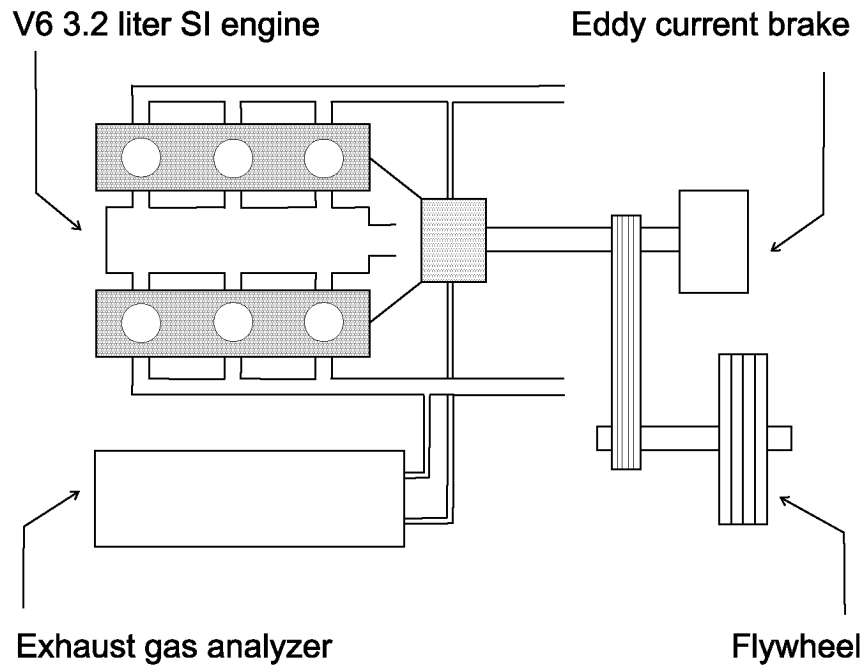


Figure 2.1: Main components of the test bench

does permit an engine operation at all operating points covered by the European driving cycle for a midsize car equipped with this engine. The control unit of the test bench is able to guarantee a constant engine speed under variable load levels and to measure the mean net torque on the eddy current brake.

The engine is a standard V6 port-injected gasoline engine with a total displacement of 3.2 liters. Table 2.1 lists the main specifications of the engine. Each cylinder is equipped with a pressure sensor. Additionally, pressure and temperature sensors are situated in the air and exhaust paths. The engine is equipped with an ECU that allows reading and writing ECU-internal values, such as spark advance and injection timing.

Equipment for the steady-state measurement of the engine-out concentrations of CO, CO₂, NO, HC, and O₂ completes the test bench hardware.

Table 2.1: Main engine specifications

Manufacturer Type	DaimlerChrysler AG M112 E32	
Property	Units	Value
Displacement	cm^3	3199
Bore	mm	89.9
Stroke	mm	84
Compression ratio	-	10:1
Connecting rod length	mm	148.5
Rated power at engine speed	kW at $1/min$	165 at 5600
Rated torque at engine speed	Nm at $1/min$	315 at 3000

2.2 Data Acquisition

The data acquisition system consists of two main components: (1) a data acquisition system for crank-angle-based measurements and (2) a data acquisition system for time-based measurements.

The former data acquisition system serves to record the in-cylinder pressure, the pressure in the inlet and outlet manifolds, the signals from the λ sensors, the data on injection and spark advance timing, and the instantaneous crankshaft angular velocity. All these signals are recorded with a resolution of 0.2 crank angle degrees using an Eckelmann transient recorder. Table 2.2 lists the signals recorded with this system.

The time-based data acquisition system collects data on temperature, air mass and fuel mass flows, brake speed and torque, the status of the engine (oil pressure, coolant temperature, etc.), and on the engine-out emissions. Furthermore, ECU-internal signals are recorded. All time-based signals are collected by a WAGO field bus system and are transmitted via CAN protocol to the measurement PC. Table 2.2 lists the recorded signals.

Table 2.2: Recorded signals

Time-based measurements	Crank-angle-based measurements
<p><u>External sensors:</u></p> <ul style="list-style-type: none"> • Pressures: Oil, fuel, ambient, inlet manifold, exhaust manifold l. and r., end pipe • Fuel/air equivalence ratio: left and right bank • Air mass flow • Brake speed and torque • Inlet manifold CO₂ • Exhaust gas components: CO, CO₂, NO, HC, O₂ • Temperatures: Exhaust manifold l. and r., exhaust port of cyl. 6, end pipe, oil, water, fuel, ambient, inlet manifold, inlet port of cyl. 6 • Incremental encoder: Engine speed <p><u>ECU-internal values:</u></p> <ul style="list-style-type: none"> • Engine speed • Throttle plate angle • Oil pressure • Engine temperature • Injection timing cyl. 1 - 6 • Ignition timing cyl. 1 - 6 • EGR valve position • Status of knock controller, inlet manifold geometry, idle speed controller, full load enrichment, fuel cut-off 	<ul style="list-style-type: none"> • In-cylinder pressure cyl. 1- 6 • Inlet port pressure cyl. 6 • Exhaust port pressure cyl. 6 • Ignition timing cyl. 1 - 6 • Injection timing cyl. 1 - 6 • Air mass flow meter • Fuel/air equivalence ratio: left and right bank

2.3 Operating Points

Measurements are taken at a grid of engine speed and inlet manifold pressure. The inlet manifold pressure is set to $p_{im} = 0.30, 0.50,$ and 0.65 bar and the engine speed to $n = 1000, 2000,$ and 3000 rpm, such that a grid with 9 knots is created. At each knot, the engine runs at steady-state conditions and at nominal operating conditions. The data from these operating points is recorded and serves as the set of reference operating conditions to support the model at the grid points of the operating range. A second set of data is recorded with operating conditions different from the nominal settings. Starting from each operating point with nominal operating condition, spark advance and fuel/air equivalence ratio are varied. The spark advance is set to two earlier and two later settings than the nominal value. The fuel/air equivalence ratio is set to one richer position and three leaner positions than the nominal value. In total, 9 times 8 variations are recorded. Figures 2.3 and 2.4 show the operating points and conditions at which measurements are obtained.

2.4 Data Sets

The calibration and validation of the various submodels described later in this text relies on subsets of the collected data. Therefore, the collected data is grouped into different data sets, for later reference:

1. Data set **A** contains the data obtained at the reference operating points.
2. Data set **A**⁺ contains data set **A** plus one measurement per reference operating point where the spark advance is retarded.
3. Data set **B** contains all measurements acquired at fuel/air equivalence ratios and spark advance settings other than nominal set-

tings.

4. Data set \mathbf{B}^- contains data acquired during the spark advance and the air/fuel equivalence ratio variations at the reference operating point at an engine speed of $n = 2000$ rpm and at an inlet manifold pressure of $p_{im} = 0.5$ bar.

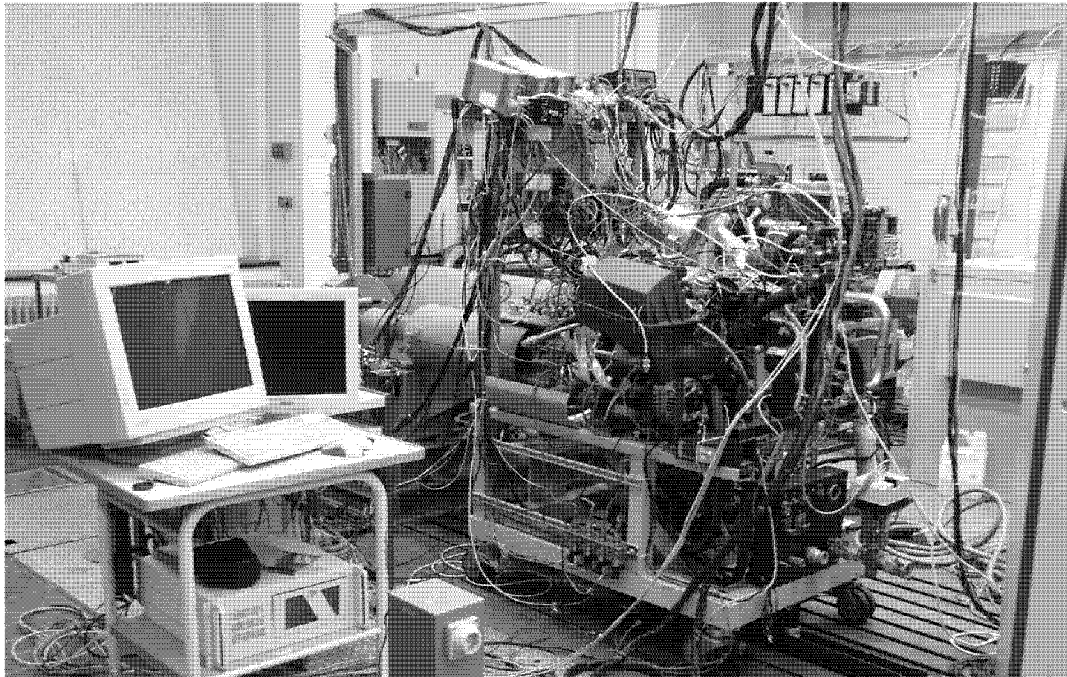


Figure 2.2: DaimlerChrysler M 112 E 32 engine, eddy current brake, and data acquisition equipment

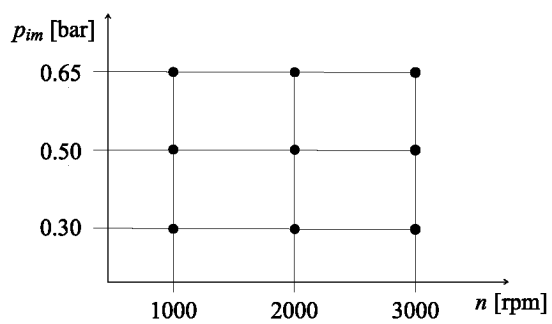


Figure 2.3: Reference operating points

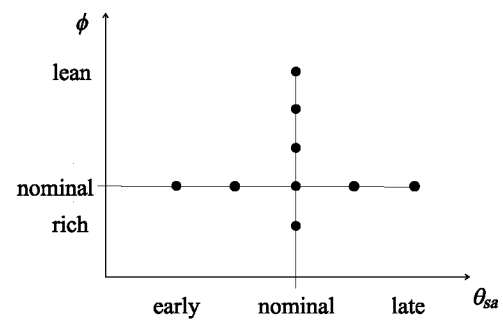


Figure 2.4: Variations of the operating conditions

Chapter 3

In-Cylinder Pressure

This chapter introduces a model for the estimation of the instantaneous in-cylinder pressure. The estimated pressure is averaged over a number of cycles and all cylinders, although the model conceptually allows the in-cylinder pressure for each cylinder to be estimated individually. The model consists of two parts: A *pressure estimation path* and a *parameter adaption path* (see Fig. 1.5).

In the pressure estimation path, the in-cylinder pressure is estimated based on engine speed n , inlet manifold pressure p_{im} , spark advance θ_{sa} , and fuel/air equivalence ratio ϕ . First, the flame development angle θ_d and the rapid burning angle θ_b are calculated using an approach similar to the one presented in [18]. Then, the in-cylinder pressure is reconstructed using results from [53] and [45]. Finally, the in-cylinder pressure is used to calculate the torque on the crankshaft and the instantaneous rotational velocity of the crankshaft.

In the parameter adaption path, a *phase-controlled algorithm* serves to adapt θ_d and θ_b such that the phasing of the measured and calculated crankshaft angular velocity match. For this purpose, the time history of the instantaneous crankshaft angular velocity of one engine

cycle is decomposed into a series of harmonic functions

$$\omega(\theta) = \sum_m A_m \sin\left(m \frac{\theta}{4\pi} 2\pi - \varphi_{\omega,m}\right) \quad m = 1, 2, \dots \quad (3.1)$$

The amplitude at the frequency m is denoted by A_m . The symbol θ denotes the crank angle, which runs from 0 to 4π during one engine cycle and $\varphi_{\omega,m}$ is the phase associated with m . The phase $\varphi_{\omega,m}$, where m equals the number of cylinders, is referred to as the phase at the engine firing frequency.

The phase-controlled algorithm makes use of the facts illustrated in Fig. 3.1. In the left-hand graph the measured instantaneous crankshaft angular velocity is shown for three different spark advance settings at engine speed $n = 1000$ rpm and inlet manifold pressure $p_{im} = 0.5$ bar. The graph shows two important points: First, the combustion pulses can be clearly seen in the oscillation pattern of the crankshaft angular velocity, and second, the amplitude and the phasing of the crankshaft angular velocity are affected by the spark advance.

The right-hand graph makes the effect of the spark advance on the phasing more obvious. It shows the phase of the crankshaft angular velocity at the engine firing frequency relative to the phase at nominal operating conditions ($\theta_{sa}^0 = -21$ deg in this example) for the three different spark advance settings. Clearly, the phase moves to larger values as the spark discharge is retarded. This effect can be explained as follows. Retarding the spark discharge causes the combustion to start later and (in general) to progress more slowly. As a consequence, the peak of the in-cylinder pressure is retarded as well. The in-cylinder pressure is transformed to indicated torque which drives the crankshaft. As a consequence, a change in the combustion phasing affects the phasing of the crankshaft angular velocity, and in particular the phase at firing frequency. A similar effect would be visible for dif-

ferent fuel/air equivalence ratios. A leaner mixture slows the flame speed down, which causes the combustion to start later and to run more slowly with a similar effect on the phase at the engine firing frequency.

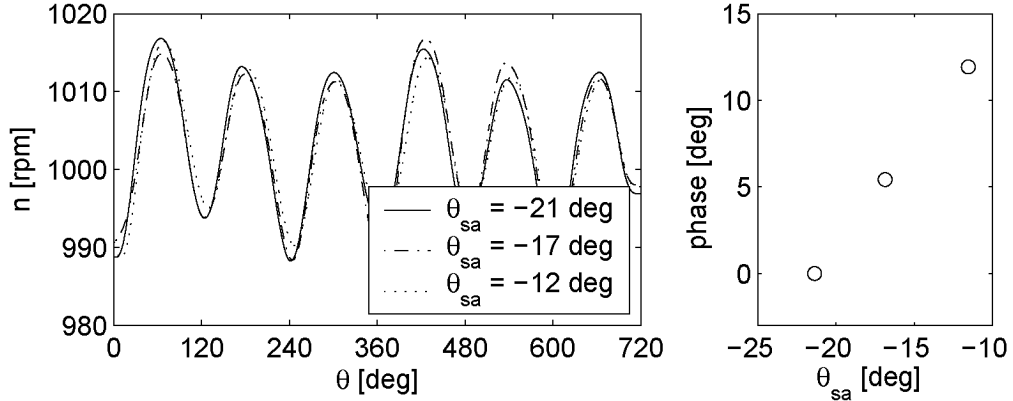


Figure 3.1: Measured instantaneous crankshaft angular velocity at $n = 1000$ rpm and $p_{im} = 0.5$ bar. Left graph: Instantaneous crankshaft angular velocity plotted against crank angle. Right graph: Phase at the engine firing frequency for three different spark advance settings

The algorithm that will be presented in this chapter compares calculated and measured phases of the crankshaft angular velocity and uses the difference to correct the values of θ_d and θ_b previously estimated in the pressure estimation path.

The organization of this chapter follows the signal-flow graph depicted in Fig. 1.5. It starts with a method for the calculation of the burned mass fraction $x_b(\theta)$ as a function of the crank angle. Cornerstones are the calculation of the two parameters flame development angle θ_d and rapid burning angle θ_b . Then a model for calculating the in-cylinder pressure $p(\theta)$, the net torque at the crankshaft $T_n(\theta)$, and the instantaneous crankshaft angular velocity $\omega(\theta)$ is presented. Based on this material the adaption scheme for θ_d and θ_b is developed. The chapter ends with a comparison of the pressure estimation method to a benchmark method taken from the literature ([36], [17]).

3.1 Heat-Release Profile

The heat-release profile $x_b(\theta)$ describes the ratio between the heat released at the crank angle position θ and the total heat released during the combustion. For the homogeneous combustion x_b is equal to the ratio of the burned mass to the total mass trapped in the combustion chamber:

$$x_b(\theta) = \frac{Q_f(\theta)}{Q_f(\theta = \theta_{ce})} = \frac{m_b}{m_b + m_u} \quad (3.2)$$

For the heat-release profile, the parametrized form known as Vibe function was chosen

$$x_b(\theta) = 1 - e^{a\left(\frac{\theta - \theta_{cs}}{\theta_{ce} - \theta_{cs}}\right)^{m_v + 1}}, \quad (3.3)$$

where θ , θ_{cs} , and θ_{ce} are the crank angle, the start of combustion, and the end of combustion, respectively. The constant $a = -6.7$ ensures a fuel conversion rate of 99.9% at the combustion end. The form parameter $m_v = 2$ is held constant. Combustion start and combustion end are functions of engine speed n , inlet manifold pressure p_{im} , spark advance θ_{sa} , fuel/air equivalence ratio ϕ , EGR rate x_r , etc. For the purpose of this text, only the dependence on n , p_{im} , θ_{sa} , and ϕ is taken into account, because the test bench setup did not allow for any other parameters to be varied. Combustion start and end follow from the equations below, which will be reviewed in detail in the next subsection.

$$\theta_{cs} = \theta_{sa} + \theta_d(p_{im}, n, \theta_{sa}, \phi) \quad (3.4)$$

$$\theta_{ce} = \theta_{sa} + \theta_d(p_{im}, n, \theta_{sa}, \phi) + \theta_b(p_{im}, n, \theta_{sa}, \phi) \quad (3.5)$$

3.1.1 Flame Development Angle and Rapid Burning Angle

In the previous section the flame development angle θ_d and the rapid burning angle θ_b were introduced. The flame development angle is the crank angle interval between the spark discharge and the start of the combustion, while the rapid burning angle is the crank angle interval from combustion start to combustion end [34].

In order to mathematically express the dependency of θ_d and θ_b on engine operation variables, the approach presented in [18] is taken and slightly modified¹:

$$\theta_d = k_d \theta_d^0 \frac{f_{sa}(\theta_{sa})}{f_{sa}(\theta_{sa}^0)} \frac{f_\phi(\phi)}{f_\phi(\phi^0)} \quad (3.6)$$

$$\theta_b = k_b \theta_b^0 \frac{g_{sa}(\theta_{sa})}{g_{sa}(\theta_{sa}^0)} \frac{g_\phi(\phi)}{g_\phi(\phi^0)} \quad (3.7)$$

The superscript 0 indicates a lookup value in the reference map at given values of engine speed and inlet manifold pressure. The polynomials f_{sa} and g_{sa} are of first order, the polynomials f_ϕ and g_ϕ are of second order. The gains k_d and k_b are correcting factors allowing the adaption of the flame development and the rapid burning angle to actual combustion conditions. Their importance is described in more detail below.

In order to calibrate the coefficients of the polynomials f_{sa} , f_ϕ , g_{sa} , and g_ϕ , the in-cylinder pressure was calculated using Eqs. (3.3) to (3.7) and (3.29) on page 45 as well as the setting $k_d = k_b = 1$. By comparing the calculated pressure with the measured in-cylinder

¹The modifications concern: (A) The parameters θ_d and θ_b are tabulated for a set of reference operating points rather than only for a central operating point. (B) With the polynomials f_{sa} , f_ϕ , g_{sa} , and g_ϕ , only the spark advance and the fuel/air equivalence ratio are taken into account. The polynomials are calibrated with data obtained from a 6-cylinder 3.2-liter engine, rather than with the coefficients proposed in [18].

pressure obtained from spark advance and fuel/air equivalence ratio variations at $n = 2000$ rpm and $p_{im} = 0.5$ bar (data set \mathbf{B}^-), the best (in a mean-squared-error sense) set of coefficients for the polynomials f_{sa} , f_ϕ , g_{sa} , and g_ϕ is computed. Figure 3.2 shows the calculated peak pressure and peak pressure location compared to measured data.

The values for k_d and k_b are calculated based on the phase at the engine firing frequency of the measured crankshaft angular velocity on a cycle-to-cycle basis. One difficulty arises from the fact that two quantities (k_d and k_b) have to be inferred simultaneously from one measurement ($\varphi_{\omega,6}$). The next section addresses this problem by formulating both the flame development and the rapid burning angle as functions of the flame speed. This makes it possible to estimate the flame speed first and then to calculate k_d and k_b .

The expressions (3.6) and (3.7) can be extended to include the residual gas mass as well. This can be done by appending the terms $f_{x_r}(x_r)/f_{x_r}(x_r^0)$ and $g_{x_r}(x_r)/g_{x_r}(x_r^0)$, respectively. The same technique can be used to include the charge temperature during the compression stroke and other engine operating variables (see [19] for reference). Since the residual gas mass could not be controlled on the test bench, the variations were limited to spark advance and fuel/air equivalence ratio variations.

3.1.2 Parametrization of the Flame Development and the Rapid Burning Angle

As pointed out earlier, the phase of the instantaneous crankshaft angular velocity will be used to calculate k_d and k_b and to correct the flame development and rapid burning angle, such that they converge to the true values of θ_d and θ_b .

This subsection is divided into two parts. The first part characterizes the relation between the flame development and the rapid

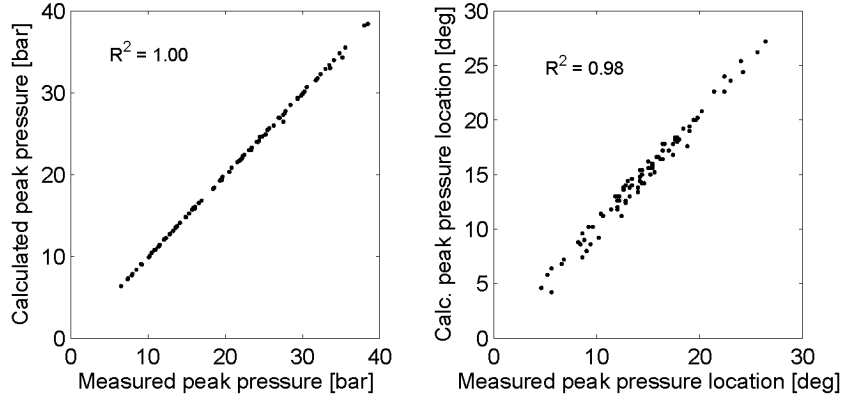


Figure 3.2: Calculated and measured peak pressure and peak pressure location for all operating points and conditions, with R being the correlation coefficient of measured and calculated data

burning angle and the phase of the crankshaft angular velocity at the engine firing frequency. It is shown that it is difficult to infer θ_d and θ_b from the phase of the crankshaft angular velocity simultaneously. Therefore, the second part of the subsection introduces θ_d and θ_b as functions of the flame speed. Through a series of algebraic manipulations it is possible to show that θ_d and θ_b are in a good approximation proportional to $(S_l)^{-2/3}$ (S_l being the flame speed). Based on this material it is possible to estimate the single parameter S_l and from that to infer both θ_d and θ_b .

Relations between θ_d , θ_b , and φ_ω

The relations between the flame development, the rapid burning angle, and the phase of the crankshaft angular velocity at the engine firing frequency are accessed in three steps:

1. The phase of the crankshaft angular velocity at the engine firing frequency is calculated for the reference values $\theta_{d,ref}$ and $\theta_{b,ref}$. The resulting reference phase $\varphi_{\omega,6,ref}$ is stored for later use.
2. The phase of the crankshaft angular velocity at the engine firing

frequency is calculated for $\theta_{d,i}$, $i = 1 \dots n$, and $\theta_{b,j}$, $j = 1 \dots m$. The resulting phases $\varphi_{\omega,6,ij}$ are used to form the cost function $J(\theta_d, \theta_b)$:

$$J(\theta_d, \theta_b) = (\varphi_{\omega,6}(\theta_d, \theta_b) - \varphi_{\omega,6,ref})^2 \quad (3.8)$$

3. The cost function $J(\theta_d, \theta_b)$ is depicted in Fig. 3.3. It allows to draw conclusions as to whether it is possible to infer both θ_d and θ_b from $\varphi_{\omega,6}$.

The calculation of the phase of the crankshaft angular velocity at the engine firing frequency comprises the following steps: First, the burned mass fraction $x_b(\theta)$ is calculated, then the in-cylinder pressure $p(\theta)$ is computed, which serves to calculate the net torque $T_n(\theta)$ at the crankshaft. Integrating the torque yields the instantaneous crankshaft angular velocity $\omega(\theta)$. Finally, the crankshaft angular velocity is Fourier-transformed and the phase at the engine firing frequency $\varphi_{\omega,6}$ is extracted.

The surface in Fig. 3.3 shows two important results. First, the phase at the engine firing frequency shows a clear dependency on θ_d and θ_b . Second, the surface $J(\theta_d, \theta_b)$ exhibits a long "valley", which makes it difficult for numeric algorithms to find the correct combination of the θ_d and θ_b . The latter observation implies that a relation between θ_d and θ_b has to be established, if they have to be inferred simultaneously from the measured phase.

The Parameters θ_d and θ_b as Functions of the Flame Speed

Earlier research [35] and [34] has shown that θ_d and θ_b are closely coupled through the flame speed. It is therefore possible to parametrize the flame development and the rapid burning angle with the flame speed. Figure 3.4 shows a cross section of the surface $J(\theta_d, \theta_b)$ in Fig. 3.3. The cross section lies approximately perpendicular to the long

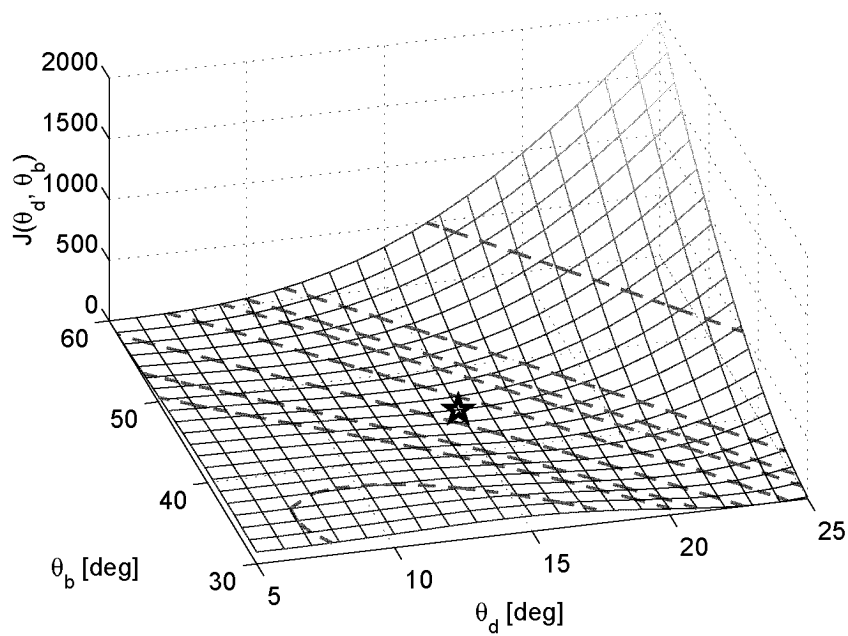


Figure 3.3: Dependency of the phase of the crankshaft angular velocity at engine firing frequency from θ_d and θ_b (simulated data). The reference flame development and rapid burning angle are illustrated with a star. The dashed contour lines emphasize the shape of the surface, which makes it difficult for numeric algorithms to find the minimum of $J(\theta_d, \theta_b)$

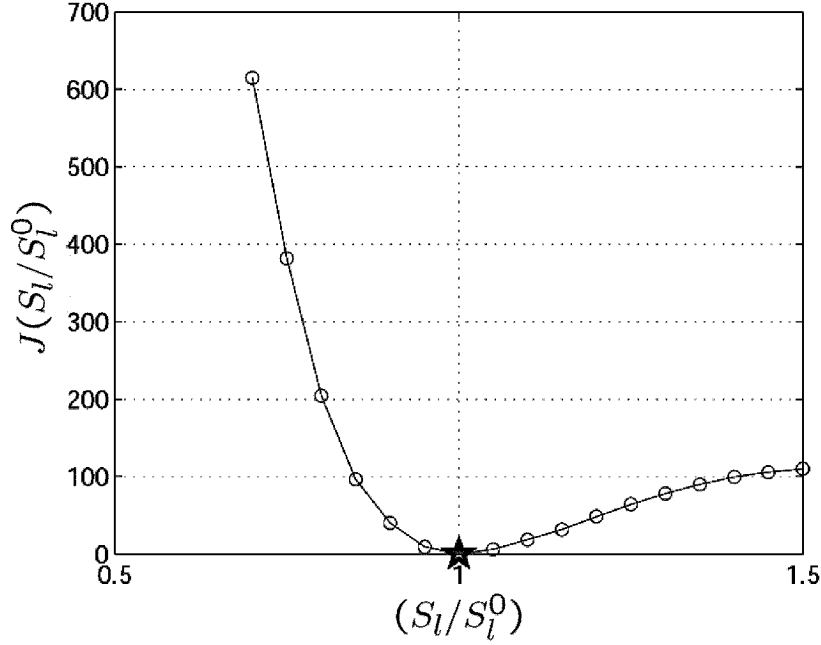


Figure 3.4: Cross section of the error surface $J(\theta_d, \theta_b)$ depicted in Fig. 3.3 using the flame speed to parametrize θ_d and θ_b

”valley” formed by $J(\theta_d, \theta_b)$. The ratio of the actual flame speed to the nominal flame speed (S_l/S_l^0) is used as a parameter. In this way it is possible to find the flame speed that offers the minimum phase difference to the reference phase and to use it for the correction of θ_d and θ_b .

The remainder of this subsection will show the details of how the flame development and the rapid burning angle can be parametrized using the flame speed. The start is made by stating a formulation for the flame development and the rapid burning angle taken from [35]:

$$\theta_d = C (c_m \nu)^{1/3} \left(\frac{h}{S_l} \right)^{2/3} \quad (3.9)$$

$$\theta_b = D \left(\frac{B}{h^*} \right) \left(\frac{\rho_i}{\rho_u^*} \right)^{10/9} (c_m \nu^*)^{1/3} \left(\frac{h_i}{S_l^*} \right)^{2/3} \quad (3.10)$$

where c_m , $\nu = \mu/\rho$, h , B , S_l , ρ are the mean piston speed, the kinematic viscosity, the clearance height, the bore, the laminar flame speed, and the density. The subscript i stands for ignition (for instance, end of flame development), the subscript u stands for properties of the unburned gas, and $*$ marks the crank angle position where 50% of the mass is burned. The variables C and D are lumped geometrical engine design parameters. In Eq. (3.9), ν , h , and S_l are values that are averaged over the entire period from spark discharge to the beginning of the combustion.

The text now focuses on simplifying the expressions (3.9) and (3.10). As a first step, the term (ρ_i/ρ_u^*) is simplified.

$$\frac{\rho_i}{\rho_u^*} = \frac{\frac{m_0}{A_p h_i}}{\frac{0.5m_0}{A_p h_u^*}} \quad (3.11)$$

In [34] it is shown that the density of the unburned zone is approximately four times the density of the burned zone for a wide range of engine operating conditions². This relation is applied to the position where 50% of the mass is burned.

$$\begin{aligned} \frac{\rho_u^*}{\rho_b^*} &= \frac{0.5m_0}{V_u^*} \frac{V_b^*}{0.5m_0} = \frac{h_b^*}{h_u^*} = 4 \\ h^* &= h_b^* + h_u^* \\ \Rightarrow h_u^* &= \frac{1}{5}h^* \end{aligned} \quad (3.12)$$

Inserting (3.12) into (3.11) yields:

$$\frac{\rho_i}{\rho_u^*} = \frac{2}{5} \frac{h^*}{h_i} \quad (3.13)$$

²The ratio of the densities of the burned and the unburned gas depends on the fuel/air equivalence ratio. For fuel/air equivalence ratio variations found in homogeneous spark ignited engines, this dependency can be omitted. Results shown later support this assumption

Inserting (3.13) into (3.10), the rapid burning angle becomes:

$$\theta_b = D' B (h^*)^{1/9} (h_i)^{-4/9} (c_m \nu^*)^{1/3} (S_l^*)^{-2/3} \quad (3.14)$$

The kinematic viscosity ν in (3.9) can be expanded as follows:

$$\nu = \frac{\mu}{\rho} = \frac{A_p h}{m_0} \mu_0 \left(\frac{T}{T_0} \right)^n \quad (3.15)$$

The variables μ , ρ , A_p , h , m_0 , and T are the dynamic viscosity, the density, the cylinder cross section, the clearance height, the total mass of the charge, and the temperature, respectively. The symbols μ_0 and n are constants for a specific gas³. The temperature T can be expressed as:

$$\begin{aligned} pV^\kappa &= \text{const} \\ TV^{\kappa-1} &= \text{const} \\ Th^{\kappa-1} &= \text{const} \\ T &= \text{const} \cdot h^{1-\kappa} \end{aligned} \quad (3.16)$$

Inserting (3.15) and (3.16) into (3.9) and (3.14), the flame development and the rapid burning angle become:

$$\theta_d = C' c_m^{1/3} \left(\frac{\mu_0 A_p}{m_0 T_0^n} \right)^{1/3} h^{1+n \frac{1-\kappa}{3}} S_l^{-2/3} \quad (3.17)$$

$$\theta_b = D' B (h^*)^{1/9} (h_i)^{-4/9} c_m^{1/3} \left(\frac{\mu_0 A_p h^*}{m_0 T_0^n} \right)^{1/3} (h^*)^{n \frac{1-\kappa}{3}} (S_l^*)^{-2/3} \quad (3.18)$$

The term $n \frac{1-\kappa}{3}$ is about -0.07 . The constants μ_0 , T_0^n , A_p and m_0

³For air and $T_0 = 273$ K, $\mu_0 = 1.17e^{-5}$ kgm⁻¹s⁻¹, $n = 0.7$; The ratio of specific heats is approximated as $\kappa \approx 1.3$ for temperatures prevailing in the combustion chamber.

are lumped together with the constant values of C' and D' into the constant values of C'' and D'' , respectively.

$$\theta_d = C'' c_m^{1/3} h^{1.60} S_l^{-2/3} \quad (3.19)$$

$$\theta_b = D'' B (h^*)^{0.375} (h_i)^{-4/9} (c_m)^{1/3} (S_l^*)^{-2/3} . \quad (3.20)$$

So far, the rapid burning angle is parametrized by geometric properties and the laminar flame speed at 50% mass fraction burned, S_l^* , while the flame development angle is parametrized by geometric properties and the laminar flame speed during the flame development phase, S_l . In order to reduce the parametrization to one single parameter (apart from the geometric properties), a relation between S_l and S_l^* must be introduced.

The laminar flame speed can be calculated as follows [34]:

$$S_l = S_{l,0} \left(\frac{T_u}{T_0} \right)^\alpha \left(\frac{p}{p_0} \right)^\beta (1 - 2.06x_r^{0.77}) \quad (3.21)$$

The values of α and β depend on the fuel/air equivalence ratio and thus are constant during the combustion of premixed fuel and air. The quantities $S_{l,0}$, T_0 , and p_0 are reference values for the computation of the laminar flame speed, while x_r is the residual gas mass fraction. Dividing the laminar flame speed during the flame development S_l by the laminar flame speed where 50% of the mass is burned S_l^* yields:

$$\frac{S_l}{S_l^*} = \left(\frac{T_u}{T_u^*} \right)^\alpha \left(\frac{p}{p^*} \right)^\beta \quad (3.22)$$

Assuming that the unburned zone undergoes isentropic compression, the ratio between T_u and T_u^* is given by

$$\frac{T_u}{T_u^*} = \left(\frac{p}{p^*} \right)^{\frac{\kappa-1}{\kappa}} \quad (3.23)$$

Finally the relation between the two flame speeds is given:

$$\begin{aligned}\frac{S_l}{S_l^*} &= \left(\frac{p}{p^*}\right)^{\alpha \frac{\kappa-1}{\kappa}} \left(\frac{p}{p^*}\right)^\beta \\ S_l^* &= S_l \left(\frac{p}{p^*}\right)^{\alpha \frac{\kappa-1}{\kappa} + \beta}\end{aligned}\quad (3.24)$$

Summing up, the equations for θ_d and θ_b are given below:

$$\theta_d = C''(c_m)^{1/3} h^{1.60} S_l^{-2/3} \quad (3.25)$$

$$\theta_b = D'' B (h^*)^{0.375} (h_i)^{-4/9} (c_m)^{1/3} \left(\frac{p}{p^*}\right)^{-2/3(\alpha \frac{\kappa-1}{\kappa} + \beta)} (S_l)^{-2/3} \quad (3.26)$$

Both expressions, (3.25) and (3.26) can be grouped as follows:

$$\theta_d = G_d H_d k_{s_f}^{-2/3} \quad (3.27)$$

$$\theta_b = G_b H_b k_{s_f}^{-2/3} \quad (3.28)$$

where:

$$G_d = C''(c_m)^{1/3} (S_l^0)^{2/3}$$

$$H_d = h^{1.60}$$

$$G_b = D''(c_m)^{1/3} (S_l^0)^{2/3}$$

$$H_b = (h^*)^{0.375} (h_i)^{-4/9} \left(\frac{p}{p^*}\right)^{-2/3(\alpha \frac{\kappa-1}{\kappa} + \beta)}$$

$$k_{s_f} = \frac{S_l}{S_l^0}$$

The values G_d and G_b are constant for any given operating point. The quantities H_d and H_b depend on geometry and in-cylinder pressure. The variations of H_d and H_b are usually small and are neglected for

the purpose of this text. The ratio between the actual flame speed and the flame speed at nominal operating conditions k_{s_f} remains the parameter with the dominant influence on the flame development and the rapid burning angle. (See also [26] and [44].)

For operating conditions with nominal flame speed S_l^0 , the flame development and the rapid burning angle are calculated using (3.6) and (3.7) with $k_d = k_b = 1$. If a non-measured disturbance changes the actual flame development and rapid burning angle, it is possible to rely on the fact that they are in proportion to $S_l^{-2/3}$. Therefore it is possible to replace k_d and k_b in (3.6) and (3.7) with $(k_{s_f})^{-2/3}$:

$$k_d = k_b = (k_{s_f})^{-2/3}$$

In Sect. 3.6 an adaption rule is proposed to compensate for flame speed deviations.

3.2 In-Cylinder Pressure

In this section, an analytic model of the in-cylinder pressure during the high pressure cycle is given. The material follows the work presented in [25].

During the compression and expansion phases, the in-cylinder pressure follows a polytropic compression and a polytropic expansion, respectively. During combustion, the in-cylinder pressure is interpolated between the two enveloping polytropic pressure trajectories as shown in Fig. 3.5.

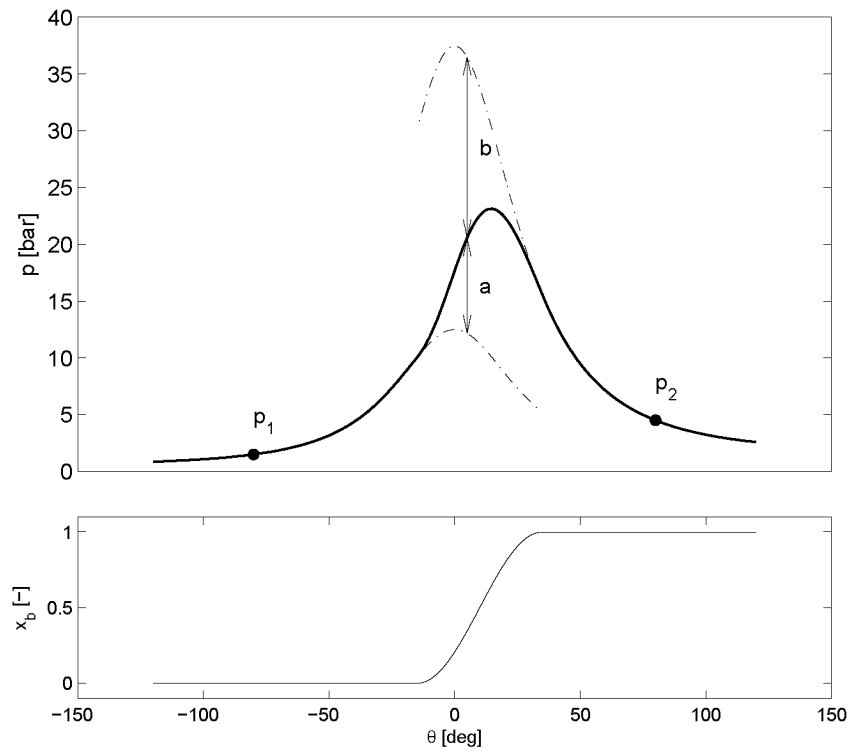


Figure 3.5: The upper graph shows the interpolation of the in-cylinder pressure between the two enveloping polytropic pressure trajectories. The burned mass fraction x_b is used as interpolation parameter: $\frac{x_b}{1-x_b} = \frac{a}{b}$. The lower graph shows the burned mass fraction as a function of the crank angle

The in-cylinder pressure can be written as:

$$p(\theta) = (1 - x_b(\theta)) \underbrace{p_1^0 \left(\frac{V_{80}}{V(\theta)} \right)^{\kappa_u}}_{\substack{\text{polytropic} \\ \text{compression}}} + x_b(\theta) \underbrace{p_2 \left(\frac{V_{80}}{V(\theta)} \right)^{\kappa_b}}_{\substack{\text{polytropic} \\ \text{expansion}}}, \quad (3.29)$$

The parameters κ_u and κ_b are calibrated using the data set **A**. The pressure p_1^0 at 80 degrees before top dead center is taken from the reference map. The pressure p_2 at 80 degrees after top dead center is calculated as follows (see [45])

$$p_2 = p_1^0 + \Delta p^0 c_{\Delta p} (\theta_{80} - \theta_{80}^0) \left(\frac{\max(1/\phi^0, 1) + 0.5}{\max(1/\phi, 1) + 0.5} \right), \quad (3.30)$$

where Δp^0 , θ_{80}^0 , and ϕ^0 are the reference values for the difference between p_1 and p_2 at nominal operating conditions, the crank angle position when 80% of the combustion time has elapsed, and the fuel/air equivalence ratio at nominal operating conditions, respectively. The constant $c_{\Delta p}$ compensates for the changing heat transfer with changing combustion phasing. The calculated pressure differences $p_2 - p_1^0$ are compared to measured data obtained from a 6-cylinder 3.2-liter SI engine and are depicted in Fig. 3.6.

3.3 Crankshaft and Piston Model

In this section the model for the crankshaft, connecting rod and piston is derived. Using this model, the instantaneous indicated torque from the combustion pressure and the torque from the oscillating masses (connecting rod and piston) can be calculated.

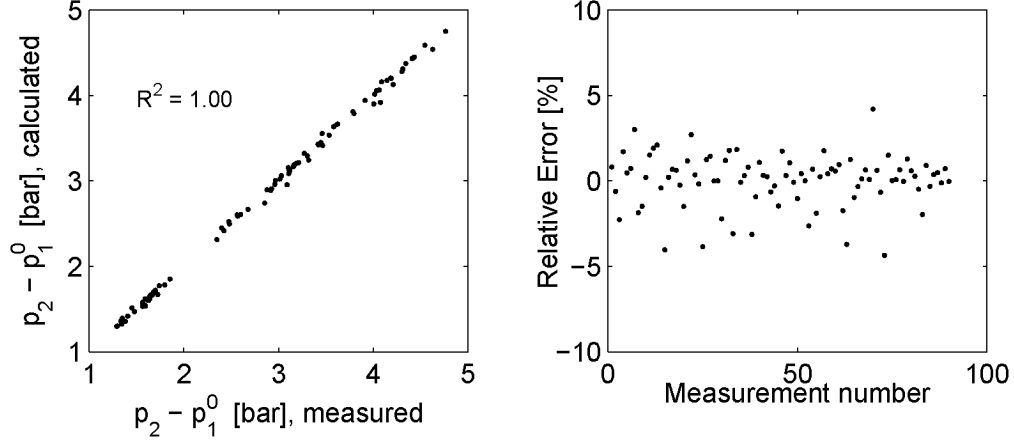


Figure 3.6: Measured and calculated pressure differences $p_2 - p_1^0$ between crank angle position 80 degrees before and after top dead center. The measured data has been obtained from a 6-cylinder 3.2-liter SI engine. The left graph shows the correlation between measured and calculated data, the right graph shows the relative error for all measured operating points and conditions

First, the torque balance on the crankshaft is given:

$$I_{cr}\dot{\omega} = T_i + T_r + T_l = T_n \quad (3.31)$$

The rotational inertia of the crankshaft is denoted by I_{cr} , while ω is the angular velocity of the crankshaft, T_i , T_r , T_l , and T_n are the indicated torque, the torque from reciprocating masses, the load torque, and the resulting net torque, respectively. The friction is absorbed in the load torque. Each torque term is explained in more detail below.

$$T_i(\theta) = A_p p(\theta) f(\theta) \quad (3.32)$$

$$f(\theta) = \frac{S}{2} \left(\sin(\theta) + \frac{\lambda_p}{2} \sin(2\theta) \right) \quad (3.33)$$

The indicated torque T_i is calculated based on the in-cylinder pres-

sure $p(\theta)$. The product of the piston surface area and the in-cylinder pressure, $A_p p(\theta)$, is the pressure force acting on the piston. The function $f(\theta)$ relates the pressure force to the torque at the crankshaft. It is an approximation of the crank-slider kinematics. The symbols S and $\lambda_p = S/(2L)$ denote the stroke and the ratio between half of the stroke and the length of the connecting rod L .

$$T_r(\theta) = -m_r \ddot{x} f(\theta) \quad (3.34)$$

$$= -m_r \frac{S}{2} \omega^2 (\cos(\theta) + \lambda_p \cos(2\theta)) f(\theta) \quad (3.35)$$

The reciprocating torque T_r is calculated based on the acceleration \ddot{x} of the reciprocating mass m_r . The expression for \ddot{x} is an approximation of the acceleration imposed by the crank-slider kinematics. The load torque T_l is usually unknown, but its changes within the duration of one engine cycle are small, due to the transfer behavior of the drive train (e.g. see [46]). Since only the angular velocity at the firing frequency or higher frequencies are of interest (see Sect. 3.6), the unknown load torque can be neglected for the purpose of this text.

3.4 Phase of the Angular Velocity

In this section, the procedure for calculating the phase of the crankshaft angular velocity at the engine firing frequency is described in detail. The procedure can be divided into two steps:

1. Discrete Fourier transformation of the instantaneous crankshaft angular velocity to obtain the spectrum and
2. extracting the phase information at the engine firing frequency from the spectrum.

After explaining these two steps, some simplifications are proposed and calibration issues are discussed.

3.4.1 Discrete Fourier Transformation

The signal x , which is to be Fourier-transformed, consists of $N = 720$ samples. The sampling interval is $\Delta\theta = 1$ degree crank angle. Thus the signal covers one full engine cycle. The sample taken at the crank angle positions $\theta = n\Delta\theta$, $n = 0, \dots, N - 1$, is denoted by $x(n)$. Then the formula for the complex amplitude X_m at the frequency $f = \frac{m}{N\Delta\theta}$ is given as:

$$X_m = \sum_{n=0}^{N-1} x(n)e^{-j\frac{2\pi m n}{N}} \quad (3.36)$$

For the purpose of this work, the signal x is either the instantaneous crankshaft velocity $\omega(\theta)$ or the net torque at the crankshaft T_n .

3.4.2 Phase Information

The complex amplitude X_m can be written as

$$X_m = |X_m| e^{j\varphi_m},$$

where $|X_m|$ is the magnitude and φ_m is the phase of X_m . The phase φ_m is calculated as

$$\varphi_m = \arctan\left(\frac{\text{Imag}(X_m)}{\text{Real}(X_m)}\right). \quad (3.37)$$

3.4.3 Simplifications

The following two simplifications substantially reduce the computational burden for the calculation of the phase of the crankshaft angular velocity at the engine firing frequency:

1. The only property of interest in the spectrum of the crankshaft angular velocity is the phase at the engine firing frequency. It is therefore inefficient to calculate the whole spectrum and it is suggested to only partially Fourier-transform the angular velocity and to evaluate (3.36) and (3.37) only for the case where m matches the number of cylinders of the engine, which corresponds to the engine firing frequency. Since all the experimental data was obtained from a 6-cylinder engine, m is set to $m = 6$ and the phase of the crankshaft angular velocity at the firing frequency is denoted as $\varphi_{\omega, m=6}$. For simplicity, the suffix $m = 6$ will be omitted for the remainder of the text.

2. The crankshaft angular velocity is calculated by integrating the net torque on the crankshaft and dividing the result by the rotational inertia I_{cr} (3.31). The fact that the change of operating conditions is small during the duration of one engine cycle allows the assumption of a steady-state operation for the duration of one engine cycle. The integration may then be carried out in the frequency domain, where 'integration' is equal to shifting the phase by $C_{\varphi} = -90$ degrees and dividing the magnitude of the complex amplitude by its frequency. Therefore, the phase of the crankshaft angular velocity can be calculated as

$$\hat{\varphi}_{\omega} = \varphi_{T_n} + C_{\varphi}, \quad (3.38)$$

where $\hat{\varphi}_{\omega}$ is the estimated phase of the crankshaft angular velocity at the engine firing frequency and φ_{T_n} is the phase of the net torque at the engine firing frequency.

Table 3.1: Calibrated phase differences between model and measurements

ΔC_φ^0 [deg]	$n = 1000$ [rpm]	$n = 2000$ [rpm]	$n = 3000$ [rpm]
$p_{im} = 0.30$ bar	9.30	11.76	15.39
$p_{im} = 0.50$ bar	9.30	-0.40	18.26
$p_{im} = 0.65$ bar	11.20	0.70	20.06

3.5 Calibration

Comparing the phase of the crankshaft angular velocity calculated from measured data with the estimated phase, a remaining difference ΔC_φ can be observed:

$$\varphi_\omega - \hat{\varphi}_\omega = \Delta C_\varphi \quad (3.39)$$

This remaining difference is attributed to neglected crankshaft elasticity and influences from belt-driven devices connected to the crankshaft. In order to avoid more complex modeling, the remaining difference ΔC_φ is derived from measured data (data set **A**) and stored in the reference map as ΔC_φ^0 for each reference operating point (see Table 3.1).

3.6 Flame Speed Correction

Based on the material presented so far in this chapter, an adaption scheme of the flame development angle θ_d and the rapid burning angle θ_b can be derived. Recalling that

1. the angles θ_d and θ_b are related to the flame speed by

$$\theta_d = \text{const} \cdot k_{sf}^{-2/3} \quad (3.40)$$

$$\theta_b = \text{const} \cdot k_{sf}^{-2/3} \quad (3.41)$$

and that they thus are proportional to each other, and that

2. the estimated phase of the crankshaft angular velocity $\hat{\varphi}_\omega$ is related to θ_d and θ_b ,

the following adaption scheme can be outlined:

1. The angles θ_d and θ_b are estimated based on the spark timing θ_{sa} , the fuel/air equivalence ratio ϕ , the engine speed n , and the inlet manifold pressure p_{im} , as depicted in the pressure estimation path in Fig. 1.5 (Eqs. (3.6) and (3.7)).
2. From the estimated values of θ_d and θ_b , the heat-release profile and the in-cylinder pressure can be calculated (Eq. (3.3)).
3. The model of the crankshaft and piston-connecting rod assembly allows the calculation of the instantaneous net torque on the crankshaft T_n (Sect. 3.3).
4. The phase of the net torque at the engine firing frequency is calculated. Adding $C_\varphi = -90$ deg and correcting with ΔC_φ (Table 3.1) yields the phase of the crankshaft angular velocity at the engine firing frequency (Sect. 3.4).
5. The true crankshaft angular velocity is measured and partially Fourier-transformed to extract the phase at firing frequency.
6. The difference between the calculated and the measured phase at the firing frequency, $\Delta\varphi_\omega$, is a measure for the difference between

the flame speed underlying the in-cylinder pressure estimation and the true flame speed,

$$\Delta\varphi_\omega = \varphi_\omega - \hat{\varphi}_\omega. \quad (3.42)$$

7. The value of $\Delta\varphi_\omega$ is used to correct k_{sf} in Eqs. (3.6) and (3.7).

The adaption rule is formulated as:

$$s_{k+1} = s_k + k_i \Delta\varphi_{\omega,k} \quad (3.43)$$

$$(k_{sf})_{k+1}^{-2/3} = 1 - (k_p \Delta\varphi_{\omega,k} + s_k) \quad (3.44)$$

The equations of the adaption rule are evaluated once per engine cycle k . They comprise a proportional part and an integrating part. The proportional part allows for fast adaption, while the integrating part eliminates any steady-state error.

The gain $(k_{sf})^{-2/3}$ is acting as a multiplicative correction in (3.6) and (3.7). This is more advantageous than an additive correction for the following reason: Non-measured disturbances (such as non-measured air-humidity, charge temperature, or EGR rate) affecting the flame speed are not related to a specific operating point. Their effect on the flame speed thus remains, while the operating conditions may change. Since θ_d and θ_b are proportional to $(k_{sf})^{-2/3}$, it makes sense to apply a multiplicative correction.

The parameters k_p and k_i determine the transient behavior of the pressure estimation. They have to be chosen in such a way that a good compromise between a fast response to changing operating conditions and a reliable rejection of the cyclic variability of the combustion is achieved. Furthermore, k_p and k_i have to ensure the stability of the adaption algorithm. The stability, the robustness, and the performance are discussed in the next subsection.

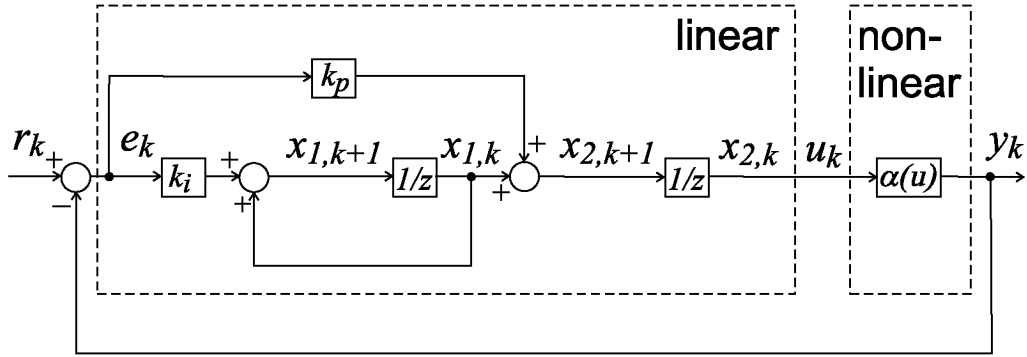


Figure 3.7: Signal-flow graph of the system

3.6.1 Stability, Robustness, and Performance of the Adaption Algorithm

In order to assess the stability, the robustness, and the performance of the pressure adaption algorithm, the system depicted in Fig. 3.7 is used for the investigation. It consists of a dynamic linear part and a static non-linear part. The linear part represents the adaption rule, whereas the non-linear part represents the calculation of the phase based on the correction of the flame speed. The time delay of the duration of one engine cycle introduced by measuring and processing the crankshaft rotational velocity is added to the linear part of the system. The linear part is then given as:

$$\mathbf{x}_{k+1} = \mathbf{F} \mathbf{x}_k + \mathbf{G} e_k \quad (3.45)$$

$$u_k = \mathbf{C} \mathbf{x}_k ,$$

where

$$\mathbf{F} = \begin{bmatrix} 1 & 0 \\ 1 & 0 \end{bmatrix} \quad \mathbf{G} = \begin{bmatrix} k_i \\ k_p \end{bmatrix}$$

$$\mathbf{C} = \begin{bmatrix} 0 & 1 \end{bmatrix} .$$

From the state space representation the transfer function of the linear part can be derived:

$$G(z) = \frac{k_i + (z - 1)k_p}{z(z - 1)} \quad (3.46)$$

The static non-linearity $\alpha(u) = y/u$ represents the transfer behavior from the flame speed correction to the phase of the crankshaft angular velocity. The input u is the deviation of the flame speed correction from the nominal setting, $u = \Delta(k_{s_f})^{-2/3} = 1 - (k_{s_f})^{-2/3}$ (see (3.44)), and the output y is the deviation of the actual phase based on the phase at nominal operating conditions $y = \Delta\varphi_\omega = \varphi_\omega - \varphi_\omega^0$. The static non-linearity $\alpha(u)$ is depicted in Fig. 3.8. The same figure shows the two lines $\alpha_1 u$ and $\alpha_2 u$ which define a sector enclosing $\alpha(u)$.

The Circle Criterion [2] states that the closed loop of the system depicted in Fig. 3.7 is stable, if the Nyquist curve of the linear part of the system does not intersect the circle with center $M = -1/2(1/\alpha_1 + 1/\alpha_2)$ and radius $R = 1/2(1/\alpha_1 - 1/\alpha_2)$. In Fig. 3.9 the Nyquist curve is depicted for two combinations of k_p and k_i . Clearly, the Nyquist curve does not intersect the circle, which ensures stability of the system. Furthermore, the minimum distance between the Nyquist curve and the circle, d_{min} , can be understood as a measure of the robustness of the system. Figure 3.10 shows the minimum distance d_{min} between the Nyquist curve and the circle $\{M, R\}$ for a

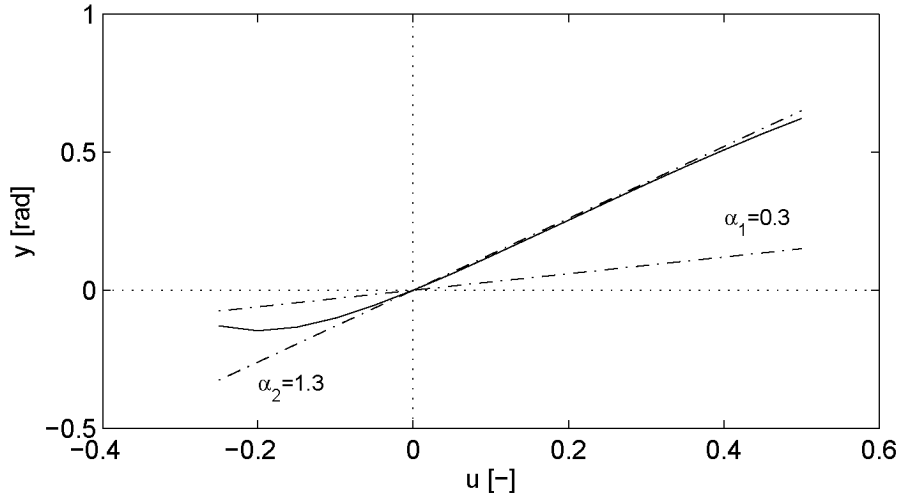


Figure 3.8: Static non-linearity with sector boundaries

range of values for k_p and k_i .

The step response of the system is depicted in Fig. 3.11 for two combinations of k_p and k_i .

3.6.2 Cylinder-Individual Pressure Estimation

Conceptually it is possible to estimate the in-cylinder pressure separately for each cylinder. This would require an adequate masking of the measured crankshaft angular velocity, such that the properties of each cylinder could be isolated. Care would have to be taken not to introduce any "artificial" frequencies into the signal by choosing sharp boundaries of the mask and to catch as much useful information in the masked window as possible. However, this is beyond the scope of this work and will not be discussed here.

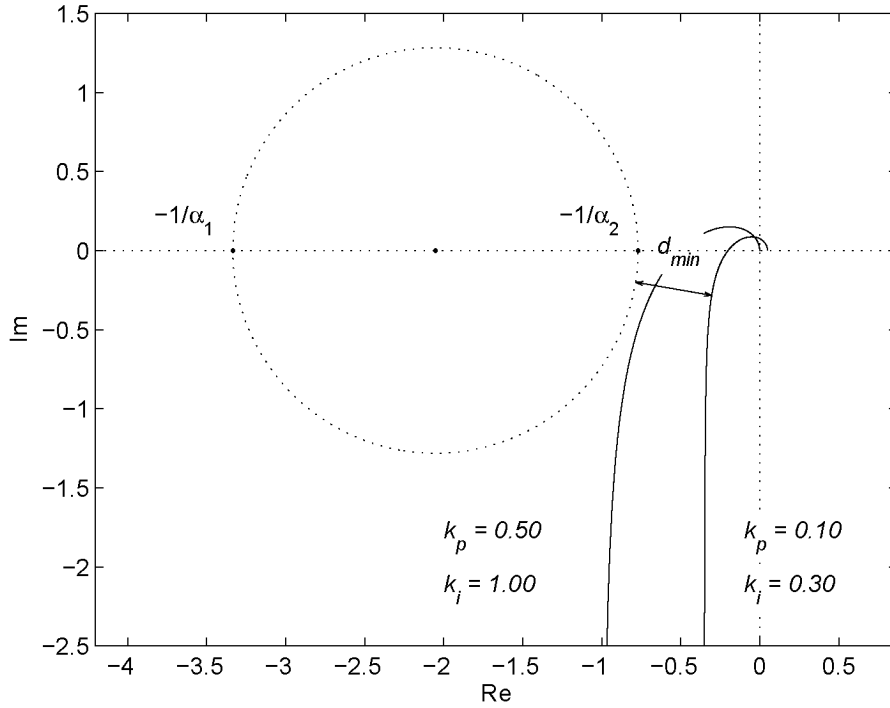


Figure 3.9: Nyquist curve of the linear part of system (3.45) and circle with center $M = -1/2(1/\alpha_1 + 1/\alpha_2)$ and radius $R = 1/2(1/\alpha_1 - 1/\alpha_2)$ for two combinations of k_p and k_i . The minimum distance between the circle and the Nyquist curve, d_{min} , serves as a measure for robustness

3.6.3 Calibration and Validation

Calibration

The calibration of the pressure estimation model follows a two-step procedure. First, the parameters for nominal operating conditions (e.g. nominal spark advance and nominal fuel/air equivalence ratio) are stored in reference maps. Second, the parameters needed to describe the pressure changes due to changes of θ_{sa} and ϕ are identified. For calibration, the measured data at nominal operating condition throughout the whole operating range plus the spark advance and fuel/air equivalence ratio variations at an engine speed of $n = 2000$ rpm and an inlet manifold pressure $p_{im} = 0.5$ bar are used. Table 3.2

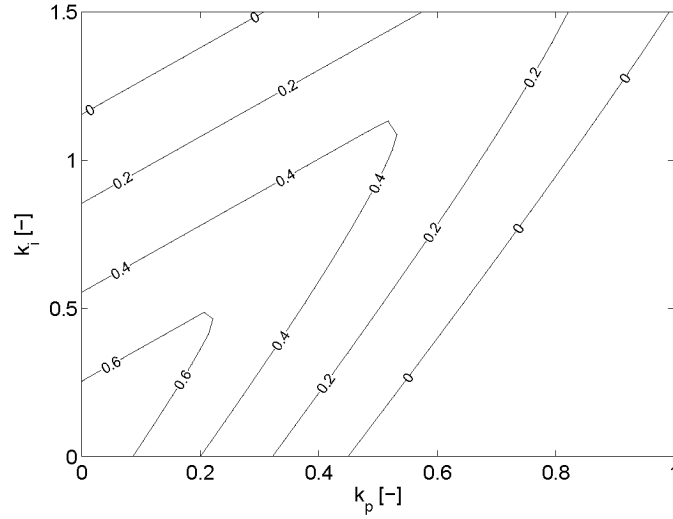


Figure 3.10: Contour plot of the minimum distance d_{min} between the Nyquist curve and the circle in Fig. 3.9 as a function of k_p and k_i

lists the parameters identified with the calibration data set.

Steady-State Validation

For the steady-state validation of the flame speed correction, the following three cases are studied (compare with the signal-flow graph in Fig. 3.12):

1. The in-cylinder pressure is calculated without the adaption path ($a = 0$ in Fig. 3.12) and without any disturbances ($d_{\theta_a} = d_{\theta_b} = 0$). The resulting peak pressures (PP) and peak pressure locations (PPL) are compared to measured data obtained from the 6-cylinder 3.2-liter SI engine. The data is depicted in the graphs (a) and (b) of Fig. 3.13.
2. The in-cylinder pressure is calculated while a randomly chosen offset ($d_{\theta_a} \neq 0, d_{\theta_b} \neq 0$) is added to the flame development and the rapid burning angle. The adaption algorithm is disabled

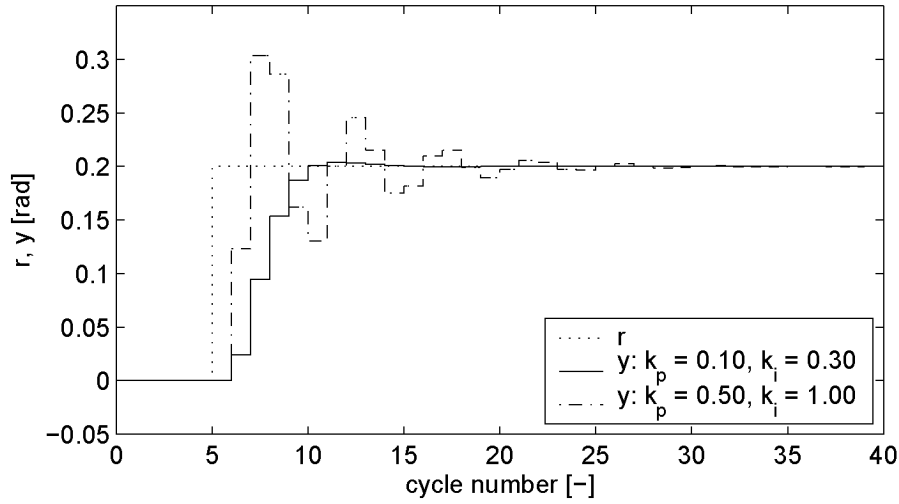


Figure 3.11: Step response of the system for two combinations of k_p and k_i

($a = 0$). The results are depicted in the graphs (c) and (d) of Fig. 3.13.

3. The in-cylinder pressure is calculated while randomly chosen offsets to θ_d and θ_b are added. The adaption algorithm is enabled ($a = 1$) in order to to compensate for the offsets. The data is depicted in the graphs (e) and (f) of Fig. 3.13.

Figure 3.13 clearly demonstrates the capabilities of the adaption algorithm: The offset of the input data is compensated to a considerable extent by the feedback of the measured crankshaft angular velocity.

Transient Validation

Figures 3.14 to 3.16 demonstrate the transient behavior of the pressure estimation when the phase-controlled adaption algorithm is applied.

Table 3.2: Reference parameters and calibration data

Parameter	Calibration Data	Equation
θ_d^0, θ_b^0	data set A	(3.6) - (3.7)
θ_{sa}^0, ϕ^0	data set A	(3.6) - (3.7)
p_1^0	data set A	(3.29)
$\Delta p^0, \theta_{80}^0$	data set A	(3.30)
ΔC_φ^0	data set A	(3.39)
coefficients of $f_{sa}(\theta_{sa}), f_\phi(\phi),$ $g_{sa}(\theta_{sa}), g_\phi(\phi),$	data set B ⁻	(3.6) - (3.7)
$c_{\Delta p}$	data set A ⁺	(3.30)

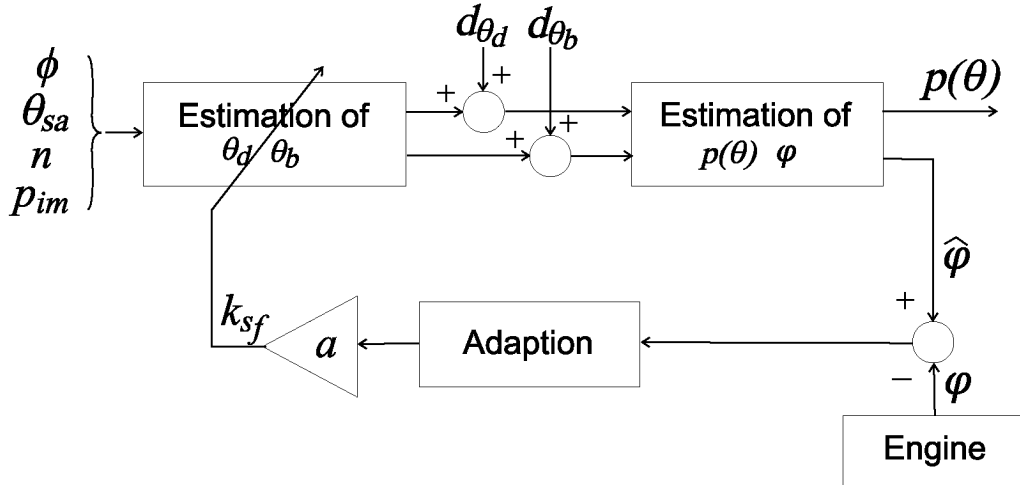


Figure 3.12: Signal-flow graph of the adaption algorithm. The disturbances d_{θ_d} and d_{θ_b} are added to θ_d and θ_b . Setting the flag $a = 1$ enables the adaption algorithm, setting $a = 0$ disables the adaption

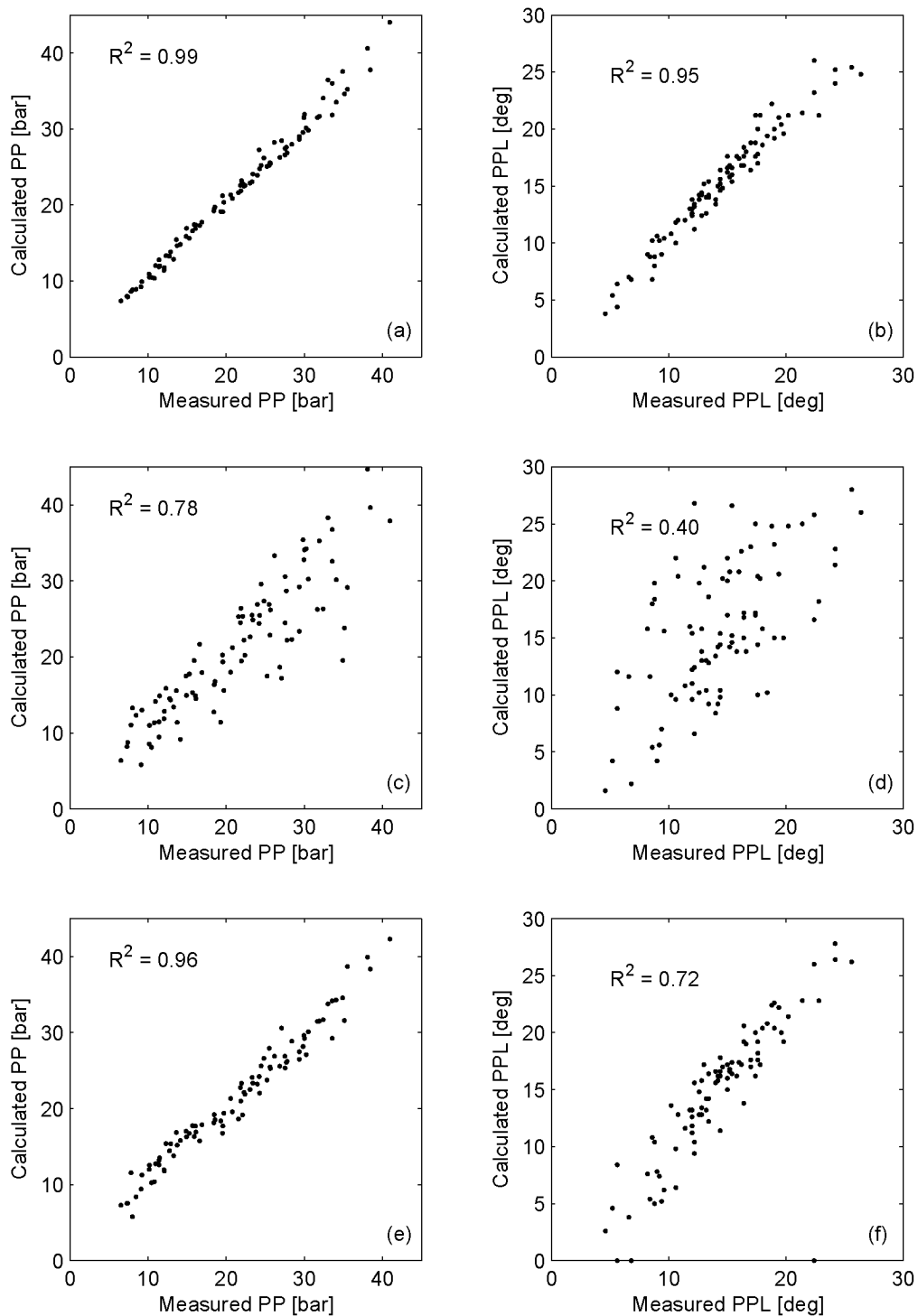


Figure 3.13: The graphs (a) and (b) show the peak pressure (PP) and its location (PPL) together with measured data when the parameter adaption path is disabled ($a = 0$ in Fig. 3.12). The graphs (c) and (d) show PP and PPL when a randomly chosen offset is added to the flame development and rapid burning angle (adaption still disabled). The graphs (e) and (f) show PP and PPL when the parameter adaption path is enabled in order to compensate for the disturbed flame development and rapid burning angles

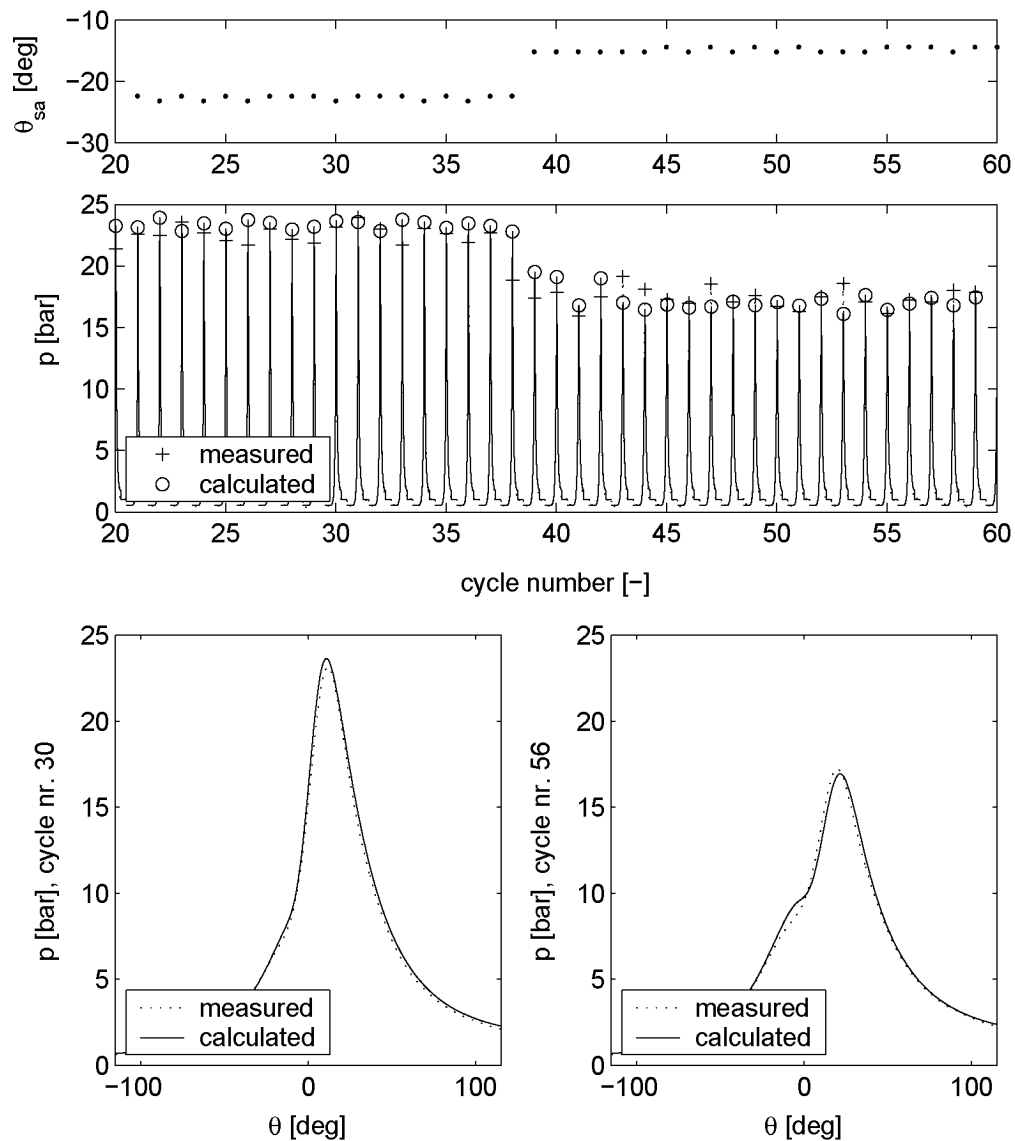


Figure 3.14: The graph at the top shows the spark advance. The graph in the middle compares the measured and the estimated in-cylinder pressure during a spark advance step at $p_{im} = 0.5$ bar and $n = 1000$ rpm. The graphs at the bottom show the estimated in-cylinder pressure for one cycle before the spark advance change and one cycle after the in-cylinder pressure has settled to the new steady-state values

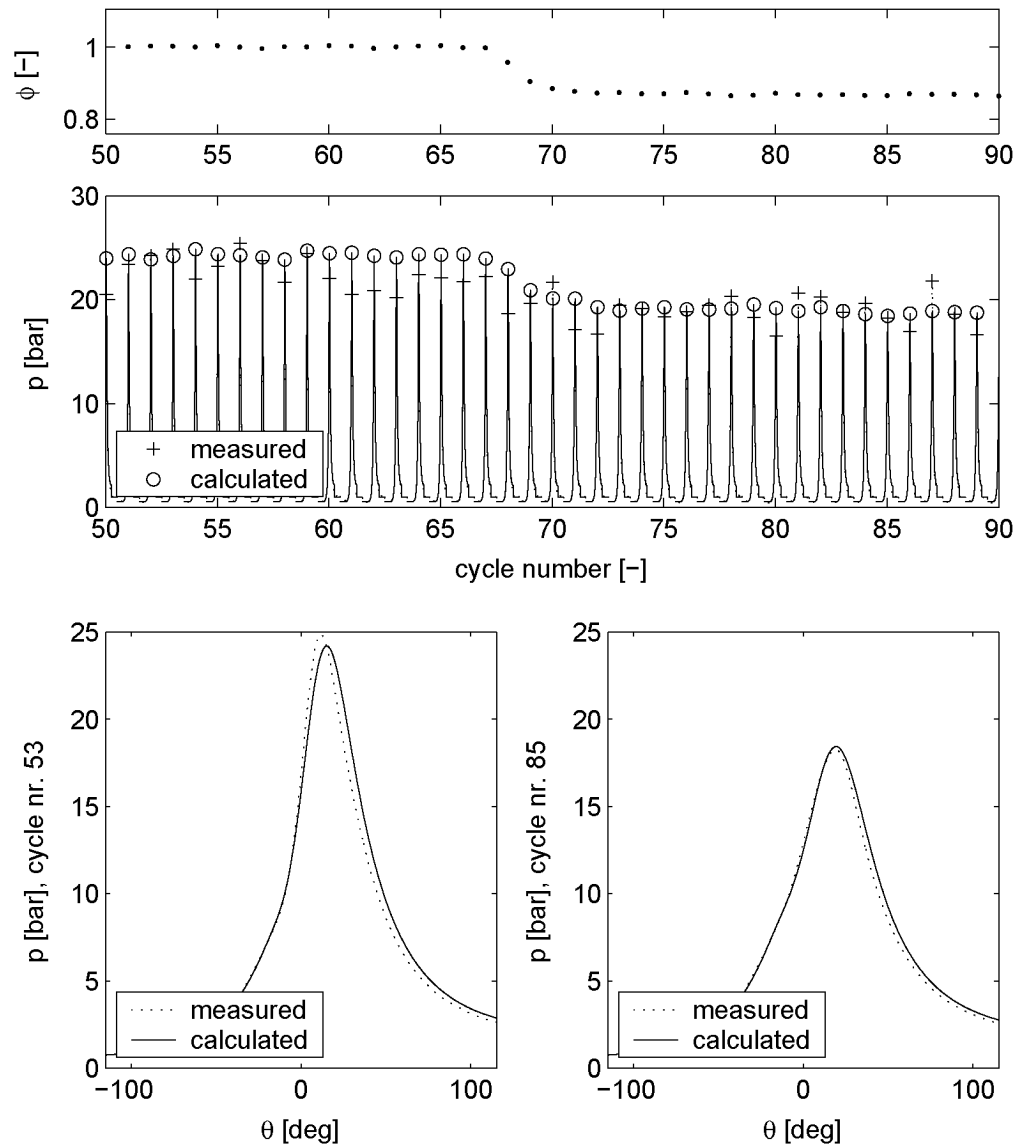


Figure 3.15: The graph at the top shows the fuel/air equivalence ratio ϕ . The graph in the middle compares the measured and the estimated in-cylinder pressure during a ϕ step at $p_{im} = 0.5$ bar and $n = 2000$ rpm. The graphs at the bottom show the estimated in-cylinder pressure for one cycle before the fuel/air equivalence ratio change and one cycle after the in-cylinder pressure has settled to the new steady-state values

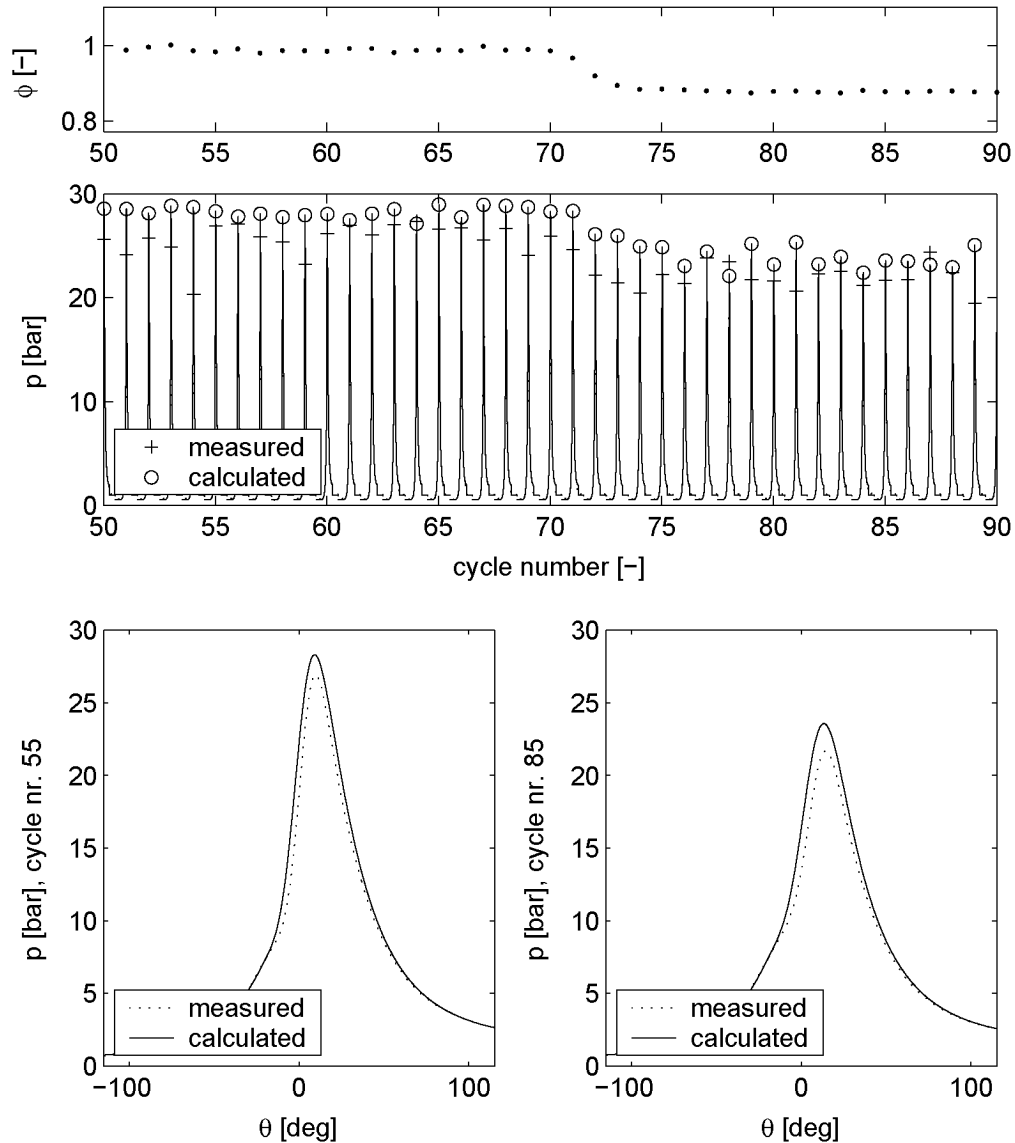


Figure 3.16: The graph at the top shows the fuel/air equivalence ratio ϕ . The graph in the middle compares the measured and the estimated in-cylinder pressure during a ϕ step at $p_{im} = 0.5$ bar and $n = 3000$ rpm. The graphs at the bottom show the estimated in-cylinder pressure for one cycle before the fuel/air equivalence ratio change and one cycle after the in-cylinder pressure has settled to the new steady-state values

3.7 Comparison to Sliding Mode Observer (SMO)

In this section the pressure estimation method described in the first part of the chapter is compared to the estimation of the in-cylinder pressure using a Sliding Mode Observer (SMO).

Kao and Moskwa in [37] and Shiao and Moskwa in [57] presented a pressure estimation method using an SMO. Their method can be summarized as follows: The two states in-cylinder pressure and crankshaft angular velocity are calculated using a known but fixed heat-release profile, a 1-zone process simulation model, and the kinematics of the piston, connecting rod and crankshaft. The difference between measured and calculated crankshaft angular velocity is used to correct the derivatives of the state variables. Figure 3.17 depicts the corresponding signal-flow graph.

The basic differences between the two pressure estimation methods are: (A) The SMO estimates the derivative of the in-cylinder pressure and the crankshaft angular velocity with respect to the crank angle, while the phase-controlled pressure estimation algorithm estimates the flame development and the rapid burning angle. (B) The sampling time of the SMO is of the order of one degree crank angle. In contrast, the phase-controlled algorithm updates the model parameters θ_d and θ_b once per engine cycle. (C) In the framework of the phase-controlled algorithm, the load torque is assumed to be constant over one engine cycle and thus can be neglected. The SMO assumes that the load torque is available through measurement or observer-based estimation.

This has consequences on how the two algorithms perform (see Table 3.3). **Observability:** The gain $A_p f(\theta)$ in (3.32), which relates the in-cylinder pressure to the torque at the crankshaft, disappears for the crankshaft positions top dead center (TDC) and bottom dead center (BDC) and is small for positions close to TDC and BDC, thus

Table 3.3: Differences between the Sliding Mode Observer and the phase-controlled pressure estimation algorithm.

	Phase-controlled algorithm	Sliding Mode Observer
Estimated variables	θ_d, θ_b	$\frac{dp(\theta)}{d\theta}, \frac{d\omega(\theta)}{d\theta}$
Error dynamics	about 10 cycles	< 1 cycle
Update rate	1 cycle	1 crank angle degree
Observability		$p(\theta = 0)$ not observable

making the in-cylinder pressure unobservable at these positions. Inverting the model, the gain $(A_p f(\theta))^{-1}$ relating the indicated torque to the in-cylinder pressure becomes large for crankshaft positions close to TDC or BDC and infinite at TDC and BDC. This makes it difficult for the SMO to accurately correct the in-cylinder pressure close to TDC, because even small differences between estimated and measured crankshaft angular velocity lead to strong corrections of the estimated in-cylinder pressure.

In contrast, the phase-controlled algorithm estimates the flame development and the rapid burning angle once per cycle. For this purpose, the rotational crankshaft angular velocity is recorded during one engine cycle and then partially Fourier-transformed to extract the phase at the engine firing frequency. This method avoids the issues associated with the poor observability mentioned above.

Error dynamics: The SMO works with a sample time on the order of one degree crank angle. It is therefore capable of reacting to changing operating conditions within one single engine cycle. The phase-controlled algorithm updates the model parameters once per engine cycle, which leads to a reaction time of several engine cycles.

The remainder of this section provides a summary of the governing

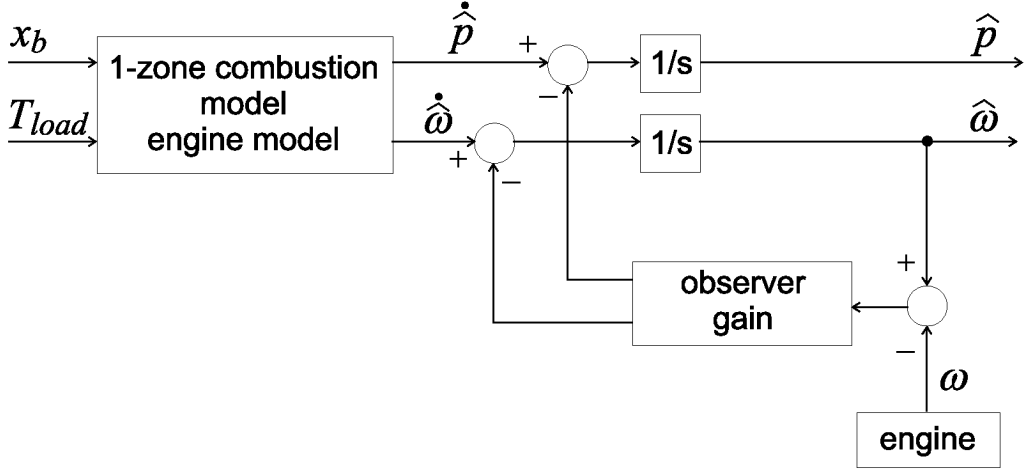


Figure 3.17: Signal-flow graph of the Sliding Mode Observer (SMO) described in [57]. The model has two inputs (the reference heat-release profile and the load torque), two state variables (the in-cylinder pressure and the crankshaft angular velocity) and two outputs (both state variables). The estimated and the measured crankshaft angular velocity is compared and the difference serves to correct the derivatives of the state variables.

equations of the SMO taken from [57]. Then the accuracies for steady-state and for transient operation of the two estimation methods are compared.

3.7.1 Governing Equations of the SMO

The equations in this subsection are taken from [57]. The symbols are maintained as used in that publication.

The torque balance on the crankshaft is formulated as:

$$J(\theta)\ddot{\theta}(t) + \frac{1}{2} \frac{dJ(\theta)}{d\theta} \dot{\theta}^2 = T_{ind} - T_{grav} - T_{fric} - T_{load} \quad (3.47)$$

The inertia $J(\theta)$ of the crankshaft, connecting rod, and piston is not detailed in [57], but may be approximated by the following function:

$$J(\theta) = I_{cr} + m_r \left[\frac{S}{2} \left(\sin(\theta) + \frac{\lambda_p}{2} \sin(2\theta) \right) \right]^2 \quad (3.48)$$

The gravity torque T_{grav} is neglected. The friction torque T_{fric} is calculated based on a mean value model with the engine speed as input and the displaced volume as model parameter. The load torque T_{load} is assumed to be available from a torque transducer or from a torque observer. The indicated torque T_{ind} is calculated based on the in-cylinder pressure as:

$$T_{ind} = \sum_i^n P_i(t) A_p L_{tor,i}(\theta) \quad (3.49)$$

$$L_{tor}(\theta) = R \sin \theta + \frac{R \cos \theta + e}{\sqrt{L^2 - (R \sin \theta + e)^2}} \quad (3.50)$$

The effective moment arm L_{tor} is calculated from the crankshaft-connecting rod mechanism. The symbols A_p , R , L , e , and n denote the piston surface area, the radius of the crankshaft, the length of the connecting rod, the piston offset, and the number of cylinders. The in-cylinder pressure $P(t)$ is derived from a 1-zone 0-dimensional process model

$$dQ_{ch} = \frac{\gamma}{\gamma - 1} P dV + \frac{1}{\gamma - 1} V dP + dQ_{ht}, \quad (3.51)$$

where γ is the ratio of the specific heats, P is the in-cylinder pressure, V is the volume of the combustion chamber, and Q_{ht} is the heat transferred to the cylinder wall, which is calculated using Eichelberg's formula. The combustion heat release Q_{ch} is calculated based on a heat-release profile approximated by the Vibe function:

$$Q_{ch} = m_f Q_{LHV} \left[1 - e^{a \left(\frac{\theta - \theta_{cs}}{\theta_{ce} - \theta_{cs}} \right)^{m_v + 1}} \right] \quad (3.52)$$

Using the formulas above, the two state variables crankshaft an-

gular velocity $\omega(t)$ and in-cylinder pressure $P(t)$ are written as

$$\dot{\omega} = f_1 + d_1(t) \quad (3.53)$$

$$\dot{P} = f_2 + d_2(t), \quad (3.54)$$

where f_1, f_2 describe the non-linear system dynamics and $d_1(t), d_2(t)$ are disturbances. Then, the following structure for the Sliding Mode Observer is defined:

$$\dot{\hat{\omega}} = \hat{f}_1 - \alpha_1 \tilde{\omega} - K_\omega \text{sat} \left(\frac{\tilde{\omega}}{\eta} \right) \quad (3.55)$$

$$\dot{\hat{P}} = \hat{f}_2 - \alpha_2 \tilde{\omega} - K_P \text{sat} \left(\frac{\tilde{\omega}}{\eta} \right) \quad (3.56)$$

Here, $\hat{\omega}$ and \hat{P} represent the estimated state variables. The difference between the estimated and measured crankshaft angular velocities is denoted by $\tilde{\omega}$. The function $\text{sat}(\tilde{\omega}/\eta)$ is defined as follows:

$$\text{sat} \left(\frac{\tilde{\omega}}{\eta} \right) = \begin{cases} \tilde{\omega}/|\tilde{\omega}| & \text{if } |\tilde{\omega}| \geq \eta \\ \tilde{\omega}/\eta & \text{if } |\tilde{\omega}| < \eta \end{cases} \quad (3.57)$$

The linear term gains α_1 and α_2 are chosen such that the system

$$\dot{\tilde{\mathbf{x}}} = [\mathbf{A} - \mathbf{HC}] \tilde{\mathbf{x}} \quad (3.58)$$

has two desired poles p_1 and p_2 . The estimation error of the state variables is denoted by $\tilde{\mathbf{x}}$. The matrix \mathbf{A} is derived from the non-linear system dynamics by linearization:

$$\mathbf{A} = \begin{bmatrix} \frac{\partial f_1}{\partial \omega} & \frac{\partial f_1}{\partial P} \\ \frac{\partial f_2}{\partial \omega} & \frac{\partial f_2}{\partial P} \end{bmatrix}$$

The output of the system (3.58) is the crankshaft angular velocity only, thus

$$\mathbf{C} = \begin{bmatrix} 1 & 0 \end{bmatrix},$$

and the feedback matrix \mathbf{H} is composed of the two linear term gains:

$$\mathbf{H} = \begin{bmatrix} \alpha_1 & \alpha_2 \end{bmatrix}^T$$

The switching gains K_ω and K_P are chosen such that the system is converging to the sliding state. In [57] it is shown that this requires K_ω and K_P to obey

$$K_\omega > |\Delta f_1 + \alpha_1 \tilde{\omega}| \quad (3.59)$$

$$K_P = \left(-\lambda_0 - \frac{\gamma}{V(\theta)} \dot{V}(\theta) \right) \frac{J(\theta)}{A_p L_{tor}(\theta)} K_\omega, \quad (3.60)$$

where the modeling error Δf_1 is assumed to be bounded. The gain λ_0 allows the adjustment of the gain for the non-linear pressure correction in (3.56).

3.7.2 Accuracy at Steady-State Operation

For the first comparison the following performance criterion J as a measure of the steady-state accuracy is defined:

$$J = \sum_{\theta_i=-80}^{+80} (p_{meas}(\theta_i) - p_{sim}(\theta_i))^2 \quad (3.61)$$

The sensitivity S of the accuracy to model parameter changes

$$S = \frac{J(m_{r,2}) - J(m_{r,1})}{m_{r,2} - m_{r,1}} \frac{m_{r,1}}{J(m_{r,1})} \quad (3.62)$$

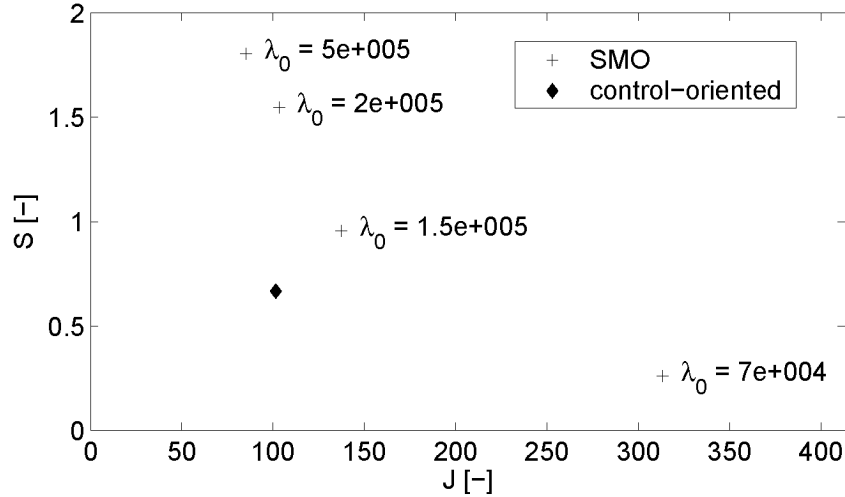


Figure 3.18: Sensitivity S of the steady-state accuracy against cost function J . The observer gain λ_0 for the correction of the derivative of the in-cylinder pressure is varied. As shown, it determines the steady-state accuracy of the SMO, whereas the steady-state accuracy of phase-controlled algorithm shows no dependence on the adaption gains k_p and k_i

was defined using the reciprocating mass m_r as the uncertain parameter. This parameter is chosen because it influences the shape of the instantaneous crankshaft angular velocity. Instead of the reciprocating mass, any other model parameter that affects the shape of the instantaneous crankshaft angular velocity could have been chosen. The comparison of the SMO and from the phase-controlled algorithm in Fig. 3.18 shows that the latter is less sensitive to model uncertainties. For steady-state estimations, therefore, the use of the phase-controlled algorithm offers certain improvements.

3.7.3 Comparison of the Transient Responses

As a next step, the spark advance step responses of both methods are compared to experimental data. This data was recorded during a spark advance step from nominal to late at the operating point $n = 1000$ rpm and $p_{im} = 0.5$ bar. Then the in-cylinder pressure was

estimated using the SMO and the phase-controlled algorithm. The spark advance input to the models was kept unchanged in order to study the adaption performance in the absence of the feedforward estimation. The estimated pressure data from the SMO and from the phase-controlled method were recorded and compared. Figure 3.19 shows the spark advance step response of the SMO and Fig. 3.20 shows the step response of the phase-controlled method.

The response of the SMO demonstrates its capability to react on a cycle-to-cycle basis to changing operating conditions. The two graphs at the bottom of Fig 3.19, however, show that the accuracy suffers, particularly at changed operating conditions and crankshaft positions close to TDC. The in-cylinder pressure trace exhibits distortions that cannot be explained from combustion thermodynamics. This is of minor concern if the in-cylinder pressure is used for the calculation of the indicated torque. In contrast, the effect of the in-cylinder pressure on the burned gas temperature cannot be neglected if the NO formation in the combustion chamber is to be estimated.

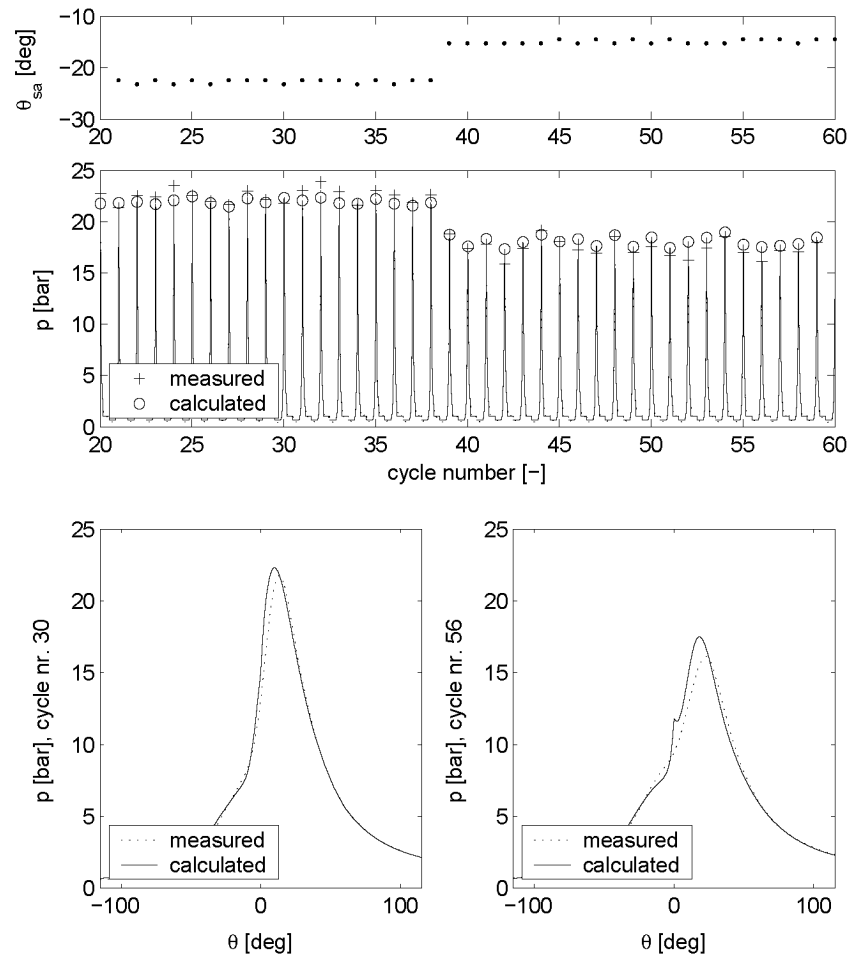


Figure 3.19: The graph at the top shows the spark advance. The graph in the middle compares the calculated in-cylinder pressure using the SMO to the measured data during a spark advance step at $n = 1000$ rpm and $p_{im} = 0.5$ bar. The graphs at the bottom depict the details of the in-cylinder pressure

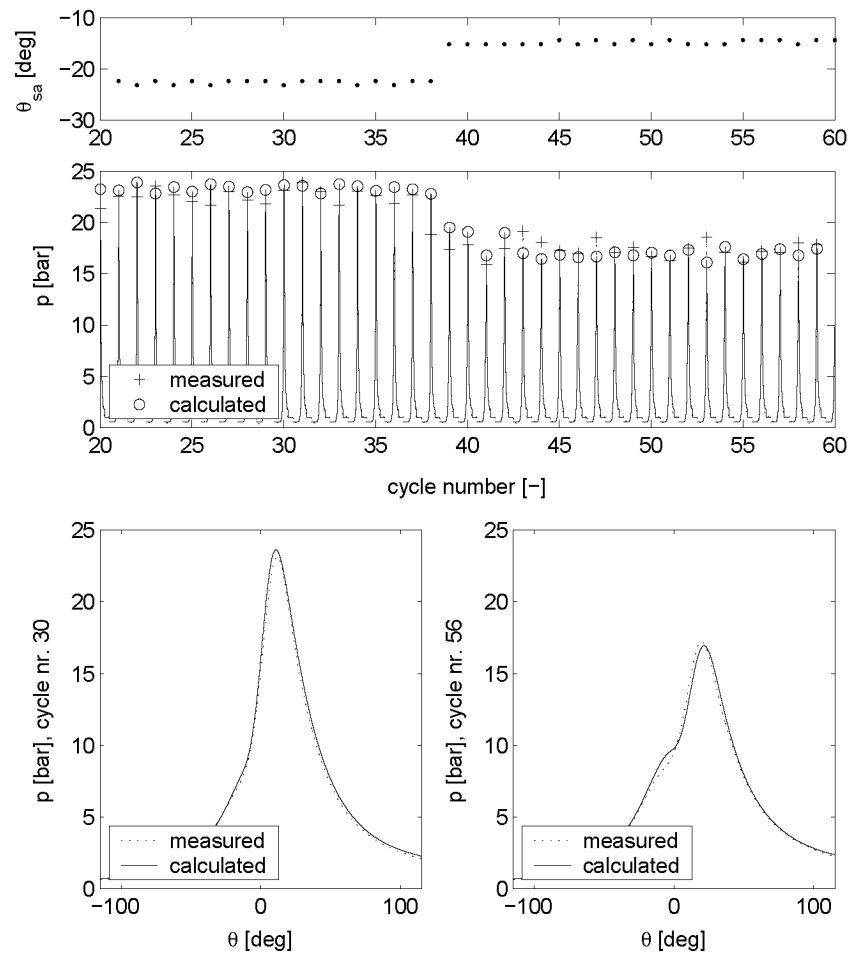


Figure 3.20: The graph at the top shows the spark advance. The graph in the middle compares the calculated in-cylinder pressure using the phase-controlled pressure estimation method to the measured in-cylinder pressure during a spark advance step at $n = 1000$ rpm and $p_{im} = 0.5$ bar. The graphs at the bottom depict the details of the in-cylinder pressure

Chapter 4

Burned Gas Temperature

In this chapter a computationally efficient method to calculate the burned gas temperature is derived. The main focus is on its simplicity in order to keep the computational effort small, while preserving the physically motivated parameters. The chapter is organized as follows. First, a 0-dimensional 2-zone process simulation is formulated in order to generate reference data. Second, a control-oriented model of the burned gas temperature is developed.

4.1 Reference Process Simulation

For the calibration and the validation of the control-oriented model, reference data for the in-cylinder pressure and the temperature is needed. While the in-cylinder pressure can be measured on the test bench, the temperature is not accessible. It is therefore necessary to set up a reference process simulation in order to generate the refer-

ence in-cylinder temperature data. For the purpose of this text, a 0-dimensional 2-zone model was chosen, because it offers a good compromise between realistic modeling of the combustion process and the computational effort required.

4.1.1 Model Equations

The process simulation model consists of two distinct zones separated by the infinitesimally thin flame front as shown in the left-hand graph of Fig. 4.1. In contrast to what the figure suggests, there is no geometric information connected to the zones except their volumes. The zones are denoted as burned gas zone (index b) and unburned gas zone (index u). Each zone has a uniform distribution of pressure, temperature, and gas composition. The pressures in the burned and in the unburned gas zones are equal. It is assumed that no mass enters or escapes the combustion chamber when inlet and outlet valves are closed. The total volume of the cylinder is dictated by the motion of the piston. The five states of the process-simulation model are: The in-cylinder pressure $p(\theta)$, temperature and volume of the burned gas zone, $T_b(\theta)$ and $V_b(\theta)$, and temperature and volume of the unburned gas zone, $T_u(\theta)$ and $V_u(\theta)$. The progress of the combustion is described by the burned mass fraction $x_b(\theta)$, which is assumed to be a predefined function. The result of the process simulation is determined by the initial conditions for pressure, temperature, and volume, p_{IC} , T_{IC} , and V_{IC} , the parameters defining the charge composition, the fuel/air equivalence ratio ϕ and the residual gas mass fraction x_r , as well as the parameters that define the burned mass fraction. Those parameters are the flame development angle θ_d , the rapid burning angle θ_b , and the form factor m_v . The output values of the model are the five state variables. The pressure and the temperature of the burned gas zone are of particular interest, because they serve as inputs to the

NO formation model. After this short description of the model, the governing equations are given below.

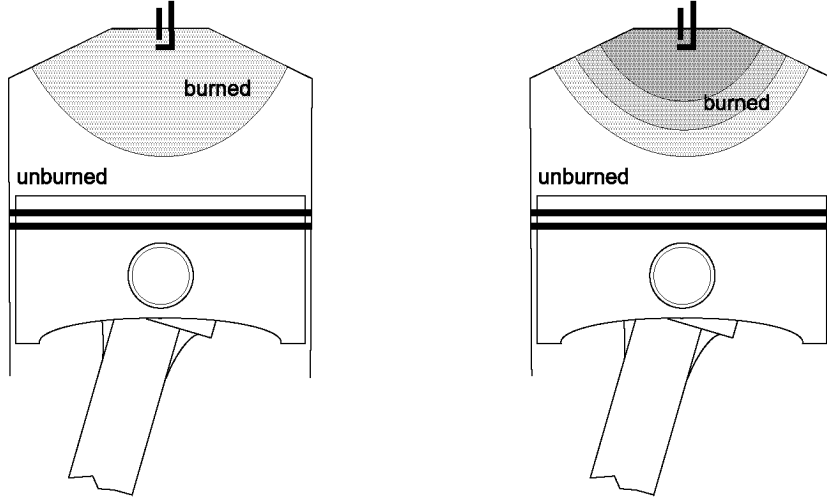


Figure 4.1: Left: 0-dimensional 2-zone process simulation. Right: More realistic sketch of the combustion process. The differently shaded zones depict gas portions that burned at different instants. Among the zones mass is exchanged due to turbulence. Furthermore, each zone is subject to heat exchange with the neighboring zones and with the cylinder wall if contact exists

For each zone in the combustion chamber, the conservation of energy and mass is formulated,

$$dU_i = dQ_{ht,i} + dW_i + \sum_{j \neq i} dm_{ij} h_j \quad (4.1)$$

$$dpV_i + p dV_i = dm_i R_i T_i + m_i dR_i T_i + m_i R_i dT_i \quad (4.2)$$

where dU_i is the internal energy of zone i , $dQ_{ht,i}$ is the heat transfer to the cylinder wall, dW_i is the work, and h_j is the specific enthalpy associated with the mass flow dm_{ij} from zone j to i . The enthalpy h_j has to be evaluated at the thermodynamic conditions of zone j . The volume, the mass, the gas constant, and the temperature of zone i are denoted by V_i , m_i , R_i , and T_i . The variable p denotes the in-cylinder

pressure.

The change of internal energy can be written as:

$$dU_i = m_i du_i + \sum_{j \neq i} dm_{ij} u_i \quad (4.3)$$

Since the gas composition changes with temperature and pressure, the internal energy du_i has to be written as:

$$du_i(p, T) = \left(\frac{\partial u_i}{\partial p} \right) dp + \left(\frac{\partial u_i}{\partial T_i} \right) dT \quad (4.4)$$

Using the Maxwell relations [27] the two terms on the right-hand side can be reformulated as:

$$\left(\frac{\partial u_i}{\partial p} \right) = -\frac{T_i^2}{p} \left(\frac{\partial R_i}{\partial T_i} \right) - T_i \left(\frac{\partial R_i}{\partial p} \right) \quad (4.5)$$

$$\left(\frac{\partial u_i}{\partial T_i} \right) = \left(\frac{\partial h_i}{\partial T_i} \right) - R_i - T_i \left(\frac{\partial R_i}{\partial T_i} \right) \quad (4.6)$$

Analogously to the change of the specific internal energy du_i , the change of the gas constant can be written as:

$$dR_i(p, T) = \left(\frac{\partial R_i}{\partial p} \right) dp + \left(\frac{\partial R_i}{\partial T_i} \right) dT \quad (4.7)$$

The caloric properties specific enthalpy h and the gas constant R as well as their derivatives with respect to temperature and pressure $\partial h/\partial T$, $\partial R/\partial p$, $\partial R/\partial T$ are calculated as functions of pressure, temperature, and fuel/air equivalence ratio and are stored in tables for later use in the process simulation (see Appendix C).

The equations for energy and mass conservation are completed with the constraints imposed by the geometry of the cylinder and the

motion of the piston,

$$\sum_i V_i = V \quad (4.8)$$

where V is the total cylinder volume.

The mass flow from the unburned zone to the burned zone dm_{bu} is given by the derivative of the burned mass fraction dx_b and the total mass of the cylinder charge m_{tot} :

$$dm_{bu} = -dm_{ub} = m_{tot} dx_b \quad (4.9)$$

The burned mass fraction x_b is calculated using (3.3). The heat transfer to the cylinder wall is formulated according to the publication by Woschni [63]. It was originally designed to take the averaged cylinder temperature as input. For the context of this work, it is appropriate to apply Woschni's heat transfer correlation to the burned gas zone only, since any other more complex calculations would unnecessarily add unwanted numerical complexity.

$$\begin{aligned} \frac{dQ_{ht}}{dt} &= A h_c (T - T_w) \\ h_c &= C_0 B^{-0.2} (p_f \cdot 10^{-5})^{0.8} T^{-0.53} c_{char}^{0.8} \\ c_{char} &= C_1 c_m + C_2 \frac{V_d T_{ivc}}{V_{ivc} p_{ivc}} (p_f - p_m) \end{aligned} \quad (4.10)$$

The variable A designates the contact area between gas and wall, T is the gas temperature, T_w is the wall temperature, C_0 , C_1 , and C_2 are empirically determined constants, p_f and p_m are the fired and the motored in-cylinder pressure, V_d is the displacement, c_m is the mean piston speed, and T_{ivc} , p_{ivc} , V_{ivc} are the temperature, the pressure and the cylinder volume at inlet valve close, respectively.

The parameters that define the in-cylinder pressure and tempera-

ture are:

1. The initial conditions of the pressure and the temperature of the unburned zone¹. The initial pressure is set to the corresponding value obtained from in-cylinder pressure measurements of a 6-cylinder 3.2-liter SI engine. The initial temperature has to be calibrated, as described below in Sect. 4.1.2.
2. The parameters that define the shape of the burned mass fraction are the combustion start θ_{cs} , the combustion end θ_{ce} , and the form parameter m_v . All three parameters have to be calibrated, as described in Sect. 4.1.2.
3. The parameters that define the gas composition are the residual gas mass fraction x_r and the fuel/air equivalence ratio ϕ . The fuel/air equivalence ratio is set to the corresponding value obtained from measurements at a 6-cylinder 3.2-liter SI engine. The residual gas mass fraction has to be calibrated, as described in Sect. 4.1.2.
4. The parameters that define the heat transfer to the cylinder wall are the constants C_0 , C_1 , and C_2 ² in (4.10). The constants C_0 to C_2 are set to standard values taken from the literature: $C_0 = 130$, $C_1 = 2.28$, and $C_2 = 3.24 \cdot 10^{-3}$ [34].

¹The initial temperature of the burned gas zone is calculated based on the temperature of the unburned gas zone and the in-cylinder pressure at combustion start. The pressure of the burned gas zone is equal to the pressure of the unburned gas zone.

²The temperature and pressure at intake valve close T_{ivc} and p_{ivc} in (4.10) are defined by the initial temperature and pressure of the unburned gas zone. The volume at intake valve close V_{ivc} is defined by the position of the piston at the instant when the inlet valve closes.

4.1.2 Calibration of the Model Parameters

The parameters that have to be calibrated are the residual gas mass fraction x_r , the initial temperature T_{IC} , the flame development angle θ_d , the rapid burning angle θ_b , and the form parameter m_v . The outputs of the model are the in-cylinder pressure $p(\theta)$ and the engine-out NO emission [NO], as shown in Fig. 4.2. For the purpose of the calibration, the 2-zone process simulation is combined with the NO formation model discussed later in Chap. 5. Since the in-cylinder temperature cannot be measured directly, but the amount of the engine-out NO emissions reflects information about the burned gas temperature, the measured and the calculated engine-out NO emissions are compared in order to calibrate the burned gas temperature. For this purpose, the NO formation model introduced later in Sect. 5 is used to calculate the NO emissions based on the burned gas temperature.

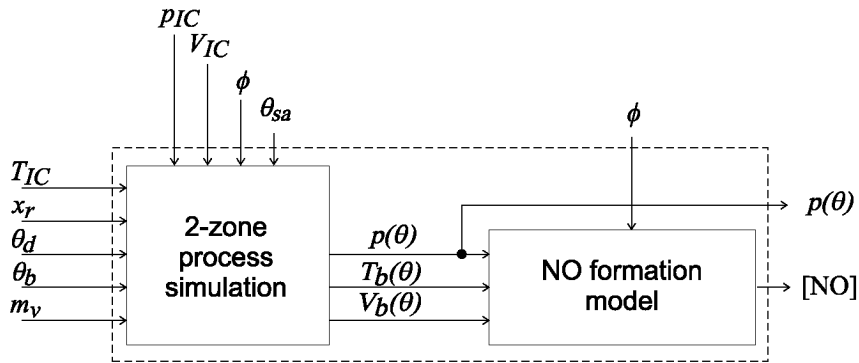


Figure 4.2: 2-zone process simulation combined with NO formation model showing model inputs and outputs

Using standard optimization techniques, the input parameters T_{IC} , x_r , θ_d , θ_b , and m_v are found, such that the following cost function J

is minimized:

$$\begin{aligned}
 J = & k_{NO}(\langle \text{NO} \rangle_{meas} - \langle \text{NO} \rangle_{sim})^2 \\
 & + \sum_{\theta_i=-100}^{+100} (p_{meas}(\theta_i) - p_{sim}(\theta_i))^2
 \end{aligned} \tag{4.11}$$

The NO concentration $\langle \text{NO} \rangle$ is on the order of 10^3 ppm, the in-cylinder pressure p is on the order of 10^5 Pa. The weight $k_{NO} = 10^6$ with units $\text{Pa}^2\text{ppm}^{-2}$ is introduced in order to balance the contributions of the NO estimation error and the pressure estimation error in (4.11).

Prior to the minimization of (4.11), initial values for the combustion start and end can be found using the heat release analysis described in Appendix B.

4.1.3 Results of the 0-Dimensional 2-Zone Process Simulation

Figures 4.3 and 4.4 show simulation results at two different operating points. As a result of the cost function (4.11), pressure profiles and engine-out NO emissions match measured data. The profiles of the burned gas temperature cannot be compared to measured data, since the in-cylinder temperature is not readily accessible.

4.1.4 Comments on the Resulting Temperature of the Burned Gas Zone

A realistic concept of the combustion process can be described as follows: Soon after the spark discharge, the flame front starts travelling through the combustion chamber. As the flame front progresses as a spherically shaped thin layer into the unburned gas, it leaves burned gas at a higher temperature behind. For a finer spatial resolution, the

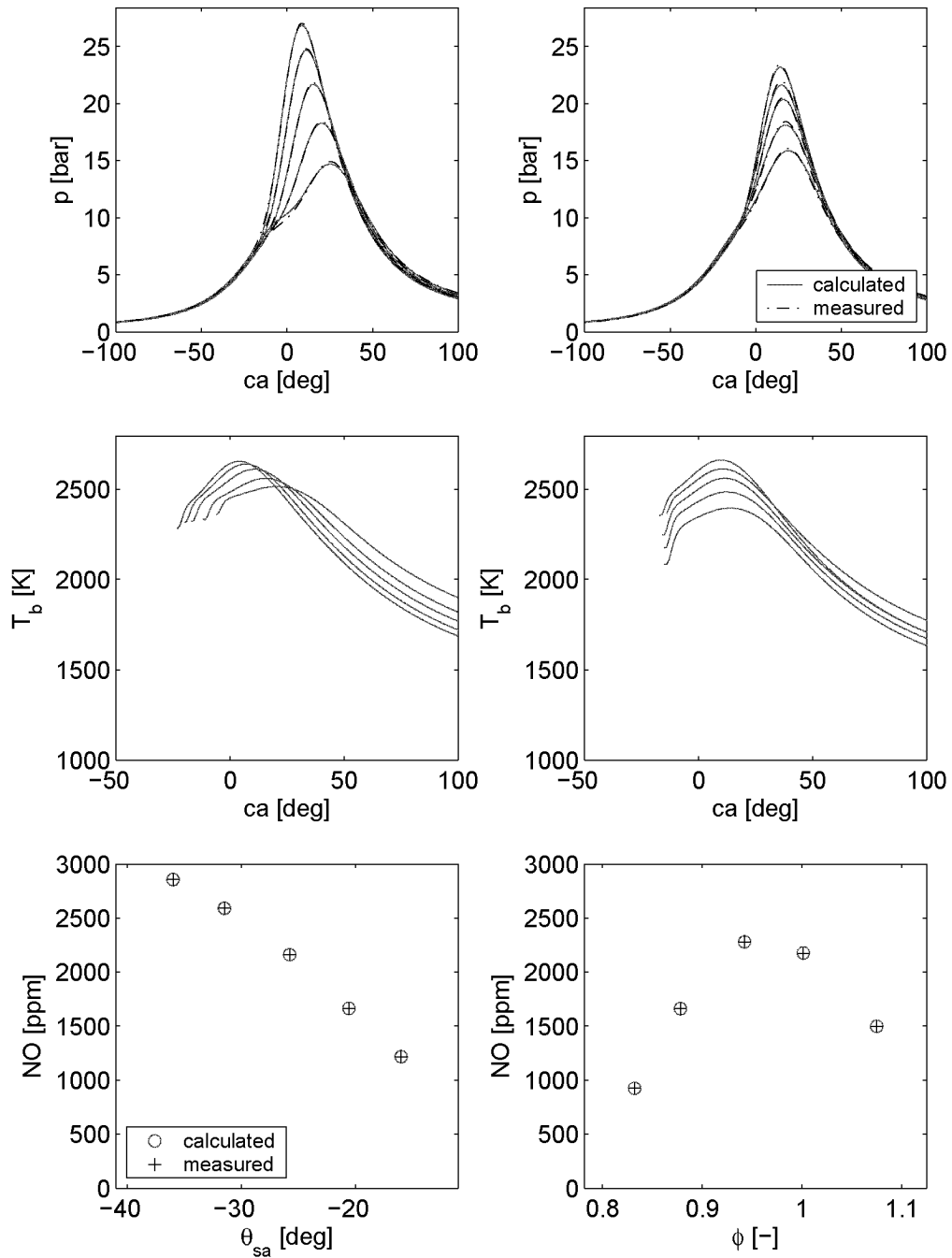


Figure 4.3: Reference data at $n = 2000$ rpm and $p_{im} = 0.5$ bar, generated with the 0-dimensional 2-zone process simulation. The graphs on the left show the results from the variations of the spark advance, while the graphs on the right show the results from the variation of the fuel/air equivalence ratio

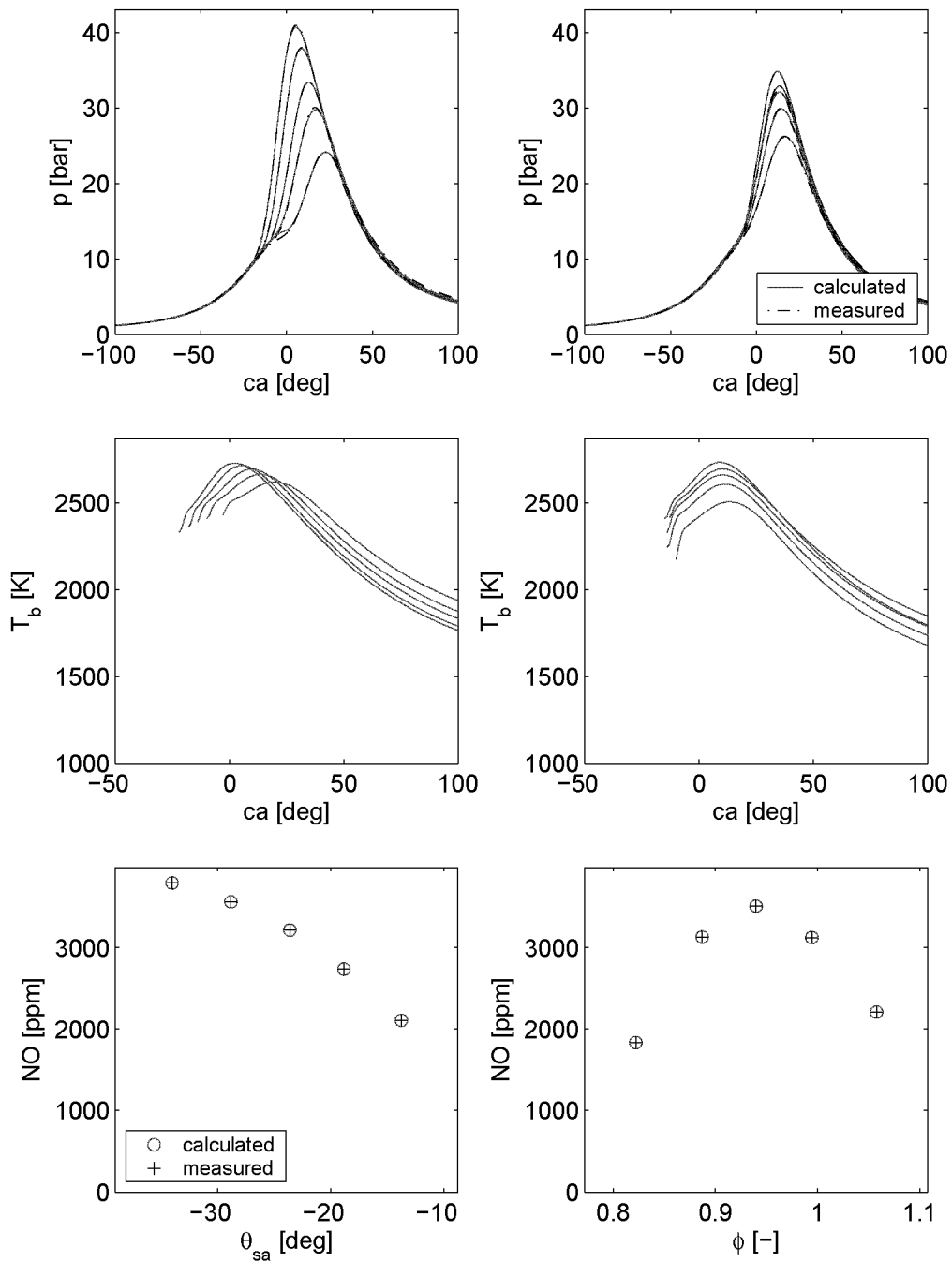


Figure 4.4: Reference data at $n = 3000$ rpm and $p_{im} = 0.65$ bar, generated with the 0-dimensional 2-zone process simulation. The graphs on the left show the results from the variation of the spark advance, while the graphs on the right show the results from the variation of the fuel/air equivalence ratio

burned gas is often divided into different zones, each of which with its own time history of temperatures. While the combustion is ongoing, the burned gas is compressed or expanded according to the motion of the piston. The different burned gas zones exchange heat and mass among themselves driven by the motion of the in-cylinder fluid. A sketch of such a combustion process is given in the right-hand graph of Fig. 4.1.

In contrast, the 0-dimensional 2-Zone process simulation used here is a simplification of what happens during combustion. Major simplifications are (A) to lump all burned gas into one single zone, (B) to neglect fluid motion and mixing among neighboring zones, and (C) to neglect all geometric information except the volume of the burned gas.

Two consequences thus have to be taken into account: (A) The temperature T_b of the burned gas zone in the process simulation model is a mass averaged temperature. (B) As the NO composition and decomposition rates are exponentially dependent on the temperature, the 2-zone process simulation cannot accurately predict the engine-out NO emissions.

Combining the 2-zone process simulation and the NO formation with the cost function J in (4.11) for calibration, the temperature of the burned gas zone is identified such that accurate engine-out NO emissions result. This comes at the cost of a slightly mistuned calibration of the parameters x_r and T_{IC} . Since only the temperature of the burned gas is of interest, this trade-off is of minor importance.

4.2 Control-Oriented Model

The 0-dimensional 2-zone process simulation model presented in the previous section is too complex for control purposes. This section thus derives a model for the burned gas zone that can be evaluated at little

computational cost.

The model is derived from physical first principles and is simplified to the extent that it is numerically efficient while the physically motivated parameters are maintained.

The strategy is to identify a set of model parameters for each reference operating point at nominal operating conditions. Deviations of the burned gas temperature profile due to deviations of the operating conditions from their nominal setting are then calculated based on the model.

4.2.1 Model Equations

For the burned gas zone an energy balance is formulated

$$dU = dW + dQ_f + dQ_{ht}, \quad (4.12)$$

where dU is the change of internal energy, dW is the work due to the displacement of the piston, dQ_f is the energy released from the fuel, and dQ_{ht} is the heat transfer to the cylinder wall.

For the control-oriented model, the combustion is discretized into equal crank angle intervals k . Each interval is divided into a compression/expansion stage and a combustion stage. The heat transfer is neglected for the moment, but will be reconsidered further below.

1. From time step k to time step $k + 1$ the mass in the burned gas zone is compressed or expanded according to the pressure change from p_k to p_{k+1} . This stage may be associated with the work term dW above.
2. After the compression or expansion stage, a new portion of fresh mixture is burned. During the combustion, the temperature of the portion of fresh mixture rises by the adiabatic flame temperature ΔT_{ad} . When the new portion is burned, it enters the

burned gas zone. The temperature difference between the new portion and the burned gas zone is immediately levelled out through heat transfer among the burned gas zone and the new portion. This stage can be associated with the term for the heat release dQ_f above.

Mathematically, the two stages are formulated as follows:

$$c_v m_{k+1} T_{k+1} = \underbrace{c_v m_k T_k \left(\frac{p_k}{p_{k+1}} \right)^{\frac{1-\kappa}{\kappa}}}_{1. \text{ stage}} + \underbrace{c_v (m_{k+1} - m_k) (T_u + \Delta T_{ad})}_{2. \text{ stage}} \quad (4.13)$$

Dividing (4.13) by $c_v m_{k+1}$, the temperature at time step $k+1$ can be calculated as:

$$T_{k+1} = \frac{m_k}{m_{k+1}} T_k \left(\frac{p_k}{p_{k+1}} \right)^{\frac{1-\kappa}{\kappa}} + \frac{m_{k+1} - m_k}{m_{k+1}} (T_u + \Delta T_{ad}) \quad (4.14)$$

The adiabatic flame temperature rise ΔT_{ad} is calculated as

$$\Delta T_{ad} = k^0 \Delta T_{ad,th} (1 - x_r) + c_{T_{ad}}^0 (\theta_{80} - \theta_{80}^0), \quad (4.15)$$

where $\Delta T_{ad,th}$ is the adiabatic flame temperature rise calculated on the basis of the temperature of the unburned gas, the pressure, and the fuel/air equivalence ratio. The residual gas mass fraction is denoted by x_r . The correcting gain k^0 is used to allow for an exact calibration of the burned gas temperature for the engine at hand. The second term on the right-hand side accounts for the changing heat transfer to the cylinder wall with changing combustion phasing. The parameter $c_{T_{ad}}^0$ has to be identified for each reference operating point. The value θ_{80} is the crank angle position when 80% of the combustion time

has elapsed. The rise of the adiabatic flame temperature $\Delta T_{ad,th}$ is the result of an enthalpy balance between a unit mass of burned and unburned gas,

$$h_u(p, T_u, \phi) = h_b(p, T_u + \Delta T_{ad,th}, \phi),$$

which has to be solved by iteration. The values for $\Delta T_{ad,th}$ are pre-computed for combinations of p , T , and ϕ and stored in a map. The calculation of the enthalpy values h_u and h_b are presented in Appendix C.

The mass m_k of the burned gas zone at time step k is calculated based on the burned mass fraction $x_{b,k}$ at time step k and the total mass m_{tot} in the combustion chamber:

$$m_k = x_{b,k} m_{tot} \quad (4.16)$$

With the insertion of (4.16) in (4.14), the total mass m_{tot} cancels out, which eliminates a major source of errors for the burned gas temperature estimation.

$$T_{k+1} = \frac{x_{b,k}}{x_{b,k+1}} T_k \left(\frac{p_k}{p_{k+1}} \right)^{\frac{1-\kappa}{\kappa}} + \frac{x_{b,k+1} - x_{b,k}}{x_{b,k+1}} (T_u + \Delta T_{ad}) \quad (4.17)$$

The temperature of the unburned gas zone is calculated assuming a polytropic state change:

$$T_u = T_1 \left(\frac{p_1}{p(\theta)} \right)^{\frac{1-\kappa}{\kappa}} \quad (4.18)$$

The temperature T_1 at 80 degrees before TDC is determined from

the inlet manifold pressure and the residual gas mass:

$$T_1 = \frac{m_r T_r + m_{fr} T_{fr}}{m_r + m_{fr}} \left(\frac{p_{im}}{p_1} \right)^{\frac{1-\kappa}{\kappa}} \quad (4.19)$$

$$m_r = \frac{p_{em} V_c}{R_r T_r} \quad (4.20)$$

$$m_{fr} = \frac{p_{im}}{R_{fr} T_{ip}} \quad (4.21)$$

The temperature T_r of the residual gas is set to 800 K for all operating points and all operating conditions. The temperature of the fresh charge T_{fr} entering the cylinder is set to the temperature at the inlet manifold T_{im} . The mass of the residual gas is denoted by m_r and the mass of the fresh charge by m_{fr} . Using the same indices, the gas constant of the residual gas and the fresh gas are denoted by R_r and R_{fr} , respectively. The pressures in the inlet manifold and the outlet manifold are p_{im} and p_{em} . Finally, the variable V_c denotes the compression volume.

The heat transfer to the cylinder wall neglected thus far has to be reconsidered now. The heat transfer correlation introduced by Woschni [63] is linearized for the purpose of the simplified model. The expression (4.10) can be approximated by a non-linear term $\alpha(p)$, which may be precalculated based on the in-cylinder pressure, multiplied by an affine function of the gas temperature T . Figures 4.5 and 4.6 show the accuracy of this approximation, while Table 4.1 lists the values identified for the coefficients.

$$\begin{aligned} \frac{dQ_{ht}}{dt} &= \alpha(p) T^{-0.53} (T - T_w) \\ &\approx \alpha(p) (a_1 T_w T + a_0 T + b_1 T_w + b_0) \end{aligned} \quad (4.22)$$

The cooling effect of the heat transfer to the cylinder wall can now

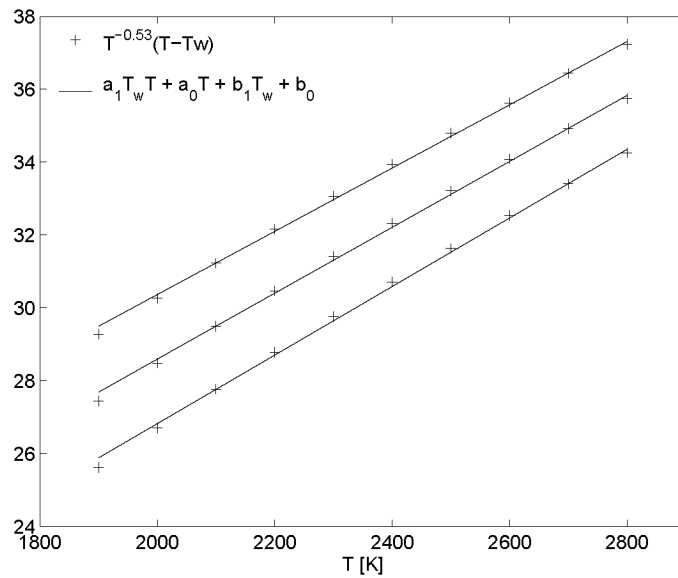


Figure 4.5: Linearization of Woschni's heat transfer correlation. The results are shown for the wall temperatures $T_w = 400$ K, $T_w = 500$ K, and $T_w = 600$ K

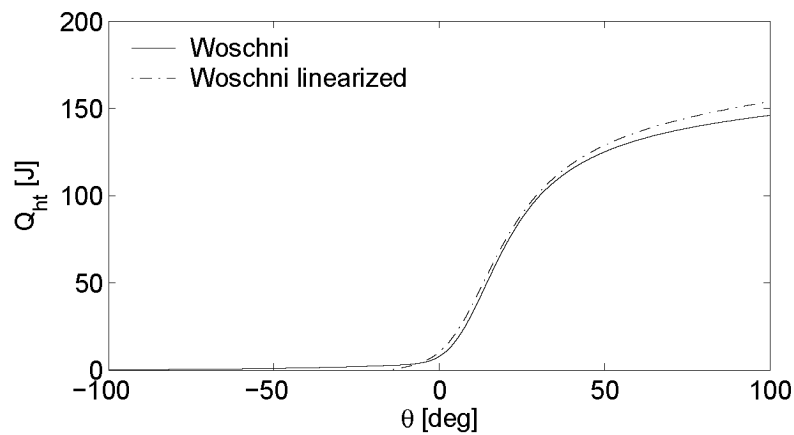


Figure 4.6: Comparison of the heat transferred to the cylinder wall calculated based on the Woschni's original heat transfer correlation and based on the linearized heat transfer correlation during a typical combustion

Table 4.1: Identified coefficients for the approximation of the Woschni's heat transfer correlation

a_0	a_1	b_0	b_1
$7.60 \cdot 10^{-3}$	$3.63 \cdot 10^{-6}$	20.47	$-2.5 \cdot 10^{-2}$

be integrated into Eq. (4.17):

$$T_{k+1} = \frac{x_{b,k}}{x_{b,k+1}} T_k \left(\frac{p_k}{p_{k+1}} \right)^{\frac{1-\kappa}{\kappa}} + \frac{x_{b,k+1} - x_{b,k}}{x_{b,k+1}} (T_u + \Delta T_{ad}) - \frac{\alpha(p)}{c_v m_{k+1}} (a_1 T_w T + a_0 T + b_1 T_w + b_0) \frac{\Delta \theta}{\omega} \quad (4.23)$$

Equation (4.23) is applied from combustion start, θ_{cs} , to combustion end, θ_{ce} . From combustion end to outlet valve open, the in-cylinder temperature is calculated following the ideal gas law:

$$T_b(\theta) = T_b(\theta_{ce}) \frac{p(\theta)V(\theta)}{p(\theta_{ce})T_b(\theta_{ce})} \quad (4.24)$$

Based on the temperatures of the burned and the unburned gas zones the volume of the burned gas zone can be calculated as

$$V_b = V \frac{x_b R_b T_b}{(1 - x_b) R_u T_u + x_b R_b T_b}, \quad (4.25)$$

where R_b , R_u are the gas constants of the burned and the unburned gas, x_b is the burned mass fraction, T_b and T_u are the temperatures of the burned and the unburned gas, and V is the total volume of the combustion chamber, respectively.

4.2.2 Calibration

For the calibration of the simplified model of the burned gas temperature, the measured data from data sets \mathbf{A}^+ (which comprises data set \mathbf{A}) and \mathbf{B}^- (see Sect. 2.4) are used.

1. The coefficients of the polynomials f_{sa} , f_ϕ , g_{sa} , and g_ϕ , which describe the flame development and the rapid burning angles (see Eqs. (3.6) and (3.7)). The polynomials f_ϕ and g_ϕ are second-order polynomials, whereas f_{sa} and g_{sa} are affine func-

tions: All together, ten coefficients have to be calibrated. The data obtained from the variations of θ_{sa} and ϕ at $n = 2000$ rpm and $p_{im} = 0.5$ bar, data set \mathbf{B}^- , are used for calibration.

2. The correction k^0 (see Eq. (4.15)) of the adiabatic flame temperature ΔT_{ad} has to be calibrated for each reference operating point. The data obtained from the measurements at the reference operating points, data set \mathbf{A} , is used for the calibration.
3. The parameters $c_{T_{ad}}^0$ have to be calibrated for each reference operating point. The data obtained from the measurements at nominal operating conditions and one later spark advance timing at the reference operating points are used for the calibration (data set \mathbf{A}^+).

The constants $C_0 = 130$, $C_1 = 2.28$, and $C_2 = 3.24 \cdot 10^{-3}$ are set to standard values taken from the literature [34].

4.2.3 Results

The Figs. 4.7 to 4.15 and Tables 4.2 and 4.3 on the following pages list the measured data obtained from the 6-cylinder 3.2-liter engine, the results obtained with the 2-zone process simulation, and the results obtained with the control-oriented model.

The graphs in Figs. 4.7 to 4.15 are organized as follows: The graphs in the first row show the combustion start and the combustion end calculated based on the control-oriented model (o) and the results based on [19] (+), as well as the results based on the 2-zone process simulation (x). The graphs in the second row show the in-cylinder pressures calculated using the control-oriented model (solid lines) and the measured in-cylinder pressures (dotted lines). The third row of graphs shows the burned gas temperatures calculated using the control-oriented model (solid lines) and the temperatures calculated

Table 4.2: Correcting gain of the adiabatic flame temperature: k^0 [-]

	1000 rpm	2000 rpm	3000 rpm
0.65 bar	0.995	1.015	1.023
0.50 bar	1.049	1.027	1.030
0.30 bar	1.098	1.080	1.051

Table 4.3: Correcting gain for heat transfer compensation: $c_{T_{ad}}^0$ [K rad⁻¹]

	1000 rpm	2000 rpm	3000 rpm
0.65 bar	-0.146	-0.083	-0.059
0.50 bar	-0.108	-0.046	-0.060
0.30 bar	-0.031	-0.044	-0.038

using the 2-zone process simulation (dotted lines). The graphs in the last row show the engine-out NO emissions calculated based on the control-oriented model (o) and the measured engine-out NO emissions (+).

The values listed in the Tables 4.2 and 4.3 for k^0 and $c_{T_{ad}}^0$ were identified, such that calculated and measured engine-out NO emissions match as closely as possible in a least-squared-error sense.

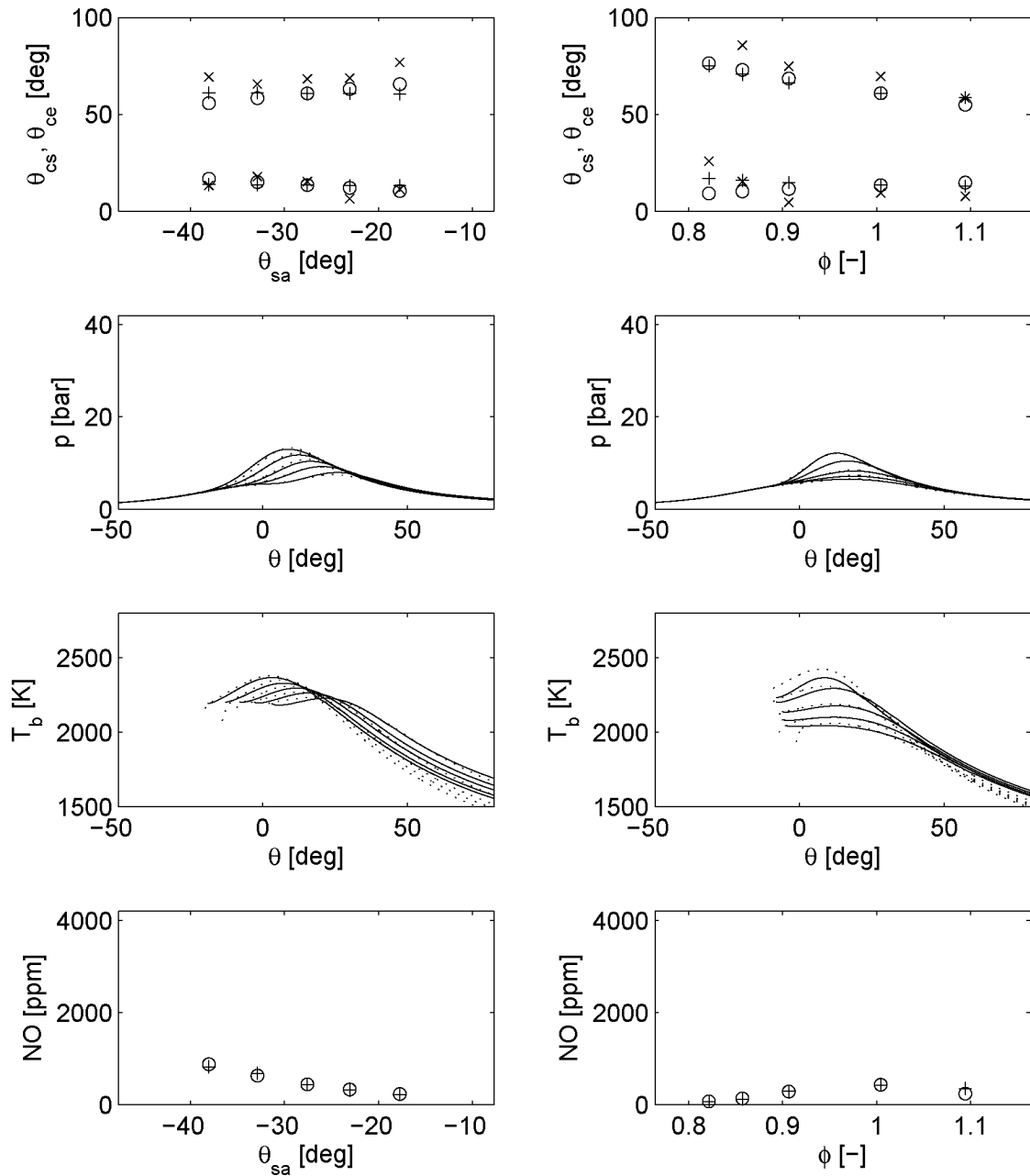


Figure 4.7: Validation results at $n = 1000$ rpm and $p_{im} = 0.30$ bar. Left column: spark advance variations; right column: fuel/air equivalence ratio variations. See also text on page 92

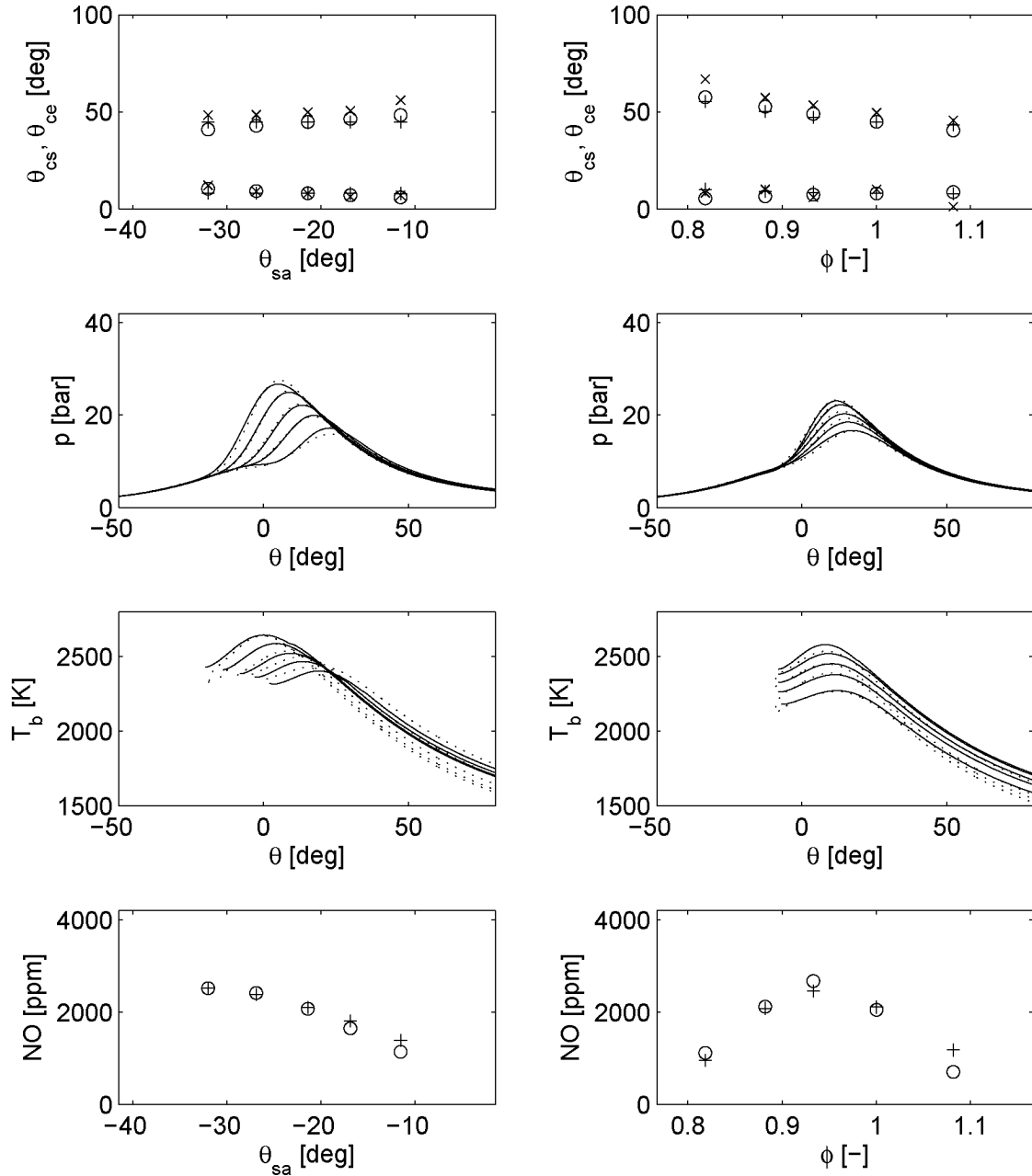


Figure 4.8: Validation results at $n = 1000$ rpm and $p_{im} = 0.50$ bar. Left column: spark advance variations; right column: fuel/air equivalence ratio variations. See also text on page 92

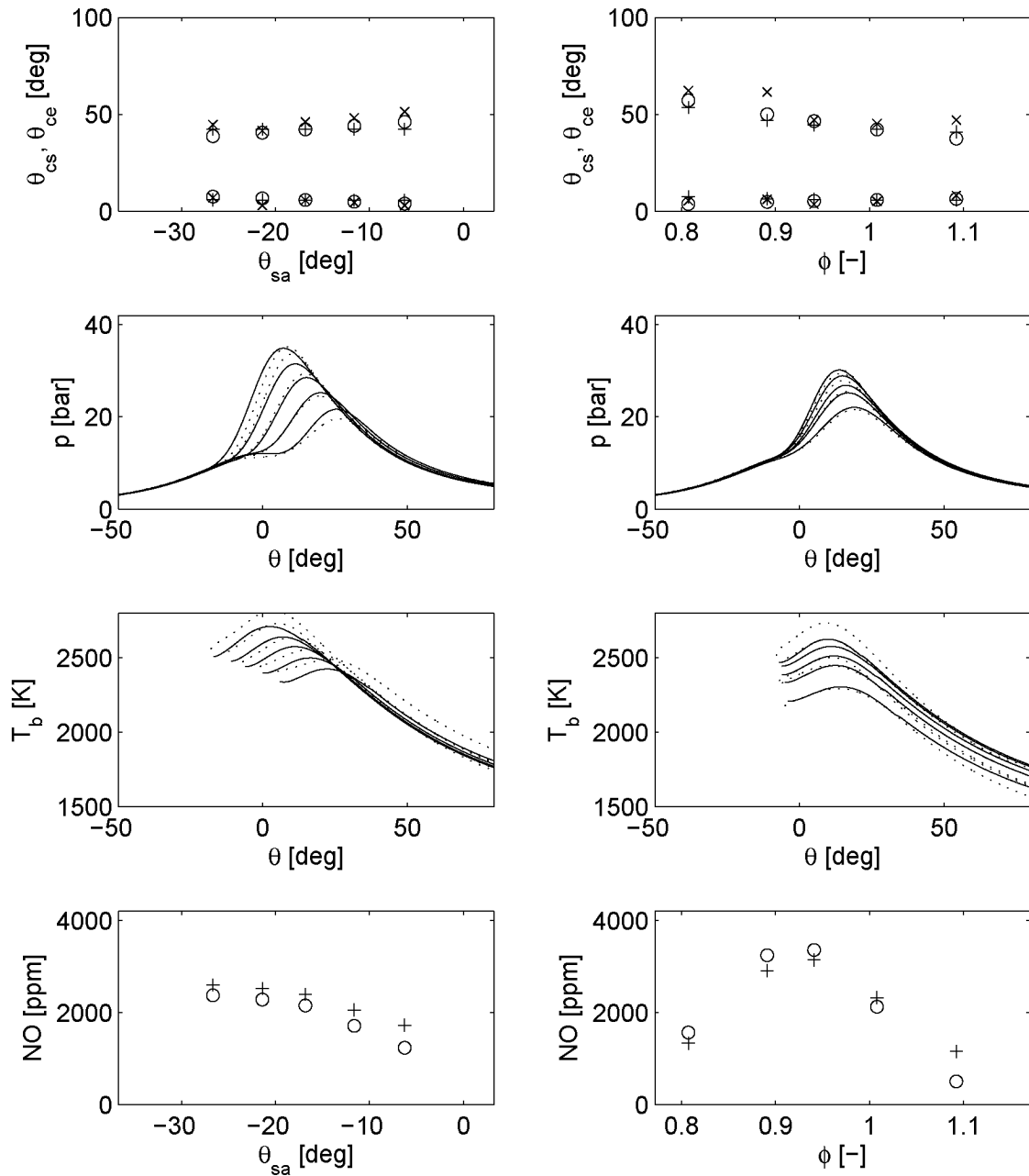


Figure 4.9: Validation results at $n = 1000$ rpm and $p_{im} = 0.65$ bar. Left column: spark advance variations; right column: fuel/air equivalence ratio variations. See also text on page 92

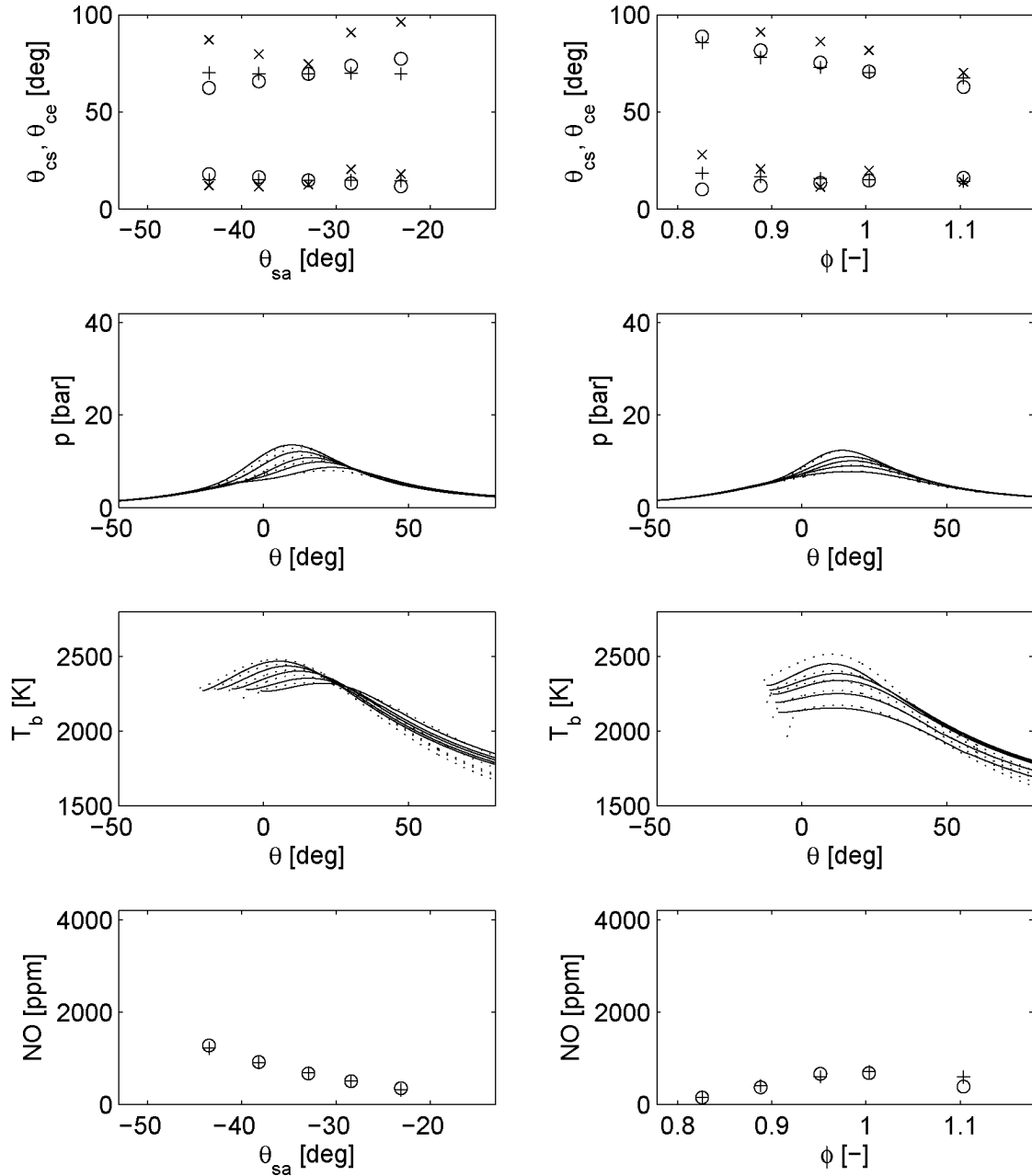


Figure 4.10: Validation results at $n = 2000$ rpm and $p_{im} = 0.30$ bar. Left column: spark advance variations; right column: fuel/air equivalence ratio variations. See also text on page 92

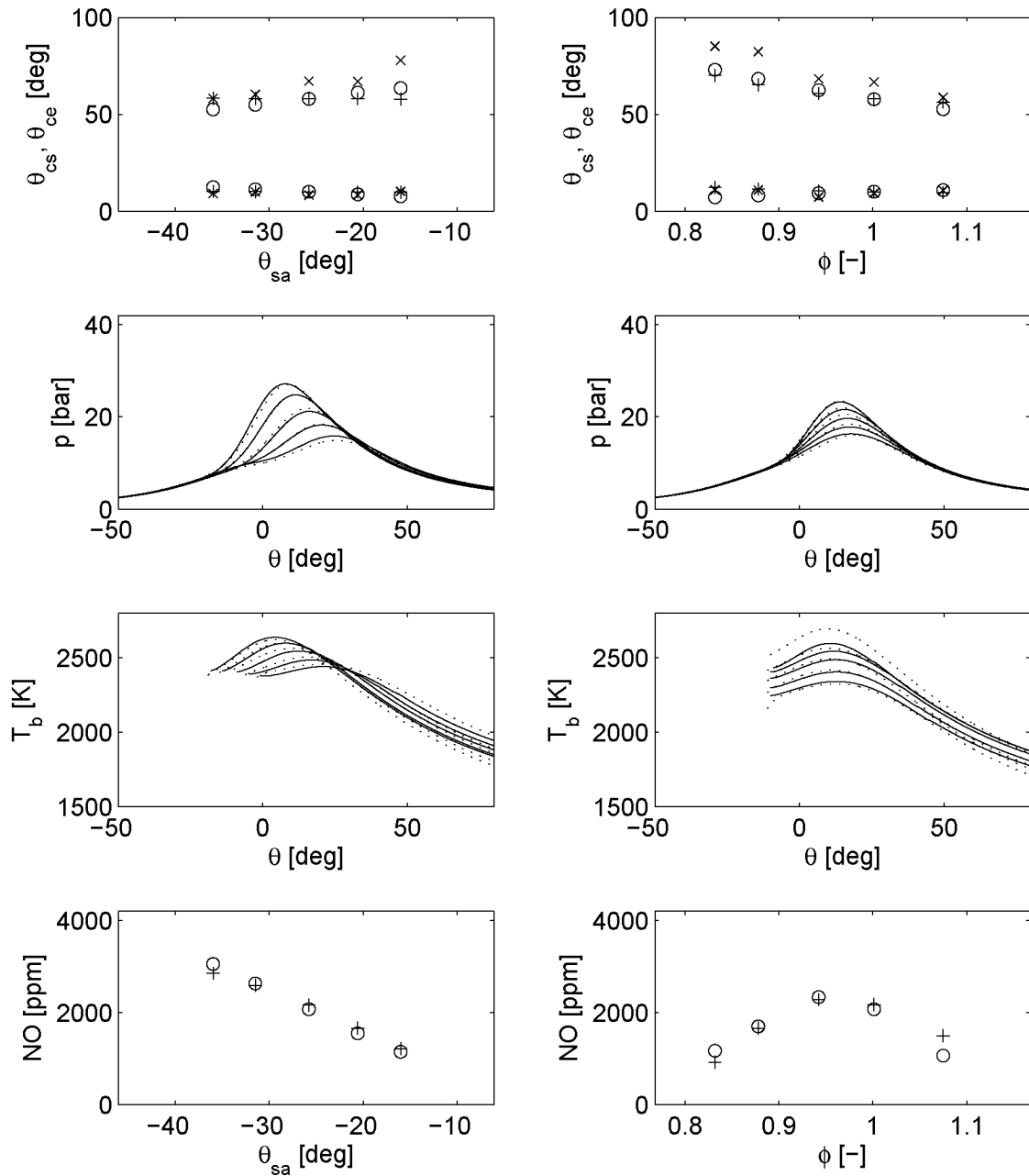


Figure 4.11: Validation results at $n = 2000$ rpm and $p_{im} = 0.50$ bar. Left column: spark advance variations; right column: fuel/air equivalence ratio variations. See also text on page 92

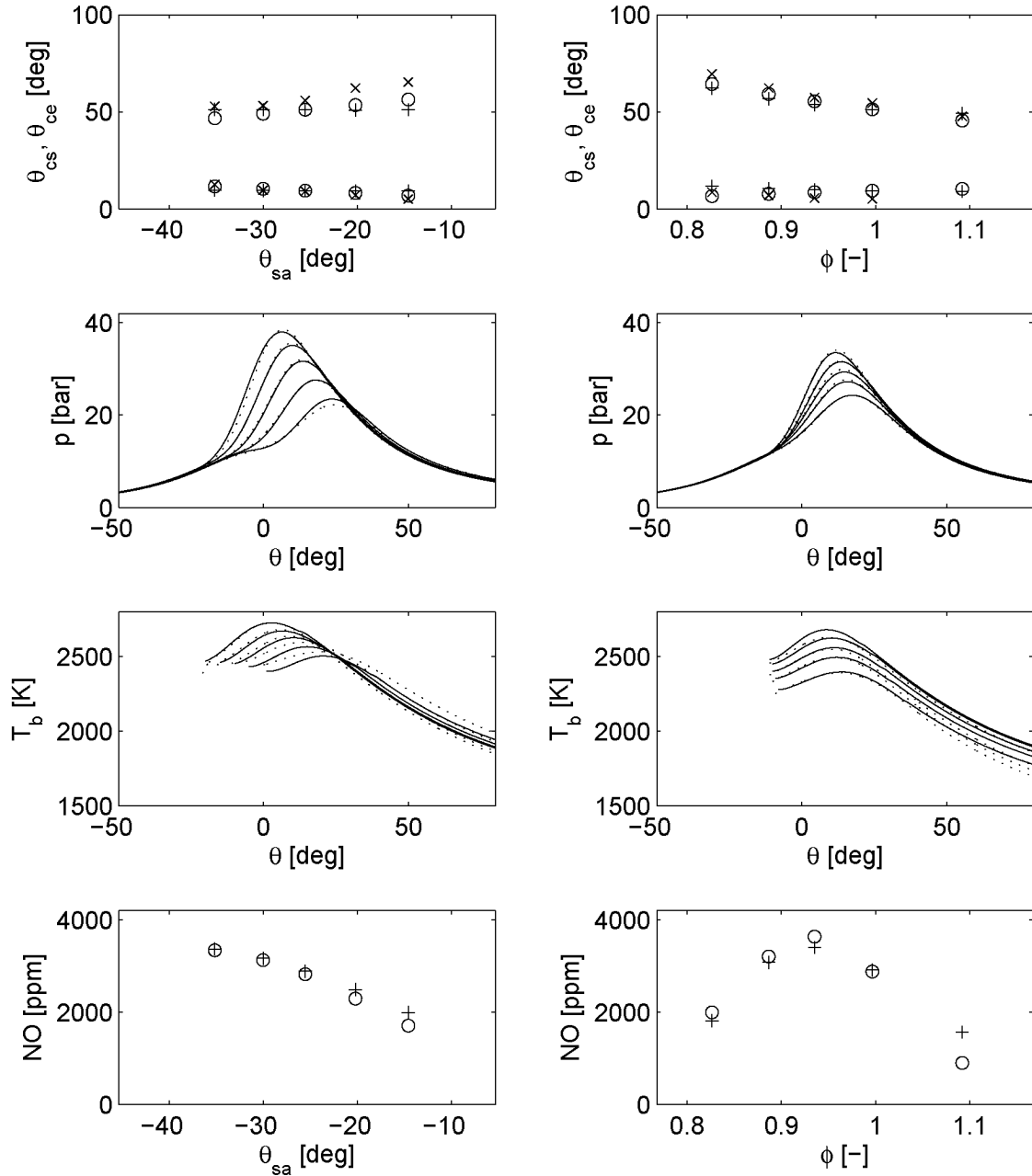


Figure 4.12: Validation results at $n = 1000$ rpm and $p_{im} = 0.65$ bar. Left column: spark advance variations; right column: fuel/air equivalence ratio variations. See also text on page 92

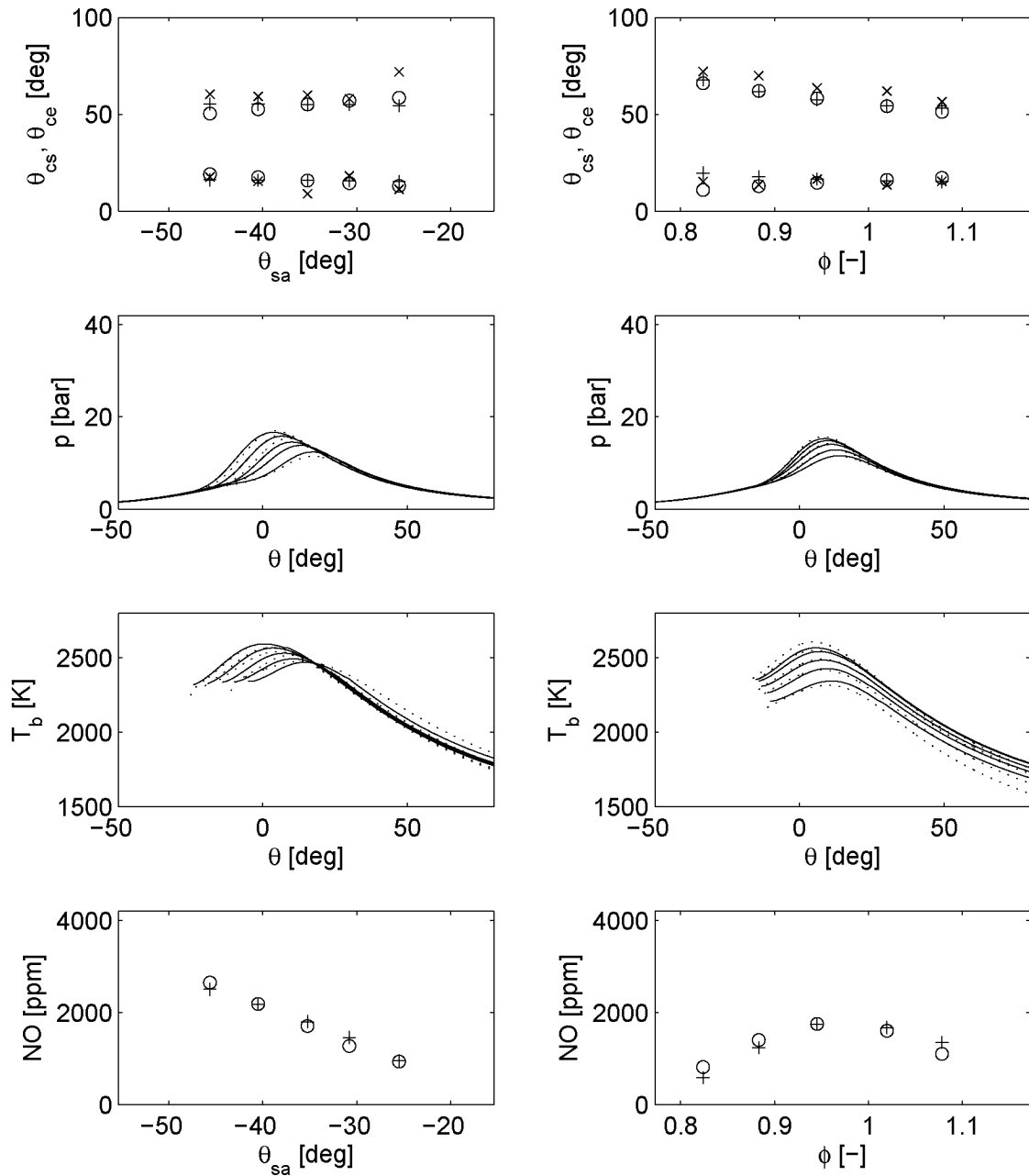


Figure 4.13: Validation results at $n = 3000$ rpm and $p_{im} = 0.30$ bar. Left column: spark advance variations; right column: fuel/air equivalence ratio variations. See also text on page 92

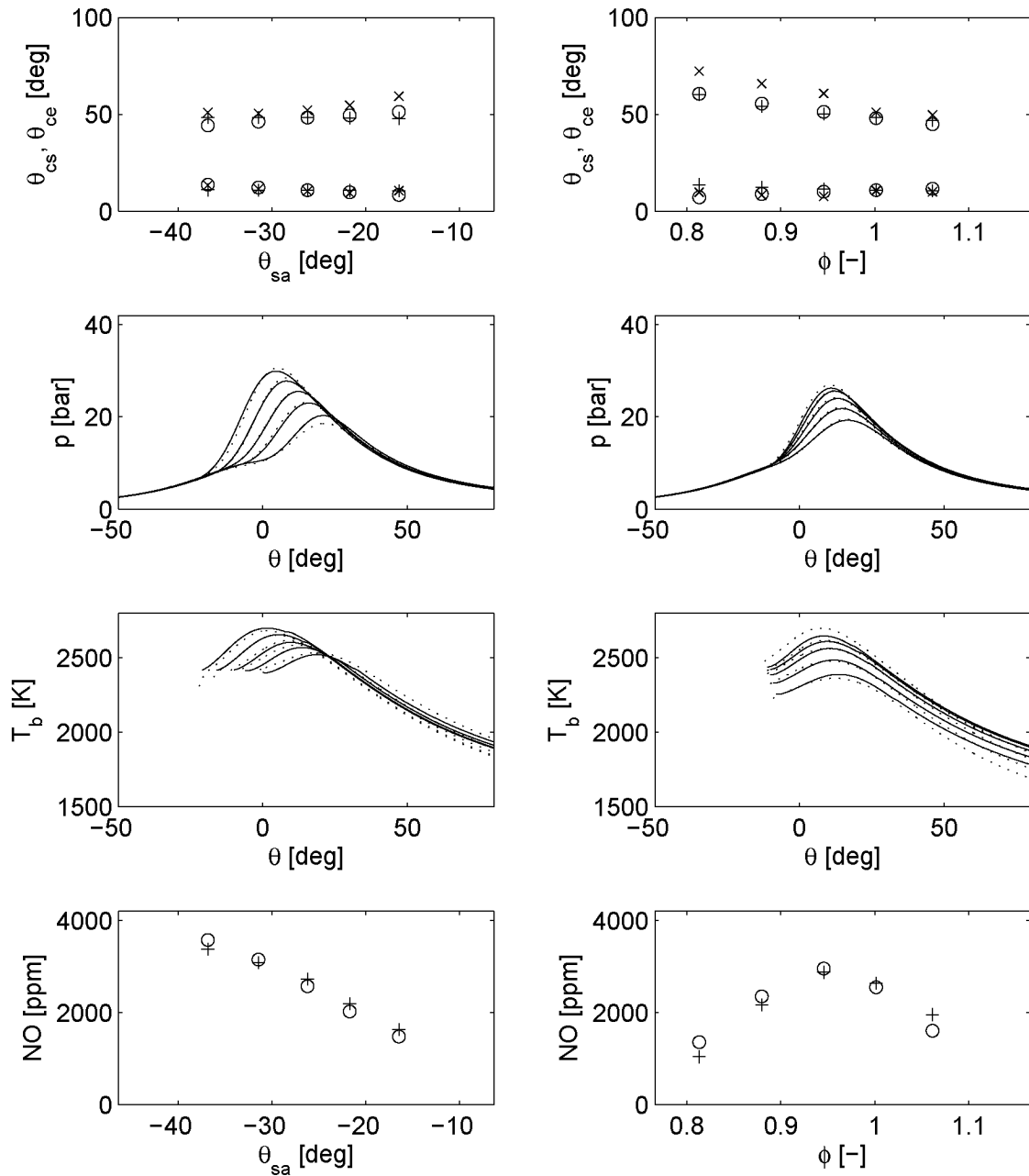


Figure 4.14: Validation results at $n = 3000$ rpm and $p_{im} = 0.50$ bar. Left column: spark advance variations; right column: fuel/air equivalence ratio variations. See also text on page 92

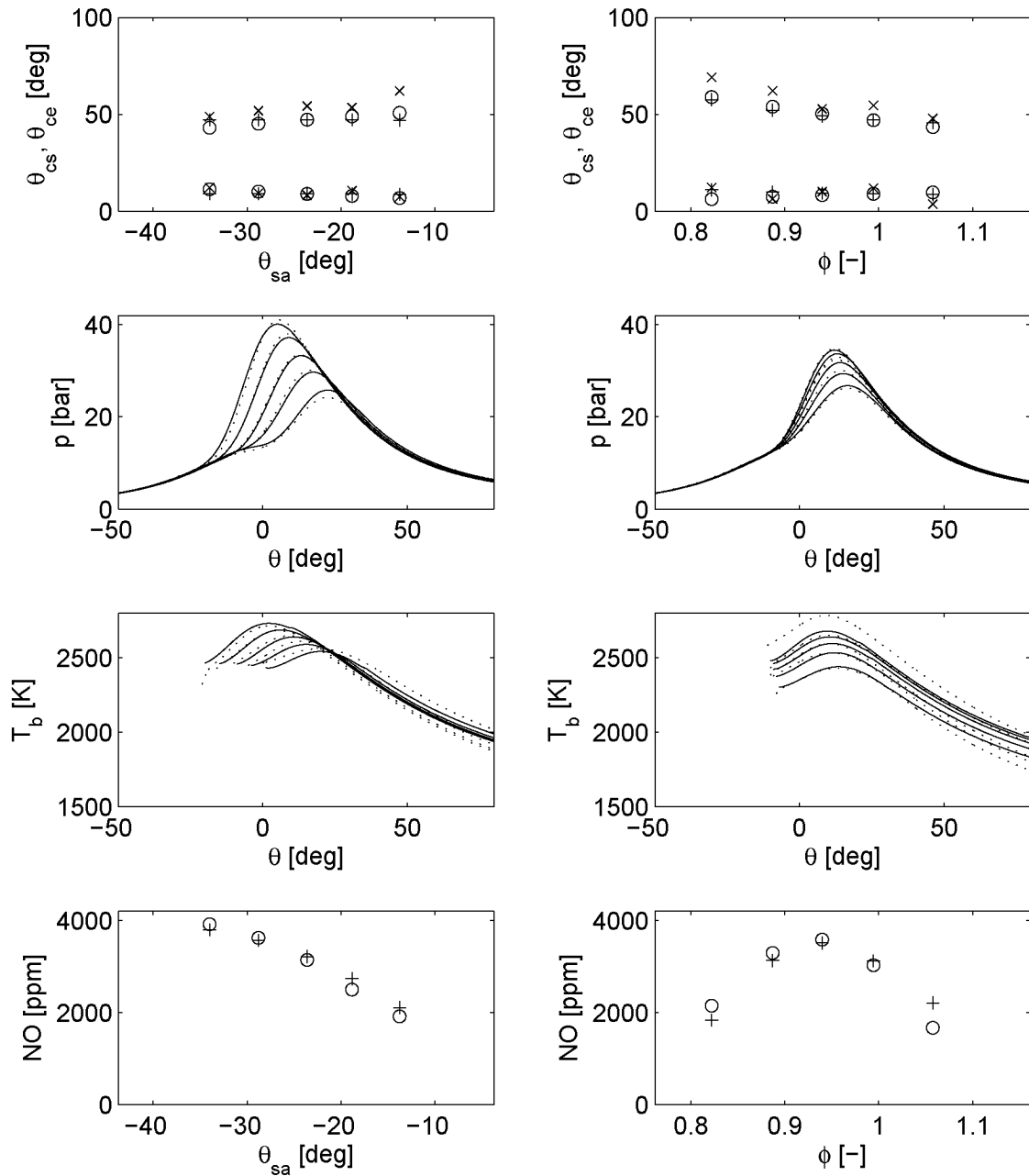


Figure 4.15: Validation results at $n = 3000$ rpm and $p_{im} = 0.65$ bar. Left column: spark advance variations; right column: fuel/air equivalence ratio variations. See also text on page 92

Chapter 5

NO Formation

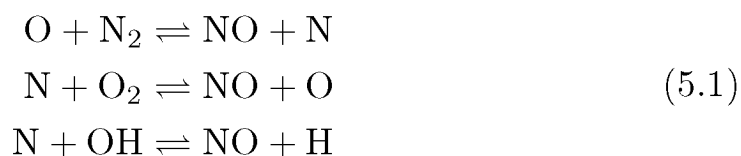
This chapter derives a simplified differential equation for the NO formation from the set of differential equations of the chemical reactions involved. Although three different paths for the NO formation have been found to be contributing to the engine-out NO emissions [13], [12], here only the thermal formation of NO is considered. For a homogeneous SI engine and for the fuel/air equivalence ratios considered here, the dominating fraction of the engine-out NO emissions originates from the thermal NO formation path [34]. Neglecting the other paths is far less critical than inaccuracies in the burned gas temperature estimation [62].

The chapter consists of three sections. The first section formulates the chemical equations. The second section deals with the assumption of the chemical equilibrium and the third section derives the control-oriented differential equation for the NO concentration.

The concentration of NO molecules in the combustion gases is usually measured in ppm or in kmol m^{-3} . Here, angles $\langle \rangle$ denote concentrations in ppm and rectangular brackets $[]$ denote concentrations in kmol m^{-3} .

5.1 Extended Zeldovich Mechanism

Since Zeldovich [65] published the equations to the chemical reactions that lead to the formation of NO during the combustion of hydrogen, a number of other pathways of NO formation in flames or post-flame gases have been postulated (see, e.g., [13]). Up to date, the two equations found by Zeldovich plus a third chemical equation describe the most relevant NO formation mechanism, known as Extended Zeldovich Mechanism:



The extended Zeldovich Mechanism accounts for more than 90% of the NO formation for the operating conditions found in an SI combustion engine [34], [12]. For control-oriented purposes, it is therefore reasonable to neglect the other pathways of the formation of NO, as they add additional complexity to the model without adding any significant information. Moreover, the NO formation shows an extreme sensitivity towards the burned gas temperature; small uncertainties in the temperature estimation cause large NO estimation errors compared to the errors introduced by neglecting certain pathways of the formation of NO.

5.2 Equilibrium Assumption

The time scale of the formation of NO in internal combustion engines heavily depends on the temperature of the burned gas, the availability of oxygen, and the pressure. It is often similar to the time scale of the combustion itself. The NO formation therefore has to be formulated as a differential equation and integrated along with the temperature and pressure profiles of the burned gas during the combustion and

expansion strokes.

From the chemical equations of the Extended Zeldovich Mechanism, the formation rate for $[\text{NO}]$ and $[\text{N}]$ can be derived:

$$\begin{aligned} \frac{d[\text{NO}]}{dt} = & k_{1+}[\text{O}][\text{N}_2] - k_{1-}[\text{NO}][\text{N}] + k_{2+}[\text{N}][\text{O}_2] \\ & - k_{2-}[\text{NO}][\text{O}] + k_{3+}[\text{N}][\text{OH}] - k_{3-}[\text{NO}][\text{H}] \end{aligned} \quad (5.2)$$

$$\begin{aligned} \frac{d[\text{N}]}{dt} = & k_{1+}[\text{O}][\text{N}_2] - k_{1-}[\text{NO}][\text{N}] - k_{2+}[\text{N}][\text{O}_2] \\ & + k_{2-}[\text{NO}][\text{O}] - k_{3+}[\text{N}][\text{OH}] + k_{3-}[\text{NO}][\text{H}] \end{aligned} \quad (5.3)$$

The reaction constants have the form

$$k_i = AT^B e^{\frac{-E}{R_0 T}}. \quad (5.4)$$

The tables with values for the constants A , B , and E are shown in [32], for instance. The universal gas constant is denoted by R_0 and the temperature by T .

While the time scales of the formation of N and NO are comparable to the duration of the combustion, the changes in the concentrations of the other species involved ($[\text{N}_2]$, $[\text{O}_2]$, $[\text{O}]$, $[\text{H}]$, and $[\text{OH}]$) are fast compared to the NO formation. For these species it is assumed that they are at equilibrium concentration, which is denoted by $[\]_e$. The differential equations for concentrations of the NO and N thus read as follows:

$$\begin{aligned} \frac{d[\text{NO}]}{dt} = & k_{1+}[\text{O}]_e[\text{N}_2]_e + k_{2+}[\text{N}]_e[\text{O}_2]_e + k_{3+}[\text{N}]_e[\text{OH}]_e \\ & - k_{1-}[\text{NO}][\text{N}]_e - k_{2-}[\text{NO}][\text{O}]_e - k_{3-}[\text{NO}][\text{H}]_e \end{aligned} \quad (5.5)$$

$$\begin{aligned} \frac{d[\text{N}]}{dt} = & k_{1+}[\text{O}]_e[\text{N}_2]_e - k_{2+}[\text{N}]_e[\text{O}_2]_e - k_{3+}[\text{N}]_e[\text{OH}]_e \\ & - k_{1-}[\text{NO}][\text{N}]_e + k_{2-}[\text{NO}][\text{O}]_e + k_{3-}[\text{NO}][\text{H}]_e \end{aligned} \quad (5.6)$$

Since the concentration of nitrogen is very small compared to that of other species of interest, it is often assumed (see e.g. [34]) to be at steady state, e.g. $d[\text{N}]/dt = 0$. An algebraic solution for the nitrogen concentration may thus be derived from (5.6).

In this work a somewhat different approach is chosen: The concentration of nitrogen is assumed to be at equilibrium concentration as well. This underestimates the formation rate of NO associated with the first reaction of the Extended Zeldovich Mechanism (5.1) and it overestimates the formation rates of NO associated with the second and the third reaction, but it makes it possible to derive a linear first-order differential equation with time-varying coefficients for the concentration of NO.

The equilibrium concentrations of the species involved in the Extended Zeldovich Mechanism are calculated off-line as a function of temperature, pressure, and fuel/air equivalence ratio using the method described in Appendix C. The results are stored in lookup tables for later use.

5.3 Simplified ODE

In this section a simplified differential equation for the change in NO concentration is derived. The derivation is organized as follows:

1. Equations (5.7) to (5.9) develop an expression for the change of the concentration of NO. The terms R_c , \tilde{R}_d , and $[\text{NO}]_e$ are introduced which are independent of the actual concentration of

NO.

2. Equations (5.10) to (5.12) set up a relation between the terms R_c and \tilde{R}_d , in order to simplify the expression for the formation of NO.
3. Finally, in Eqs. (5.13) to (5.15) algebraic manipulations are used to derive a linear first-order differential equation with time-varying coefficients to describe the formation of NO.

The NO concentration is defined as:

$$[\text{NO}] = \frac{n_{\text{NO}}}{V}, \quad (5.7)$$

where n_{NO} is the number of NO molecules and V the volume of the reaction zone.

The total change of the NO concentration can be written as:

$$\begin{aligned} \frac{d[\text{NO}]}{dt} &= \frac{\frac{dn_{\text{NO}}}{dt} V - \frac{dV}{dt} n_{\text{NO}}}{V^2} \\ &= \underbrace{\frac{dn_{\text{NO}}}{dt} \frac{1}{V}}_{\left(\frac{d[\text{NO}]}{dt}\right)_f} + [\text{NO}] \frac{dV}{dt} \frac{1}{V} \end{aligned} \quad (5.8)$$

The right-hand side of (5.8) consists of two parts: A change due to the chemical formation of NO, the formation rate $\left(\frac{d[\text{NO}]}{dt}\right)_f$, and a change due to the volume change. The chemical NO formation rate can be further divided into a composition and a decomposition rate

$$\left(\frac{d[\text{NO}]}{dt}\right)_f = \left(\frac{d[\text{NO}]}{dt}\right)_c - \left(\frac{d[\text{NO}]}{dt}\right)_d, \quad (5.9)$$

where

$$\begin{aligned} \left(\frac{d[\text{NO}]}{dt}\right)_c &= k_{1+}[\text{O}]_e[\text{N}_2]_e + k_{2+}[\text{N}]_e[\text{O}_2]_e + k_{3+}[\text{N}]_e[\text{OH}]_e \\ &= R_c(p, T, \phi) \end{aligned}$$

$$\begin{aligned} \left(\frac{d[\text{NO}]}{dt}\right)_d &= k_{1-}[\text{NO}][\text{N}]_e + k_{2-}[\text{NO}][\text{O}]_e + k_{3-}[\text{NO}][\text{H}]_e \\ &= (k_{1-}[\text{N}]_e + k_{2-}[\text{O}]_e + k_{3-}[\text{H}]_e) [\text{NO}]_e \frac{[\text{NO}]}{[\text{NO}]_e} \\ &= \tilde{R}_d(p, T, \phi) \frac{[\text{NO}]}{[\text{NO}]_e}. \end{aligned}$$

The functions R_c and \tilde{R}_d depend only on pressure, temperature, and fuel/air equivalence ratio. The same applies to $[\text{NO}]_e$: The NO equilibrium concentration is a function of the pressure, the temperature, and the fuel/air equivalence ratio. Note that R_c , \tilde{R}_d , and $[\text{NO}]_e$ are independent of the current concentration of NO. This is helpful for the derivation of a relation between R_c and \tilde{R}_d as the next step.

When the NO concentration is at the equilibrium concentration $[\text{NO}]_e$, the NO composition and decomposition rates are equal:

$$\left(\frac{d[\text{NO}]}{dt}\right)_f = \left(\frac{d[\text{NO}]}{dt}\right)_c - \left(\frac{d[\text{NO}]}{dt}\right)_d = 0 \quad (5.10)$$

From this follows that

$$R_c(p, T, \phi) = \tilde{R}_d(p, T, \phi) \quad (5.11)$$

and

$$\left(\frac{d[\text{NO}]}{dt}\right)_f = R_c(p, T, \phi) \left(1 - \frac{[\text{NO}]}{[\text{NO}]_e}\right). \quad (5.12)$$

If (5.12) is inserted into (5.8), the total NO concentration change becomes

$$\frac{d[\text{NO}]}{dt} = R_c(p, T, \phi) \left(1 - \frac{[\text{NO}]}{[\text{NO}]_e} \right) \frac{1}{V} + [\text{NO}] \frac{dV}{dt} \frac{1}{V} \quad , \quad (5.13)$$

which can be reformulated to:

$$\frac{d[\text{NO}]}{dt} = \left(\frac{dV}{dt} \frac{1}{V} - \frac{R_c(p, T, \phi)}{[\text{NO}]_e} \right) [\text{NO}] + R_c(p, T, \phi) \quad (5.14)$$

In Eq. (5.14) the information on the equilibrium composition of the burned gas is used twice: (1) For the calculation of the quantity R_c and (2) for the equilibrium concentration of NO, $[\text{NO}]_e$. The equilibrium composition of the burned gas is calculated using the techniques given in detail in Appendix C. Based on those calculations, the quantity R_c and the the equilibrium concentration of NO are stored in maps as functions of the pressure, temperature, and fuel/air equivalence ratios.

In the context of this work, the reaction zone V is assumed to be the entire burned gas zone V_b . The time histories of the pressure, the temperature, and the volume of the burned gas zone are known from the calculations shown in Chaps. 3 and 4 and the fuel/air equivalence ratio is obtained from measurements. Equation (5.14) then becomes a linear first-order differential equation with time-varying coefficients:

$$\frac{d[\text{NO}]}{dt} = a(t) [\text{NO}] + b(t) \quad (5.15)$$

5.4 Steady-state Validation

The NO formation model has been validated against data found in the literature and against measured engine-out NO emissions of a 6-cylinder 3.2-liter SI engine.

Table 5.1: Comparison of the NO equilibrium concentrations calculated with different methods

p	T	NO equilibrium concentration					
		Equil. calc. [20]	Differential Equation				
[bar]	[K]	[ppm]	[50]	[9],[14]	[64],[16]	[62]	control-oriented
		[ppm]	[ppm]	[ppm]	[ppm]	[ppm]	[ppm]
10	2800	10000	10470	7870	7720	7530	9176
100	2400	1980	2170	1590	1550	1500	1884
	2600	3980	4290	3190	3190	3030	3707
	2800	7100	7580	5710	5600	5460	6506

5.4.1 Validation with Published Steady-State NO Concentrations

An overview of steady-state NO concentrations is given in [32].

First, the steady-state concentrations of NO in a constant-volume container with constant temperature and pressure are presented. The results are either achieved with a direct calculation of the NO equilibrium concentration (see Appendix C) or by solving Eq. (5.5) over a sufficiently long time interval with different sets of constants A , B , and E . The results are summarized in Table 5.1: The data shown in the third column are obtained by calculating directly the equilibrium concentrations. The results shown in the columns 4 to 7 are obtained by setting $d[\text{N}]/dt = 0$, solving (5.6) for $[\text{N}]$ and inserting the result into (5.5). The values in columns 4 to 7 are the steady-state solutions of Eq. (5.5) using different sets of constants A , B , and E , as indicated by the references. The results shown in the right-most column are obtained with the control-oriented method (5.14).

Secondly, the transient behavior of the control-oriented model is in-

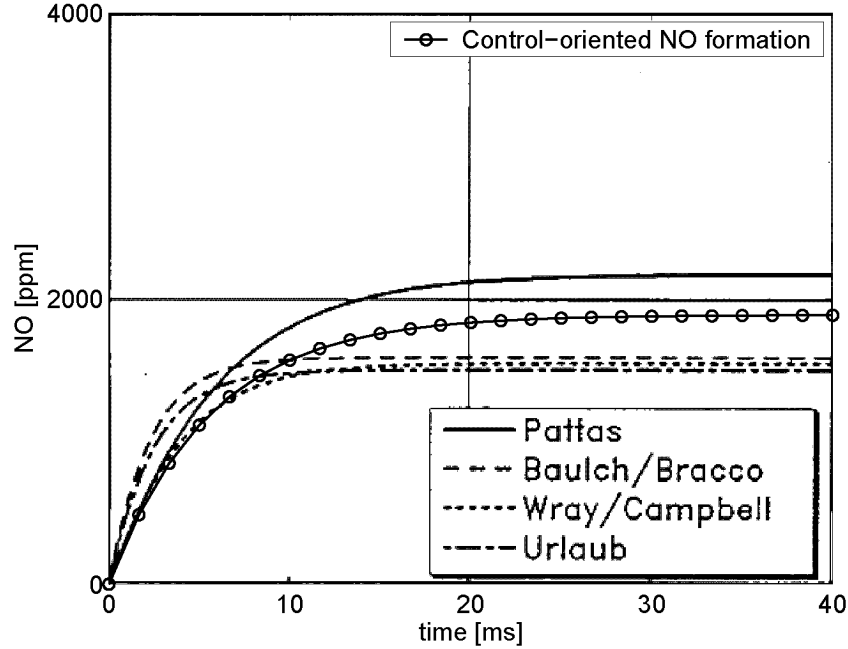


Figure 5.1: Transient NO concentration in a container at $p = 100$ bar, $T = 2400$ K, and $\phi = 1$. Data from [32] and data calculated with the control-oriented formulation of the NO formation rate are compared.

vestigated. Figure 5.1 shows an overlay of data from [32] with the transient NO concentration calculated by means of the control-oriented formulation of the NO formation.

The transient behavior of the control-oriented NO formation model is then compared to the more complete model in which the two differential equations for the formation of NO and N are solved, (5.5) and (5.6). The results for three different combinations of temperature, pressure, and fuel/air equivalence ratio are shown in the three graphs of Fig. 5.2.

The comparison of Figs. 5.1 and 5.2 clearly shows that the error introduced by simplifying the NO formation model is on the order of the variations introduced by using different sets of the constants A , B , and E .

Finally, Fig. 5.3 shows the measured and the calculated engine-out

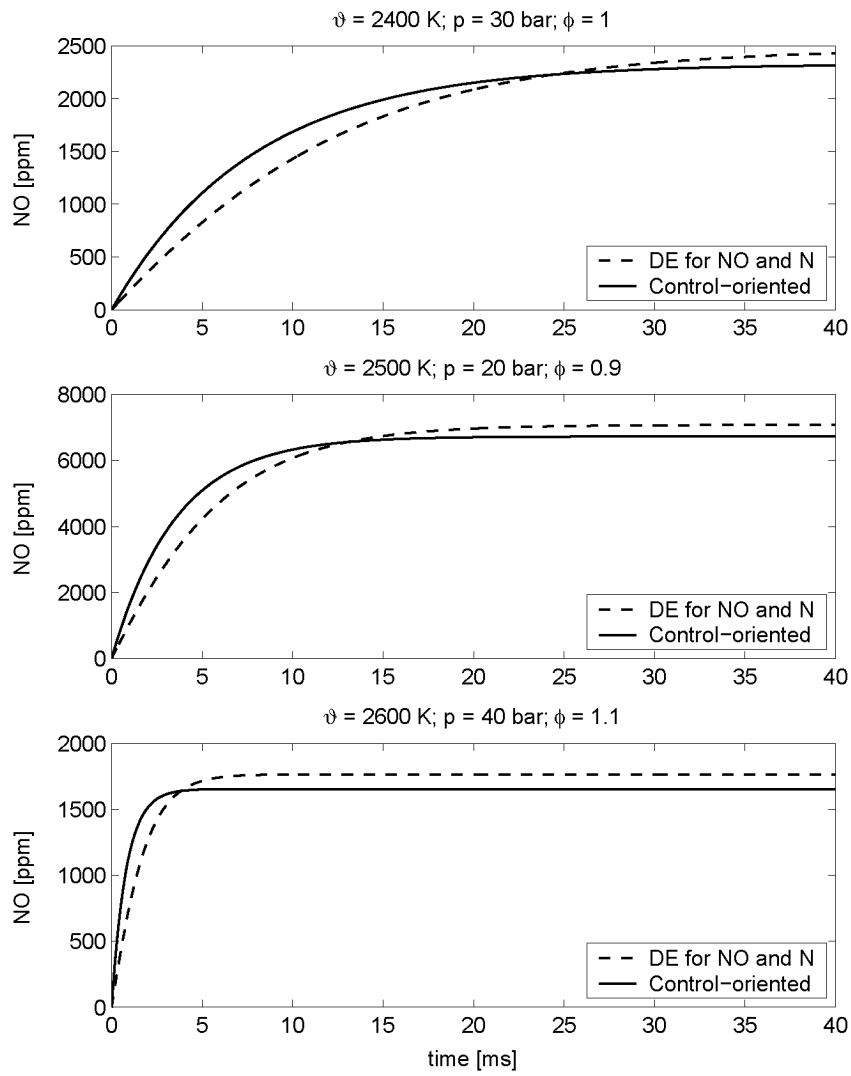


Figure 5.2: Transient NO concentrations calculated using the control-oriented NO formation model and the more complete model in Eqs. (5.5) and (5.6).

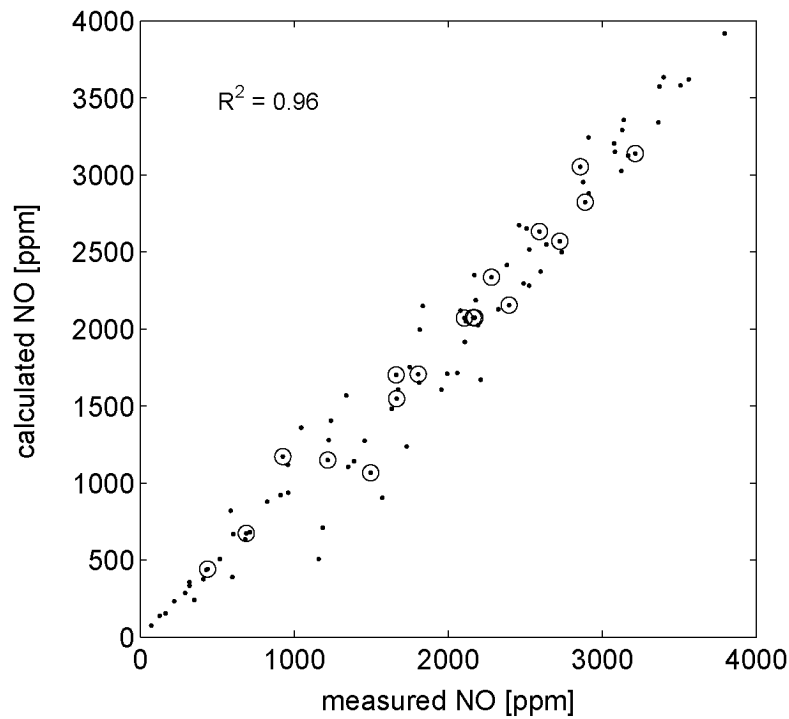


Figure 5.3: Measured and calculated engine-out NO emissions for all operating points and conditions. Data that was used for calibration is indicated by a circle. The accuracy of the estimations is documented by the correlation coefficient R , which is calculated excluding the calibration data

NO emissions for all operating points and conditions. The calculated data shown in this figure is based on the control-oriented pressure estimation, the control-oriented estimation of the burned gas temperature, and the control-oriented formulation of the NO formation. Evidently, highly accurate estimations of the engine-out NO emissions are achieved for the whole operating range considered here.

5.4.2 Sensitivity of the Formation of NO to the Burned Gas Temperature and the Initial NO Concentration

In this subsection the sensitivity of the engine-out NO emissions to the overall temperature level of the burned gas and to the initial NO concentration is investigated.

Burned Gas Temperature

On the basis of process simulations at the operating point $n = 1000$ rpm and $p_{im} = 0.50$ bar, the temperature level of the burned gas is varied by changing the lower heating value of the fuel. The resulting burned gas temperature profiles, the burned gas volumes, and the pressures are used to calculate the engine-out NO emissions. Figure 5.4 shows the sensitivity of the engine-out NO emissions to the level of the burned gas temperature, which is characterized by the maximum temperature of the burned gas $T_{b,max}$. Although the data shown in Fig. 5.4 seem to fall on a straight line, in general, the engine-out NO emissions depend in a non-linear way on the fuel/air equivalence ratio, the in-cylinder pressure, and the burned gas temperature profile. Figure 5.5 shows the profiles of the burned gas temperatures and the NO concentrations as functions of the crank angle for the same variations of the lower heating value. Evidently, the temperature of the burned gas has a strong influence on the engine-out NO emissions.

Initial Concentration of NO

So far, the initial concentration of NO at the start of combustion and its influence on the engine-out NO emissions has not been discussed.

Prior to the combustion, NO from previous cycles is contained in the residual gas and in the externally recirculated exhaust gas. There-

fore, the formation of NO starts with a non-zero initial concentration of NO.

In order to investigate the influence of the initial concentration of NO on the final value of the concentration of NO, a series of calculations were carried out, each with the same pressure and temperature profile, but with different initial NO concentrations. The results are shown in the Figs. 5.6 and 5.7.

Figure 5.6 shows that the initial concentration of NO has no effect on the engine-out NO concentration, while Fig. 5.7 shows the details of the transient concentration of NO. The profiles of the concentration start at different initial values and converge soon after the onset of the formation of NO to one common profile. The final values of the trajectories are virtually equal. The effect observed here may be explained as follows: The conditions in the burned gas soon after the onset of the combustion seem to favor the backward reaction of NO in the Zeldovich Mechanism which decreases the concentration of NO during the initial stages of the combustion. In fact, the temperature dependency of the reaction rates of the various reactions of the Zeldovich Mechanism differ among each other [34], which leads to the effect observed.

Thus, the inclusion of the initial concentration does not affect the engine-out NO emissions. It is sufficient to set the initial concentration to zero in order to avoid any additional complexity of the model.

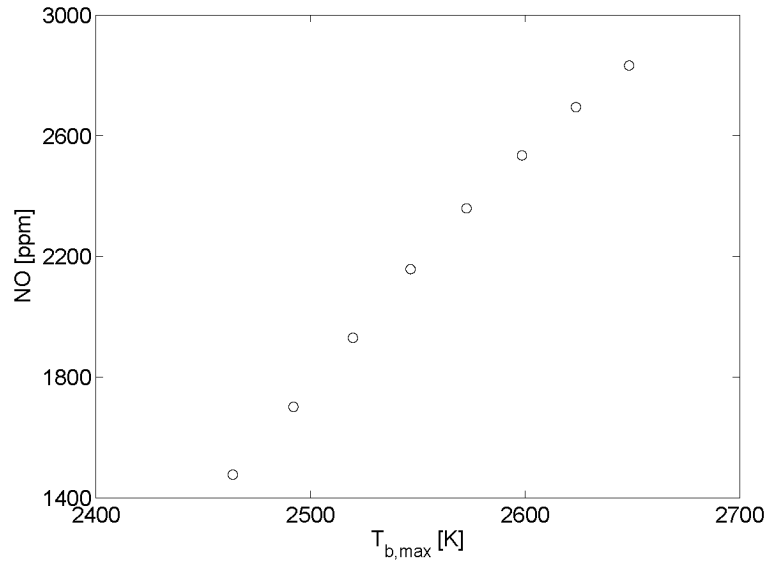


Figure 5.4: Engine-out NO concentration as functions of the maximum temperature of the burned gas

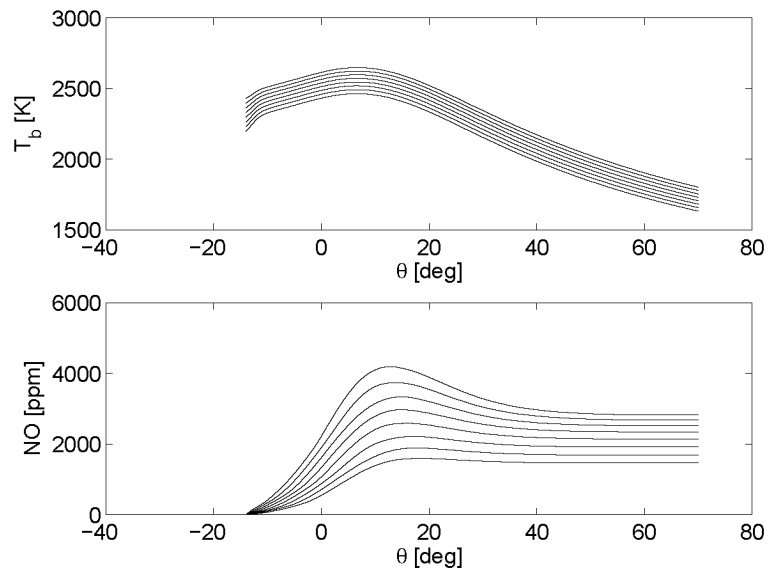


Figure 5.5: Burned gas temperature and NO concentration as functions of the crank angle for different temperature profiles

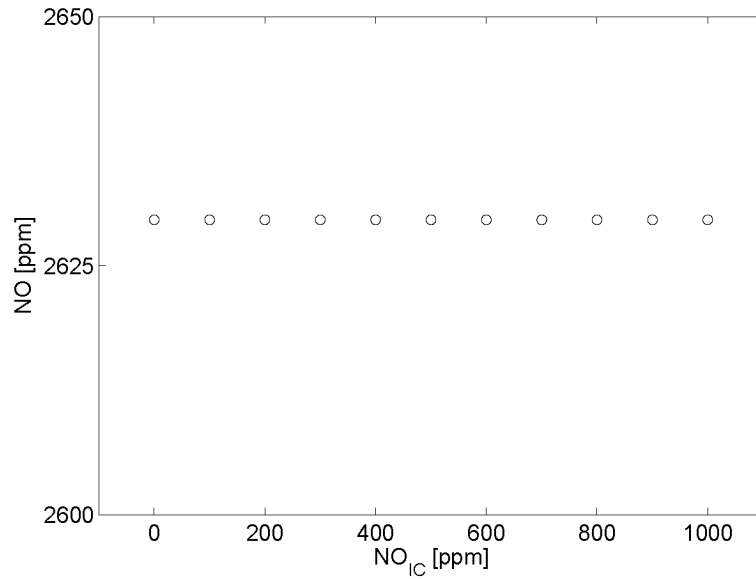


Figure 5.6: Engine-out NO concentration as functions of the initial NO concentration in the combustion chamber

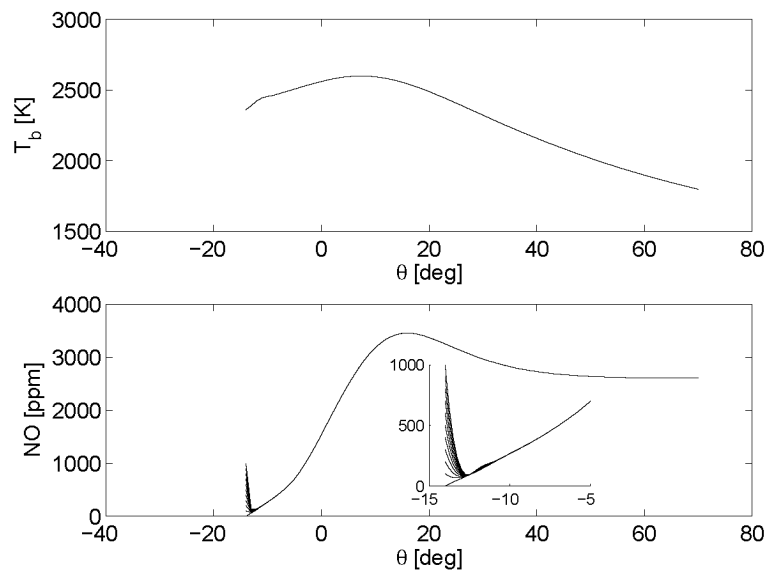


Figure 5.7: Burned gas temperature and NO concentration as functions of the crank angle for different initial NO concentrations in the combustion chamber

Chapter 6

Calculation Time

The purpose of the various submodels of the NO estimation method as developed in this work is to make NO estimation available for control purposes. Two important questions in this context are how the calculation process is organized and how much cpu time it consumes.

All calculations and simulations reported in this thesis are based on the following hardware/software configuration:

- Hardware: Compaq PC with Pentium 4 2.2 GHz processor
- Operating System: Windows XP Professional
- Matlab 6.5
- Simulink 5.1

6.1 Organization of the Calculations

Fig. 6.1 provides an overview of the calculation scheme:

During the first cycle, data is collected on the crankshaft angular velocity. During the second cycle, the NO estimation model is evalu-

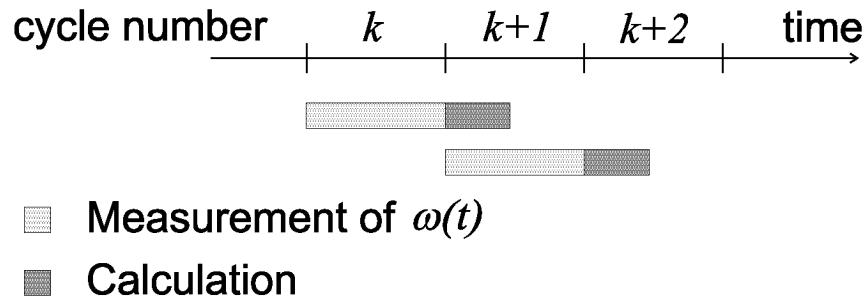


Figure 6.1: Calculation timing

ated, which involves the following: partial Fourier transformation of the measured data and calculation of the heat-release profile, of the in-cylinder pressure, of the crankshaft angular velocity and its partial Fourier transformation, of the burned gas temperature, and of the formation of the engine-out NO emissions. Parallel to the evaluation of the model, the crankshaft angular velocity is measured and made available for the next model evaluation starting at the beginning of the third cycle. All subsequent cycles repeat the same measurement and calculation pattern.

6.2 Real Time

In general the term *real time* implies that a task is processed at least at the same speed as that by which the results from the underlying process are needed. For instance, the calculation of the output of a controller has to be at least as short as the sample time at which the actuators are supplied with the newest controller output.

This applies also to the NO estimation method presented in this text. The calculation of the engine-out NO emission is achieved in a shorter time than the duration of one engine cycle (which is the "sample time"). However, there are two points that need further

comment:

1. The data acquisition process and the calculation run in parallel. The two tasks thus have to be assigned to two different processors. It is a common technique to employ a DSP (digital signal processor) for the data collection and data buffering, which can be accessed by the main processor.
2. The data acquisition covers one full engine cycle. Since the evaluation of the model cannot start until the data acquisition of the first cycle is completed. The evaluation of the model takes a fraction of a cycle, and the results are available before the start of the third cycle. This calculation scheme introduces a time delay of one cycle as described in the stability analysis in Section 3.6.1.

6.3 Detailed Calculation Time

Table 6.1 provides a summary of all the calculation times for the various submodels. Obviously, by far the most-time consuming steps are the computations of the temperature of the burned gas and of the NO formation. Both include the interpolation of the thermodynamic properties from precalculated tables.

All values of cpu time are given in milliseconds. These values have to be compared to the duration of one engine cycle: At $n = 6000$ rpm the duration of 2 crankshaft revolutions is 20 milliseconds. Clearly, the NO estimation method is able to run in parallel with the experiment without lagging behind, even for high engine speeds.

Table 6.1: Calculation time needed by the various submodels.

Submodel, Calculation Step	Equations	CPU time [ms]
Partial Fourier transformation of the measured crankshaft angular velocity	(3.36), (3.37)	0.15
Calculation of the heat release profile	(3.3) to (3.7)	0.89
Calculation of the in-cylinder pressure	(3.29), (3.30)	0.86
Calculation of the net torque	(3.32) to (3.34)	1.95
Partial Fourier transformation of the net torque	(3.36), (3.37)	0.15
Flame speed correction	(3.42) to (3.44)	~0.00
Temperature of the burned gas	(4.18), (4.22) to (4.23)	5.92
NO formation	(5.14)	3.89
Total calculation time per cycle		13.81

Chapter 7

Summary and Conclusions

A model for the engine-out NO emission of a port injected SI engine was developed and validated against measured data. The main properties of the model are:

- The model is based on physical first principles. It thus requires only few parameters to be calibrated and it allows the extrapolation of the engine-out NO emissions to operating conditions not covered by the calibration process.
- The model is formulated for control purposes. The physical first principles are used as a starting point from which the model is simplified to achieve a short simulation time.

The inputs required for the model of the NO formation process are the pressure and the temperature of the reaction zone. A simplified pressure estimation method is developed which incorporates a combustion model. The method makes use of the measured crank-

shaft angular velocity data to adapt the combustion model parameters. Furthermore, a method is developed to calculate the burned gas temperature without explicitly calculating the total mass of the cylinder charge, which avoids a main source of errors in common process simulations. A simple linear first-order differential equation for the NO formation is derived from the well-known Zeldovich Mechanism. It is easy to integrate and therefore applicable in control applications.

The new pressure estimation method is compared to a benchmark pressure estimation method. It is shown that it overcomes the observability problems at top dead center, which is common to all pressure estimation methods using the crankshaft angular velocity.

The model is validated against measured data. It proves to deliver accurate results.

The material presented in the thesis permits the observation of the course of the combustion and the calculation of important information such as in-cylinder pressure and NO formation without penetrating the combustion chamber.

The main novelties introduced in this work are

1. A physics-based process simulation and model for the formation NO have been simplified such that on-line calculations become feasible.
2. A new algorithm for the parameter adaption of the pressure estimation submodel has been developed which overcomes the loss of observability at top dead center and which is robust against disturbances.
3. The formation of NO due to the Zeldovich Mechanism is described by one single linear first-order differential equation with time-varying coefficients.

Appendix A

Step-by-Step Calibration

This appendix lists the steps necessary for the calibration of the control-oriented model for the engine-out NO emissions. Section A.1 specifies the experimental data that have to be collected, while Sect. A.2 lists a step-by-step procedure to calibrate the model parameters.

A.1 Required Experimental Data

Two sets of data have to be obtained from the engine for which the model has to be calibrated:

1. The first data set comprises measurement data obtained as the engine is running at nominal operating conditions. The operating points are distributed in a regular grid over the engine operating range of interest, e.g. the operating range that is covered by the EUDC driving cycle. These operating points are referred to as the reference operating points. Figure 2.3 shows

the arrangement of the reference operating points used in this thesis.

2. The second data set comprises measurement data obtained as the engine is running with varied spark advance settings and fuel/air equivalence ratios. For this purpose, the engine is running at an operating point centered in the operating range. The parameters spark advance θ_{sa} and fuel/air equivalence ratio ϕ are varied starting from their nominal settings. A recommended procedure is to set the spark advance to two early settings, one nominal setting, and two later settings while the fuel/air equivalence ratio is left at its nominal value (e.g. $\phi = 1$). Then the spark advance is set to the nominal setting and the fuel/air equivalence ratio is set to one rich setting, to stoichiometry ($\phi = 1$), and to three leaner settings. Figure 2.4 shows the arrangement of the parameter variations used in this thesis.

As reported in Sect. 2.4, the measured data is grouped into four sets as follows:

1. Data set **A** contains the data obtained at the reference operating points.
2. Data set **A**⁺ contains data set **A** plus one measurement per reference operating point where the spark advance is retarded.
3. Data set **B** contains all measurements acquired at fuel/air equivalence ratios and spark advance settings other than nominal settings.
4. Data set **B**⁻ contains data acquired during the spark advance and the air/fuel equivalence ratio variations at the reference operating point at $n = 2000$ rpm and $p_{im} = 0.5$ bar.

The signals that have to be recorded are summarized in Table A.1.

Table A.1: Signals required for calibration

Symbol	Signal description
$p(\theta)$	In-cylinder pressure
$\omega(\theta)$	Crankshaft angular velocity
p_{im}	Inlet manifold pressure
T_{im}	Temperature in the inlet manifold
θ_{sa}	Spark advance
ϕ	Fuel/air equivalence ratio
n	Engine speed
[NO]	NO concentration

A.2 Calibration Procedure

The parameters have to be divided in two groups: The first group consists of parameters that can be measured directly or may be obtained by calculations based on measurements. The second group consists of parameters that have to be adjusted such that measured and calculated data match in a least-squared-error sense. The first group comprises the parameters p_{im}^0 , n^0 , θ_{sa}^0 , ϕ^0 , p_1^0 , Δp^0 , and ΔC_φ^0 . The second group comprises the coefficients of f_{sa} , f_ϕ , g_{sa} , and g_ϕ and the parameters $c_{\Delta p}$, k^0 , and c_{Tad}^0 . The following list specifies for each parameter the calibration method and the calibration data set.

p_{im}^0 , n^0 , θ_{sa}^0 , ϕ^0 These parameters are taken directly from data set **A**. The parameters p_{im}^0 and n^0 denote the reference operating points. The spark advance θ_{sa}^0 and the fuel/air equivalence ratio ϕ^0 are the nominal operating conditions at the reference operating points. All four parameters are stored in the reference map.

p_1^0 , Δp^0 The pressures p_1^0 at 80 degrees before TDC and p_2^0 at 80

degrees after TDC are interpolated from the measured in-cylinder pressure $p(\theta)$ contained in the data set \mathbf{A} . The difference $\Delta p^0 = p_2^0 - p_1^0$ and the value of p_1^0 are stored in the reference map.

ΔC_φ^0

In order to calibrate ΔC_φ^0 , the phase at the engine firing frequency of the instantaneous crankshaft angular velocity $\hat{\varphi}_\omega^0$ has to be calculated for each operating point in the data set \mathbf{A} . Additionally, the phase at the engine firing frequency has to be calculated based on the measured crankshaft angular velocity φ_ω^0 . Comparing the measured and calculated phases yields $\Delta C_\varphi^0 = \varphi_\omega^0 - \hat{\varphi}_\omega^0$.

Coefficients of f_{sa} , f_ϕ , g_{sa} , g_ϕ The coefficients of these polynomials have to be adjusted such that the calculated in-cylinder pressure matches the measured in-cylinder pressure in the least-squared-error sense.

The in-cylinder pressure is calculated on the basis of Eqs. (3.3), (3.6), (3.7), and (3.29) for each operating condition contained in data set \mathbf{B}^- . Then the calculated in-cylinder pressure is compared to the measured in-cylinder pressure to form the cost function

$$J = \sum_k \left(\sum_{\theta=-80}^{+80} (p_{\text{meas}}(\theta) - p_{\text{calc}}(\theta))^2 \right),$$

where k is the measurement number in data set \mathbf{B}^- and θ runs from 80 degrees before TDC to 80 degrees after TDC. Standard optimization techniques are used to find the coefficients of f_{sa} , f_ϕ , g_{sa} , and g_ϕ such that J is minimized.

k^0 , c_{Tad}^0 These parameters are calibrated such that the calculated engine-out NO emissions match the measure engine-out NO emissions in the least-squared-error sense.

The temperature and the volume of the burned gas are calculated using Eqs. (4.10), (4.23), and (4.25). Based on the pressure, the temperature, and the volume of the burned gas zone as well as the fuel/air equivalence ratio, the engine-out NO emissions can be computed using Eq. (5.14). The engine-out NO emissions are calculated for each operating point in data set \mathbf{A}^+ . Calculated and measured engine-out NO emission levels are compared to form the cost function

$$J = \sum_k (\langle \text{NO} \rangle_{meas} - \langle \text{NO} \rangle_{calc})^2 ,$$

where k is the measurement number in data set \mathbf{A}^+ . Standard optimization techniques are used to find k^0 and c_{Tad}^0 such that J is minimized.

Appendix B

Heat-release Analysis

Heat-release analysis and process simulation are closely interconnected. While the former allows the calculation of the heat released due to combustion from measured in-cylinder pressure, the latter does the opposite; it calculates the pressure from a given heat-release trace. In this appendix the mathematical formulation of a 0-dimensional 1-zone process simulation model is given. The corresponding equations can be used either for the in-cylinder pressure or for the burned mass fraction, which represents a normalized form of the heat release. The formulation of the model is based on [47] and is given as a summary here. The model given below is formulated only for the high-pressure part of the cycle, although conceptually it is not limited to it. Note that for an accurate estimate of the initial conditions such as residual gas mass and charge temperature, the gas exchange has to be included.

The model has three state variables: The temperature T , the pressure p , and the burned mass fraction x_b . Assuming a premixed charge, the burned mass fraction x_b is proportional to the heat released due to combustion and to the mass fraction of the charge that has been

burned. The burned mass fraction x_b ranges from 0 at the start of the combustion to 1 for a completed combustion¹. For the mathematical formulation given below, the burned mass fraction is a known function of the crank angle θ . For the two other state variables, T and p , two differential equations can be given.

$$dU = dQ_{ht} + dW + \sum_{i \neq j} dm_{ij} h_j \quad (\text{B.1})$$

$$pdV + Vdp = dmRT + mdRT + mRdT \quad (\text{B.2})$$

Equation (B.1) states the energy conservation for an open system. This approach has been chosen because the unburned mass is assumed to escape through a virtual port and to be replaced by the corresponding burned mass during the course of the combustion. In Eq. (B.1) the variables dU , dQ_{ht} , and dW are the change of the internal energy, the heat transfer to the cylinder wall, and the change of work done on the piston, respectively, while dm_{ij} is the mass flow from volume j to i . The latter is used for the virtual replacement of the unburned mass by the burned mass. The variable h_j is the specific enthalpy associated with the mass flow dm_{ij} .

Equation (B.2) is the total derivative of the ideal gas law and is used here as a differential equation for the pressure. The variables p , V , m , R , and T are the in-cylinder pressure, the cylinder volume, the total mass of the charge, the gas constant, and the charge temperature, respectively.

The change of the internal energy has to be detailed as given below:

¹Here, x_b describes the progress of the combustion and is independent of the residual gas mass fraction x_r . The influence of x_r on the amount of heat released during combustion as well as on the thermodynamic properties of the unburned gas is incorporated in the thermodynamic properties

$$dU = dm u + m du \quad (\text{B.3})$$

$$du = d(x_b u_b + (1 - x_b) u_u) \quad (\text{B.4})$$

$$\begin{aligned} &= dx_b (u_b - u_u) \dots \\ &+ x_b \left(\underbrace{\left(\frac{\partial u_b}{\partial T} \right)}_a dT + \underbrace{\left(\frac{\partial u_b}{\partial p} \right)}_b dp \right) \dots \\ &+ (1 - x_b) \left(\underbrace{\left(\frac{\partial u_u}{\partial T} \right)}_c dT + \underbrace{\left(\frac{\partial u_u}{\partial p} \right)}_d dp \right) \end{aligned}$$

As mentioned above, the model is formulated for the high-pressure part of the cycle only. Assuming negligible blow-by, the mass of the cylinder charge remains unchanged and therefore $dm = 0$. The partial derivatives of the specific internal energy can be expressed by the specific enthalpy and the gas constant and their partial derivatives. This is convenient, because most thermodynamic data is available for the specific enthalpy, while the gas constant can be calculated from the molar mass of the species. The relations are taken from [27] and are given below:

$$\left(\frac{\partial u_i}{\partial p} \right)_{T_i} = -\frac{T_i^2}{p} \left(\frac{\partial R_i}{\partial T_i} \right)_p - T_i \left(\frac{\partial R_i}{\partial p} \right)_{T_i} \quad (\text{B.5})$$

$$\left(\frac{\partial u_i}{\partial T_i} \right)_p = \left(\frac{\partial h_i}{\partial T_i} \right)_p - R_i - T_i \left(\frac{\partial R_i}{\partial T_i} \right)_p \quad (\text{B.6})$$

A widely used assumption is that the composition of the unburned gas is "frozen" and that therefore $\frac{\partial R_u}{\partial T}$, $\frac{\partial R_u}{\partial p}$, and $\frac{\partial u_u}{\partial p}$ are zero.

The virtual enthalpy transport connected to the mass flows dm_{ij}

can be written as shown below. For the specific enthalpies h_b and h_u absolute values including the enthalpy of formation are used. Doing so, the heat released due to the chemical reactions is represented here as the virtual exchange of the unburned gas mass by the burned gas mass.

$$\sum_{i \neq j} dm_{ij} h_{ij} = dx m (h_b - h_u) \quad (\text{B.7})$$

The heat transfer dQ_{ht} to the cylinder wall is calculated based on Woschni's heat transfer correlation (4.10), which is here for convenience:

$$\begin{aligned} \frac{dQ_{ht}}{dt} &= A h_c (T - T_w) \\ h_c &= C_0 B^{-0.2} (p_f \cdot 10^{-5})^{0.8} T^{-0.53} c_{char}^{0.8} \\ c_{char} &= C_1 c_m + C_2 \frac{V_d T_{ivc}}{V_{ivc} p_{ivc}} (p_f - p_m) \end{aligned}$$

Finally the work term in equation (B.1) is given by:

$$dW = -pdV \quad (\text{B.8})$$

In equation (B.2) the gas constant R can be detailed as follows. Again, the composition of the unburned gas is assumed to be "frozen" with the consequences mentioned above.

$$R = x_b R_b + (1 - x_u) R_u \quad (\text{B.9})$$

$$\begin{aligned} dR &= x_b \left(\left(\frac{\partial R_b}{\partial T} \right) dT + \left(\frac{\partial R_b}{\partial p} \right) dp \right) \dots \\ &+ (1 - x_b) \left(\left(\frac{\partial R_u}{\partial T} \right) dT + \left(\frac{\partial R_u}{\partial p} \right) dp \right) \dots \\ &+ dx (R_b - R_u) \end{aligned} \quad (\text{B.10})$$

In summary, the following set of equations can be written:

$$\begin{aligned}
 & mx_b(adT + bdp) + m(1 - x_b)cdT \\
 & + mdx(h_b - R_bT - h_u + R_uT) = dQ_{ht} - dW \quad (\text{B.11})
 \end{aligned}$$

$$\begin{aligned}
 & mT x_b \left(\left(\frac{\partial R_b}{\partial T} \right) dT + \left(\frac{\partial R_b}{\partial p} \right) dp \right) \\
 & \quad + mT dx_b (R_b - R_u) \dots \\
 & + m(x_b R_b + (1 - x_b) R_u) dT = pdV + Vdp \quad (\text{B.12})
 \end{aligned}$$

Finally the model can be grouped into a matrix equation to yield the 0-dimensional 1-zone process simulation model

$$\mathbf{A}_{PS} \begin{pmatrix} dT \\ dp \end{pmatrix} = \mathbf{B}_{PS} \quad (\text{B.13})$$

or the corresponding heat-release analysis model

$$\mathbf{A}_{HR} \begin{pmatrix} dT \\ dx \end{pmatrix} = \mathbf{B}_{HR} \quad (\text{B.14})$$

The capabilities of the model are shown in Figure B.1 for a sample operating point.

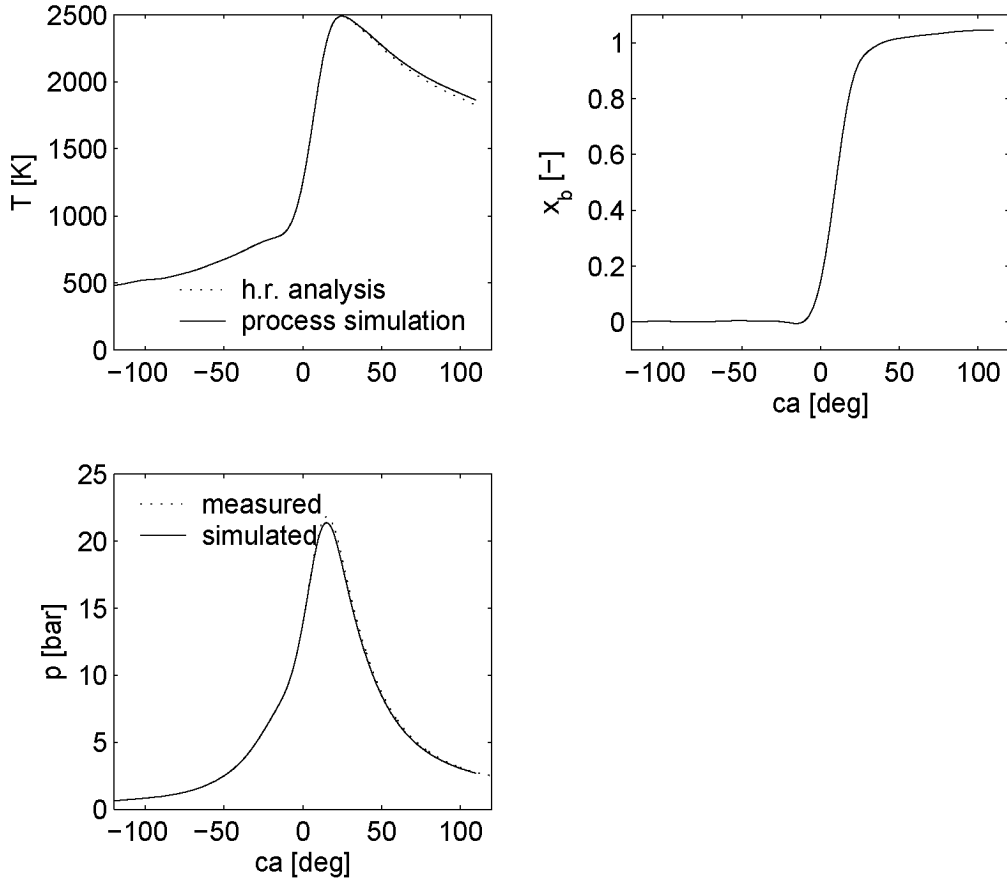


Figure B.1: The figure shows results from a heat-release analysis and process simulation for an operating point at engine speed of 2000 rpm and inlet manifold pressure of 0.5 bar. The measured in-cylinder pressure shown in the lower left graph is taken as the basis to calculate the burned mass fraction x_b shown in the right graph using the heat-release model (B.14). Then the mass burned fraction x_b is taken to calculate the in-cylinder pressure and the temperature using the process simulation model (B.13). The simulated pressure is compared to the measured pressure in the lower left graph, the temperature calculated during the heat-release analysis is compared to the temperature calculated during the process simulation in the upper left graph.

Appendix C

Thermodynamic Properties

The thermodynamic properties and the composition of the burned and of the unburned gas are essential for the process simulation and the calculation of the engine-out NO emissions. The approach here is to calculate the equilibrium composition and the thermodynamic properties of the burned gas independently of the process simulation for a range of pressures p , temperatures T , and fuel/air equivalence ratios ϕ and to store the results in maps. Later calculations can rely on these maps and interpolate appropriate values.

The calculation of the thermodynamic properties and the composition of the gas is carried out using the program package CHEPP (CHEMical Equilibrium Program Package) [24]. Other well-known codes for the calculation of the equilibrium composition and the thermodynamic properties of a mixture of gases are the NASA code [28] and the STANJAN code [54]. An early work has been published by Olikara and Borman [48]. Keck developed a method for the calcu-

lation of rate-constrained equilibrium composition of a mixture of species [38]. The techniques applied are the minimization of the Gibbs free energy or the Helmholtz energy [28], [24], the element-potential method [54], or the calculation of the equilibrium of a postulated set of reactions [48].

This appendix summarizes the technique of the minimization of the Gibbs free energy. Furthermore, an analysis of the sensitivity of the solution to the temperature, the pressure, the fuel/air equivalence ratio, and the air humidity is presented.

Thermodynamic properties of interest are the specific heat c_p , the specific enthalpy h , the specific entropy s , and the gas constant R . Furthermore, the derivatives $\frac{\partial h}{\partial p}$, $\frac{\partial R}{\partial T}$, and $\frac{\partial R}{\partial p}$ are often needed. These thermodynamic properties build the basis from which all other thermodynamic properties can be calculated. For the calculation of the formation rate of NO, the equilibrium concentration of N, N₂, NO, O, O₂, OH, and H are of particular interest (see Sect. 5.3).

The burned and unburned gas in the cylinder of a combustion engine is a mixture of different species. In particular, the burned gas consists of dozens of different species, among which only the most important can be considered here. For most applications, it is sufficient to consider $m = 12$ species: O, O₂, H, H₂, OH, H₂O, CO, CO₂, N, NO, NO₂, and N₂. In this appendix j will be used as the index for the species. A corner stone for the calculation of the thermodynamic properties is the atom balance, which will be discussed further below in detail. The reactants and products of the global combustion reactions are all assumed to consist only of $l = 4$ different types of atoms: C, O, H, N. The total numbers of each type of atoms remain constant, which leads to four atom balances. The text of this appendix will refer to the atoms using the index i .

The thermodynamic properties of the gas are calculated as the weighted average of the thermodynamic properties of the species. This

makes it necessary to know the numeric value of the property of each species as well as the exact composition of the gas. As an example, the mole specific and the mass specific enthalpy can be calculated as:

$$\tilde{h} = \sum_j \tilde{h}_j \tilde{x}_j, \quad h = \sum_j h_j x_j,$$

where \tilde{h}_j is the mole specific, h_j the mass specific enthalpy, \tilde{x}_j the mole fraction, and x_j the mass fraction of species j .

Similarly, the derivatives of the thermodynamic properties can be calculated. The derivative of the mole specific enthalpy with respect to the pressure is given as an example:

$$\frac{d\tilde{h}}{dp} = \sum_j \frac{d\tilde{h}_j}{dp} \tilde{x}_j + \tilde{h}_j \frac{d\tilde{x}_j}{dp} \quad (\text{C.1})$$

Likewise, the derivative of the mass specific enthalpy with respect to the pressure can be calculated:

$$\frac{dh}{dp} = \sum_j \frac{dh_j}{dp} x_j + h_j \frac{dx_j}{dp} \quad (\text{C.2})$$

C.1 Properties of a Single Species

The thermodynamic properties of single species have been measured by many scientists. Their data is available in a vast number of tables. The calculations at hand are based on the GRI-Mech¹ tables, because they are readily available and contain a consistent set of data for the

¹GRI-Mech data can be found on the internet following the link http://www.me.berkeley.edu/gri_mech

purpose at hand. The data is given in polynomial form:

$$\frac{\tilde{c}_p}{\tilde{R}} = a_1 + a_2T + a_3T^2 + a_4T^3 + a_5T^4 \quad (\text{C.3})$$

$$\frac{\tilde{h}}{\tilde{R}T} = a_1 + a_2T/2 + a_3T^2/3 + a_4T^3/4 + a_5T^4/5 + a_6/T \quad (\text{C.4})$$

$$\frac{\tilde{s}^0}{\tilde{R}} = a_1 \ln(T) + a_2T + a_3T^2/2 + a_4T^3/3 + a_5T^4/4 + a_7 \quad (\text{C.5})$$

The gas constant R_j of species j can be calculated from the molecular mass M_j and the universal gas constant $\tilde{R} = 8314 \text{ (kJ kmol}^{-1}\text{K}^{-1}\text{)}$

$$R_j = \frac{\tilde{R}}{M_j}. \quad (\text{C.6})$$

The entropy as a function of temperature and pressure is given as:

$$\tilde{s}(T, p) = \tilde{s}^0(T) - \tilde{R} \ln\left(\frac{p}{p^0}\right) \quad (\text{C.7})$$

C.2 Mole and Mass Specific Properties

The thermodynamic properties of a mixture of gases can be calculated as mole specific or mass specific properties. The following example for the enthalpy is given:

$$\bar{h} = \sum_j x_j h_j \quad (\text{C.8})$$

$$\tilde{h} = \sum_j \tilde{x}_j \tilde{h}_j \quad (\text{C.9})$$

Here, values with the accent \sim are mole specific and values without decoration are mass specific values. The accent $\bar{}$ denotes a weighted average. The enthalpy is denoted with h and the mole or mass fraction with x . The conversion from mole specific to mass specific values is

done according to:

$$h_j = \tilde{h}_j \frac{1}{M_j} \quad (\text{C.10})$$

$$x_j = \frac{\tilde{x}_j M_j}{\sum_k \tilde{x}_k M_k} \quad (\text{C.11})$$

Based thereon, the mass specific properties of the gas mixture may be calculated from mole specific properties of the gas components:

$$\bar{h} = \frac{1}{\sum_k \tilde{x}_k M_k} \sum_j \tilde{x}_j \tilde{h}_j \quad (\text{C.12})$$

C.3 Gibbs Function

The Gibbs free energy is defined as:

$$\tilde{g}(T, p) = \tilde{h}(T) - \tilde{s}(T, p)T \quad (\text{C.13})$$

A mixture of gas with z_j moles of the species j minimizes the Gibbs function G

$$G = \sum_j \tilde{g}_j z_j \quad (\text{C.14})$$

at the chemical equilibrium. By taking into account that $z = \sum_j z_j$ and $z_j/z = p_j/p$, the above equation can be expanded to yield the basis for the calculation of the equilibrium composition of the gas:

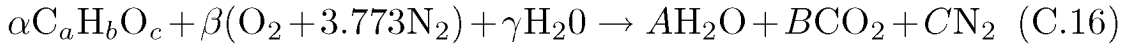
$$\begin{aligned} G &= \sum_j \left(\tilde{h}_j(T) - T\tilde{s}_j^0(T) + \tilde{R}T \ln \frac{p_j}{p^0} \right) n_i \\ &= \sum_j \left(\tilde{h}_j(T) - T\tilde{s}_j^0(T) + \tilde{R}T \ln \frac{p}{p^0} + \tilde{R}T \ln \frac{z_j}{z} \right) z_j \end{aligned} \quad (\text{C.15})$$

By specifying the fuel/air equivalence ratio ϕ , the air humidity χ , and the type of fuel, the constraints for z_j are introduced: The

mole numbers have to comply with the atom balance defined by these specifications. The next section will introduce the atom balance for the combustion gases.

C.4 Atom Balance

The global chemical reaction during the combustion of a fuel with humid air can be written as:



Note that there is no oxygen, CO, or HC on the product side, which indicates that the above reaction is stoichiometric. Furthermore, "ideal" combustion is assumed, which means that the products consist only of CO₂, H₂O, and N₂. Setting $\beta = 1$, and letting γ be a measure of the air humidity, the coefficients α , A , B , and C are defined as:

$$\begin{aligned} B &= \frac{2\gamma(2a - c) + b(2\beta + \gamma)}{b + 2(2a - c)} \\ \alpha &= \frac{2}{b} (B - \gamma) \\ A &= \frac{2a}{b} (B - \gamma) \\ C &= 3.773 \end{aligned} \quad (C.17)$$

In Table C.1 the water content of air at $\chi = 100\%$ relative air humidity is given. The last column, γ was calculated (assuming $\beta = 1$) as

$$\gamma = \beta m_{H_2O, max} \frac{M_{air}}{M_{H_2O}}, \quad (C.18)$$

where $m_{H_2O, max}$ is the mass of water in the air at 100% relative air humidity, and M_{air} and M_{H_2O} are the molecular masses of dry air and of water, respectively. For the temperature range covered by Table

Table C.1: Mass of water contained in 1 kg air at 100% relative air humidity and at a pressure of 1 atm

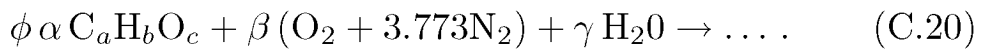
T [C°]	Mass of H ₂ O per kg dry air: $m_{\text{H}_2\text{O},max}$ [g]	γ
50	88.12	0.1425
40	49.81	0.0805
30	27.69	0.0448
20	14.85	0.0240
10	7.76	0.0125
0	3.84	0.0062

C.1, the following expression is a good fit for γ :

$$\gamma = \beta \chi 2.578 \cdot 10^{-10} e^{0.0625T} \quad (\text{C.19})$$

In the expression (C.19), the temperature T is given in Kelvin and the relative air humidity χ is within the interval $[0, 1]$.

Proceeding further, the global reaction for off-stoichiometric combustion can be rewritten as



From this equation the total number of the atoms C, O, H, and N can be computed, where the relation between α and β is determined using (C.17).

$$\begin{aligned} n_C &= \phi \alpha a \\ n_O &= \phi \alpha c + 2 + \gamma \\ n_H &= \phi \alpha b + 2\gamma \\ n_N &= 2 \cdot 3.773 \end{aligned} \quad (\text{C.21})$$

The total number of C, O, H, and N atoms does not change during the reaction. This adds four constraints to the minimization of the Gibbs function (C.15). The matrix formulation below states the four atom balances:

$$\mathbf{Az} = \mathbf{b} \tag{C.22}$$

$$\mathbf{A} = \begin{bmatrix} a_{1,1} & a_{1,2} & \cdots & a_{1,m} \\ a_{2,1} & \ddots & & \\ \vdots & & & \\ a_{l,1} & \cdots & \cdots & a_{l,m} \end{bmatrix} \quad \mathbf{z} = \begin{bmatrix} z_1 \\ \vdots \\ z_m \end{bmatrix} \quad \mathbf{b} = \begin{bmatrix} n_{\text{C}} \\ n_{\text{O}} \\ n_{\text{H}} \\ n_{\text{N}} \end{bmatrix}$$

The elements a_{ij} of matrix \mathbf{A} count the number of atoms i in the species j .

The next section shows how the constraints enforced by the atom balances are integrated in the procedure of minimizing the Gibbs function.

C.5 Composition of the Gas

C.5.1 Unburned Gas

In the case of the unburned gas, its composition is considered as "frozen". The thermodynamic properties can be calculated according to the composition of the products as given in (C.20).

C.5.2 Burned Gas

For the calculation of the equilibrium concentration of the species in the burned gas, the Lagrange multiplier approach can be used. The problem statement is formulated as follows:

The Gibbs function G has to be minimized subject to the constraints imposed by the atom balances, which leads to the following

set of equations to be solved:

$$\begin{aligned}\frac{\partial G}{\partial z_j} + \sum_i \lambda_i a_{ij} &= 0 \\ n_i - \sum_j a_{ij} z_j &= 0 \\ \sum_j z_j &= z\end{aligned}\tag{C.23}$$

The first equation can be written m times; once for each species j in the burned gas. The second equation can be written $l = 4$ times; once for the balance of atom i . The last of the three equations states that all species together add up to the total number of species, which is used to calculate G (see Eq. C.15). In this way a set of $m + 4 + 1$ equations has to be solved for the m mole numbers z_j , the 4 Lagrange multipliers λ_i , and the total mole number z of the species. The mole fractions \tilde{x}_j follow from the mole numbers z_j :

$$\tilde{x}_j = \frac{z_j}{\sum_k z_k}\tag{C.24}$$

The equilibrium concentration $c_{e,j}$ of the species j in units kmol m^{-3} is then given as

$$c_{e,j} = \frac{p}{\tilde{R}T} \tilde{x}_j$$

The vector containing the mole numbers z_j which satisfy the set of equations (C.23) is denoted by $\mathbf{z}^* = [z_1^*, z_2^*, \dots, z_m^*]^T$. In the next section algebraic expressions for the sensitivity of the solution \mathbf{z}^* to pressure, temperature, fuel/air equivalence ratio, and air humidity changes are derived.

C.6 Sensitivity of the Equilibrium Composition

Besides the mole number \mathbf{z}^* at the equilibrium of the burned gas, the derivatives of the equilibrium composition with respect to the temperature, the pressure, the fuel/air equivalence ratio, and the air humidity, $\frac{d\mathbf{z}}{dT}$, $\frac{d\mathbf{z}}{dp}$, $\frac{d\mathbf{z}}{d\phi}$, $\frac{d\mathbf{z}}{d\gamma}$, are of interest as well.

Since the magnitude of the mole fractions varies from 10^{-9} to 10^{-1} , it is challenging to calculate the derivatives of the mole numbers z_j^* numerically. Therefore an analytical expression is derived. While the analytical expressions of the derivatives with respect to temperature and pressure have been presented in earlier publications, an analytical expression of the derivative with respect to fuel/air equivalence ratio is rarely used and found e.g. in [48]. In this thesis, a new development of the derivatives of the equilibrium concentration of a mixture of species with respect to the fuel/air equivalence ratio and the air humidity is proposed.

In Sect. C.5 the mole numbers at the equilibrium of the burned gas \mathbf{z}^* (for convenience, the asterisk $*$ indicating equilibrium will be omitted in the remainder of this section) were found by minimizing the Gibbs function $G(\mathbf{z}, p, T)$, subject to the constraints $\mathbf{A}\mathbf{z} = \mathbf{b}(\phi, \gamma)$. Since the constraints are linear, it is possible to express a set of l dependent mole numbers \mathbf{z}_2 by a set of $m - l$ independent mole numbers \mathbf{z}_1 :

$$[\mathbf{A}_1 \quad \mathbf{A}_2] \begin{bmatrix} \mathbf{z}_1 \\ \mathbf{z}_2 \end{bmatrix} = \mathbf{b}(\phi, \gamma) \quad (\text{C.25})$$

$$\mathbf{z}_2 = \mathbf{A}_2^{-1} [\mathbf{b}(\phi, \gamma) - \mathbf{A}_1 \mathbf{z}_1] \quad (\text{C.26})$$

Now the following function is defined:

$$\mathbf{h} = \mathbf{A}_2^{-1} [\mathbf{b}(\phi, \gamma) - \mathbf{A}_1 \mathbf{z}_1] \quad (\text{C.27})$$

The problem can be reformulated to an unconstrained search of the minimum of the Gibbs function $G(\mathbf{z}_1, \mathbf{h}(\mathbf{z}_1, \phi, \gamma), p, T)$. A comment on \mathbf{A}_2 is in order: \mathbf{A}_2 is of dimension $l \times l$. Since the columns of \mathbf{A} , and therefore also of \mathbf{A}_2 describe the composition of the different species, they have to be linearly independent and thus \mathbf{A}_2^{-1} exists.

At the equilibrium concentration, the derivatives of G with respect to the mole fractions vanish:

$$\frac{\partial G}{\partial \mathbf{z}_1} = 0 \quad (\text{C.28})$$

This equation has to hold, even if pressure, temperature, fuel/air equivalence ratio, or air humidity are changed by small amounts away from the values for which the equilibrium concentration was calculated:

$$d \frac{\partial G}{\partial \mathbf{z}_1} = 0 \quad (\text{C.29})$$

This equation expands to

$$d \left(\frac{\partial G}{\partial \mathbf{z}_1} + \frac{\partial G}{\partial \mathbf{h}} \frac{\partial \mathbf{h}}{\partial \mathbf{z}_1} \right) = 0 \quad (\text{C.30})$$

and further to

$$\begin{aligned}
& \left[\frac{\partial^2 G}{\partial \mathbf{z}_1^2} + \frac{\partial^2 G}{\partial \mathbf{h} \partial \mathbf{z}_1} \frac{\partial \mathbf{h}}{\partial \mathbf{z}_1} + \frac{\partial G}{\partial \mathbf{h}} \frac{\partial^2 \mathbf{h}}{\partial \mathbf{z}_1^2} \right] d\mathbf{z}_1 + \\
& \left[\frac{\partial^2 G}{\partial \mathbf{z}_1 \partial \phi} + \frac{\partial^2 G}{\partial \mathbf{h} \partial \phi} \frac{\partial \mathbf{h}}{\partial \mathbf{z}_1} + \frac{\partial G}{\partial \mathbf{h}} \frac{\partial^2 \mathbf{h}}{\partial \mathbf{z}_1 \partial \phi} \right] d\phi + \\
& \left[\frac{\partial^2 G}{\partial \mathbf{z}_1 \partial \gamma} + \frac{\partial^2 G}{\partial \mathbf{h} \partial \gamma} \frac{\partial \mathbf{h}}{\partial \mathbf{z}_1} + \frac{\partial G}{\partial \mathbf{h}} \frac{\partial^2 \mathbf{h}}{\partial \mathbf{z}_1 \partial \gamma} \right] d\gamma + \\
& \left[\frac{\partial^2 G}{\partial \mathbf{z}_1 \partial p} + \frac{\partial^2 G}{\partial \mathbf{h} \partial p} \frac{\partial \mathbf{h}}{\partial \mathbf{z}_1} + \frac{\partial G}{\partial \mathbf{h}} \frac{\partial^2 \mathbf{h}}{\partial \mathbf{z}_1 \partial p} \right] dp + \\
& \left[\frac{\partial^2 G}{\partial \mathbf{z}_1 \partial T} + \frac{\partial^2 G}{\partial \mathbf{h} \partial T} \frac{\partial \mathbf{h}}{\partial \mathbf{z}_1} + \frac{\partial G}{\partial \mathbf{h}} \frac{\partial^2 \mathbf{h}}{\partial \mathbf{z}_1 \partial T} \right] dT = 0
\end{aligned} \tag{C.31}$$

The second derivatives of the function \mathbf{h} vanish. All other terms are given below. For convenience some substitutions are defined.

$$\tilde{g}_j(T) = \tilde{h}_j(T) - T\tilde{s}_j^0(T) \tag{C.32}$$

$$S = \sum_{j=1}^{m-l} z_j + \sum_{i=1}^l h_i \tag{C.33}$$

The mole specific enthalpy \tilde{h}_j has to be carefully distinguished from the constraint h_i imposed by the atom balance i (C.27).

$$\begin{aligned}
G(\mathbf{z}_1, \mathbf{h}(\mathbf{z}_1, \phi, \gamma), p, T) &= \sum_{j=1}^{m-l} \left[\tilde{g}_j(T) + \tilde{R}T \ln \frac{p}{p_0} + \tilde{R}T \ln \frac{z_j}{S} \right] z_j \\
&+ \sum_{i=1}^l \left[\tilde{g}_i(T) + \tilde{R}T \ln \frac{p}{p_0} + \tilde{R}T \ln \frac{h_i}{S} \right] h_i
\end{aligned}$$

$$\frac{\partial G}{\partial z_k} = \tilde{R}T \left[1 + \ln \frac{p}{p_0} + \ln \frac{z_k}{S} - \sum_{j=1}^{m-l} \left[\frac{z_j}{S} \right] - \sum_{i=1}^l \left[\frac{h_i}{S} \right] \right] + \tilde{g}_k(T)$$

$$\frac{\partial G}{\partial h_k} = \tilde{R}T \left[1 + \ln \frac{p}{p_0} + \ln \frac{h_k}{S} - \sum_{j=1}^{m-l} \left[\frac{z_j}{S} \right] - \sum_{i=1}^l \left[\frac{h_i}{S} \right] \right] + \tilde{g}_k(T)$$

$$\frac{\partial \mathbf{h}}{\partial \mathbf{z}_1} = -\mathbf{A}_2^{-1} \mathbf{A}_1$$

$$\frac{\partial^2 G}{\partial z_k \partial z_q} = \tilde{R}T \sum_{j=1}^{m-l} \left[\frac{z_j}{S^2} \right] + \tilde{R}T \sum_{i=1}^l \left[\frac{h_i}{S^2} \right] + \tilde{R}T \begin{cases} -\frac{2}{S} & \text{for } k \neq q \\ \frac{1}{z_q} - \frac{2}{S} & \text{for } k = q \end{cases}$$

$$\frac{\partial^2 G}{\partial z_k \partial \phi} = -\tilde{R}T \frac{\partial S}{\partial \phi} + \tilde{R}T \sum_{j=1}^{m-l} \left[\frac{z_j \frac{\partial S}{\partial \phi}}{S^2} \right] + \tilde{R}T \sum_{i=1}^l \left[\frac{h_i \frac{\partial S}{\partial \phi}}{S^2} \right]$$

The vector $\mathbf{K} = \mathbf{A}_2^{-1} \frac{\partial \mathbf{b}}{\partial \phi}$ with elements K_i is defined. Then $\frac{\partial S}{\partial \phi} = \sum_{i=1}^l K_i$.

$$\frac{\partial^2 G}{\partial z_k \partial \gamma} = -\tilde{R}T \frac{\partial S}{\partial \gamma} + \tilde{R}T \sum_{j=1}^{m-l} \left[\frac{z_j \frac{\partial S}{\partial \gamma}}{S^2} \right] + \tilde{R}T \sum_{i=1}^l \left[\frac{h_i \frac{\partial S}{\partial \gamma}}{S^2} \right]$$

The vector $\mathbf{L} = \mathbf{A}_2^{-1} \frac{\partial \mathbf{b}}{\partial \gamma}$ with elements L_i is defined. Then $\frac{\partial S}{\partial \gamma} = \sum_{i=1}^l L_i$.

$$\frac{\partial^2 G}{\partial z_k \partial p} = \tilde{R}T \frac{1}{p}$$

$$\frac{\partial^2 G}{\partial z_k \partial T} = \tilde{R} \left[1 + \ln \frac{p}{p_0} + \ln \frac{z_k}{S} - \sum_{j=1}^{m-l} \left[\frac{z_j}{S} \right] - \sum_{i=1}^l \left[\frac{h_i}{S} \right] \right] + \frac{\partial}{\partial T} \tilde{g}_k(T)$$

$$\frac{\partial^2 G}{\partial h_k \partial z_q} = \tilde{R}T \left[\frac{\frac{\partial h_k}{\partial z_q}}{h_k} - \frac{2}{S} - \sum_{i=1}^l \left[\frac{\frac{\partial h_i}{\partial z_q} S - h_i}{S^2} \right] + \sum_{j=1}^{m-l} \left[\frac{z_j}{S^2} \right] \right]$$

The matrix $\mathbf{M} = -\mathbf{A}_2^{-1} \mathbf{A}_1$ with elements M_{ij} is defined. Then $\frac{\partial h_i}{\partial z_q} = M_{iq}$ and $\frac{\partial S}{\partial z_q} = 1 + \sum_{i=1}^l M_{iq}$.

$$\frac{\partial^2 G}{\partial h_k \partial \phi} = \tilde{R}T \frac{\frac{\partial h_k}{\partial \phi} S - \frac{\partial S}{\partial \phi} h_k}{S h_k} - \tilde{R}T \sum_{i=1}^l \left[\frac{\frac{\partial h_i}{\partial \phi} S - \frac{\partial S}{\partial \phi} h_i}{S^2} \right] + \tilde{R}T \sum_{j=1}^{m-l} \left[\frac{z_j \frac{\partial S}{\partial \phi}}{S^2} \right]$$

The vector $\mathbf{N} = \mathbf{A}_2^{-1} \frac{\partial \mathbf{b}}{\partial \phi}$ with elements N_i is defined. Then $\frac{\partial h_i}{\partial \phi} = N_i$ and $\frac{\partial S}{\partial \phi} = \sum_{i=1}^l N_i$.

$$\frac{\partial^2 G}{\partial h_k \partial \gamma} = \tilde{R}T \frac{\frac{\partial h_k}{\partial \gamma} S - \frac{\partial S}{\partial \gamma} h_k}{S h_k} - \tilde{R}T \sum_{i=1}^l \left[\frac{\frac{\partial h_i}{\partial \gamma} S - \frac{\partial S}{\partial \gamma} h_i}{S^2} \right] + \tilde{R}T \sum_{j=1}^{m-l} \left[\frac{z_j \frac{\partial S}{\partial \gamma}}{S^2} \right]$$

The vector $\mathbf{P} = \mathbf{A}_2^{-1} \frac{\partial \mathbf{b}}{\partial \gamma}$ with elements P_i is defined. Then $\frac{\partial h_i}{\partial \gamma} = P_i$ and $\frac{\partial S}{\partial \gamma} = \sum_{i=1}^l P_i$.

$$\frac{\partial G}{\partial h_k \partial p} = \tilde{R}T \frac{1}{p}$$

$$\frac{\partial^2 G}{\partial h_k \partial T} = \tilde{R} \left[1 + \ln \frac{p}{p_0} + \ln \frac{h_k}{S} - \sum_{i=1}^l \left[\frac{h_i}{S} \right] - \sum_{j=1}^{m-l} \left[\frac{z_j}{S} \right] \right] + \frac{\partial}{\partial T} \tilde{g}_k(T)$$

With this, all partial derivatives are known. They make it possible to calculate $\frac{d\mathbf{z}_1}{dT}$, $\frac{d\mathbf{z}_1}{dp}$, $\frac{d\mathbf{z}_1}{d\phi}$, and $\frac{d\mathbf{z}_1}{d\gamma}$ based on the Gibbs function G , the constraints expressed by h , and the known equilibrium mole numbers \mathbf{z}_1^* . For this purpose Eq. (C.31) is solved for the derivatives $\frac{d\mathbf{z}_1}{dp}$, $\frac{d\mathbf{z}_1}{dT}$, $\frac{d\mathbf{z}_1}{d\phi}$, or $\frac{d\mathbf{z}_1}{d\gamma}$ and appropriate values for p , T , ϕ , and γ are inserted.

The sensitivities of the dependent mole fractions \mathbf{z}_2^* can be calculated using the full derivative of the constraint function $\mathbf{h}(\mathbf{z}_1, \phi, \gamma)$:

$$d\mathbf{z}_2 = \mathbf{A}_2^{-1} \frac{\partial \mathbf{b}}{\partial \phi} d\phi + \mathbf{A}_2^{-1} \frac{\partial \mathbf{b}}{\partial \gamma} d\gamma - \mathbf{A}_2^{-1} \mathbf{A}_1 d\mathbf{z}_1$$

In order to calculate the change of the mole or mass specific thermodynamic properties of the gas as indicated in (C.1) and (C.2), the changes of the mole or mass fractions have to be known. The mole and mass fractions are defined as:

$$\begin{aligned} \tilde{x}_k &= \frac{z_k}{\sum_{j=1}^m z_j} \\ x_k &= \frac{M_k z_k}{\sum_{j=1}^m M_j z_j} = \frac{M_k \tilde{x}_k}{\sum_{j=1}^m M_j \tilde{x}_j} \end{aligned} \quad (\text{C.34})$$

The changes of the mole and mass fractions are calculated as follows:

$$\begin{aligned} d\tilde{x}_k &= \frac{dz_k \sum_{j=1}^m z_j - z_k \sum_{j=1}^m dz_j}{\left(\sum_{j=1}^m z_j\right)^2} \\ dx_k &= \frac{M_k dz_k \sum_{j=1}^m M_j z_j - M_k z_k \sum_{j=1}^m M_j dz_j}{\left(\sum_{j=1}^m M_j z_j\right)^2} \\ &= \frac{M_k d\tilde{x}_k \sum_{j=1}^m M_j \tilde{x}_j - M_k \tilde{x}_k \sum_{j=1}^m M_j d\tilde{x}_j}{\left(\sum_{j=1}^m M_j \tilde{x}_j\right)^2} \end{aligned} \quad (\text{C.35})$$

Bibliography

- [1] S. M. Aceves, D. L. Flowers, C. K. Westbrook, J. R. Smith, W. Pitz, R. Dibble, M. Christensen, and B. Johansson. A Multi-Zone Model for Prediction of HCCI Combustion and Emissions. *SAE 2000-01-0552*, 2000.
- [2] J. Ackermann. *Abtastregelung*. Springer-Verlag, Berlin, Heidelberg, New York, 1988.
- [3] K. Allmendinger, L. Guzzella, A. Seiler, and O. Loffeld. A Method to Reduce the Calculation Time for an Internal Combustion Engine Model. *SAE 2001-01-0574*, 2001.
- [4] I. Andersson and L. Eriksson. Ion Sensing for Combustion Stability Control of a Spark-Ignited, Direct-Injected Engine. *SAE 2000-01-0552*, 2000.
- [5] I. Arsie, F. Marotta, C. Pianese, and G. Rizzo. Information Based Selection of Neural Networks Training Data for S.I. Engine Mapping. *SAE 2001-01-0561*, 2001.
- [6] C. M. Atkinson, T. W. Long, and E. L. Hanzevack. Virtual sensing: A Neural Network-Based Intelligent Performance and Emissions Prediction System for On-Board Diagnostics and Engine Control. *SAE 980516*, 1998.

- [7] P. M. Azzoni, G. Minelli, D. Moro, R. Flora, and G. Serra. Indicated and Load Torque Estimation using Crankshaft Angular Velocity Measurement. *SAE 1999-01-543*, 1999.
- [8] J. K. Ball, M. J. Bowe, C. R. Stone, and P. D. McFadden. Torque Estimation and Misfire Detection using Block Angular Acceleration. *SAE 2000-01-0560*, 2000.
- [9] D. L. Baulch, D. D. Drysdale, D. G. Horne, and A. C. Lloyd. High Temperature Reaction Rate Data. Technical Report No. 4, University of Leeds, 1969.
- [10] P. N. Blumberg. Nitric Oxide Emissions From Stratified Charge Engines: Prediction and Control. *Combustion Science and Technology*, 8:pp. 5 – 24, 1973.
- [11] P. N. Blumberg and J. T. Kummer. Prediction of NO Formation in Spark-Ignited Engines – An Analysis of Methods of Control. *Combustion Science and Technology*, 4:pp. 73 – 95, 1971.
- [12] G. L. Borman and K. W. Ragland. *Combustion Engineering*. McGraw-Hill, Boston, 1998.
- [13] C. T. Bowan. Mechanism and Modelling of Nitrogen Chemistry in Combustion. *Progress in Energy and Combustion Science*, 15:287–338, 1989.
- [14] F. V. Bracco. Nitric Oxide Formation in Droplet Diffusion Flames. *Proceedings of the Fourteenth International Symposium on Combustion*, *The Combustion Institute*, page 831, 1973.
- [15] D. Brand, C. H. Onder, and L. Guzzella. Estimation of the Instantaneous In-Cylinder Pressure for Control Purposes using Crankshaft Angular Velocity. *SAE 2005-01-0228*, 2005.

- [16] I. M. Campbell. Reactivity of Hydrogen to Atomic Nitrogen and Atomic Oxygen. *Trans. Faraday Soc.*, 64:265, 1968.
- [17] S. X. Chen and J. J. Moskwa. Application of Nonlinear Sliding-Mode Observer for Cylinder Pressure Reconstruction. *Control Engineering Practice*, 5(8):1115–1121, 1997.
- [18] P. Csallner. *Eine Methode zur Vorausberechnung der Aenderung des Brennverlaufes von Ottomotoren bei geänderten Betriebsbedingungen*. Dissertation, TU München, 1981.
- [19] P. Csallner and G. Woschni. Zur Vorausberechnung des Brennverlaufes von Ottomotoren bei geänderten Betriebsbedingungen. *MTZ Motortechnische Zeitschrift*, 43/1982:195 –200, 1982.
- [20] P. De Jaegher. *Das thermodynamische Gleichgewicht von Verbrennungsgasen unter Berücksichtigung der Russbildung*. Dissertation, TU Graz, 1976.
- [21] C. De Petris, S. Diana, V. Giglio, S. Golini, and G. Police. Numerical Simulation of Combustion in Premixed SI Engines using Fractal Flame Models. *SAE 952383*, 1995.
- [22] S. Diana, V. Giglio, B. Iorio, and G. Police. A Model-Based Evaluation of Emissions for Manifold-injected SI Engines. *SAE 2000-01-0955*, 2000.
- [23] W. D. Erickson and R. K. Prabhu. Rapid Computation of Chemical Equilibrium Composition: An Application to Hydrocarbon Combustion. *AIChE American Institute of Chemical Engineers Journal*, 32(7):1079–1087, 1986.
- [24] L. Eriksson. CHEPP – A CHEMical Equilibrium Program Package for Matlab. *SAE 2004-01-1460*, 2004.

- [25] L. Eriksson and I. Andersson. An Analytic Model for Cylinder Pressure in a Four-Stroke SI Engine. *SAE 2002-01-0371*, 2002.
- [26] L. Eriksson and L. Nielsen. Towards On-Board Engine Calibration with Feedback Control Incorporating Combustion Models and Ion-sense. *Automatisierungstechnik*, 5:204 – 212, 2003.
- [27] C. B. P. Finn. *Thermal Physics*. Stanley Thornes Ltd, second edition, 1998.
- [28] S. Gordon and B. J. McBride. Computer Program for Calculation of Complex Chemical Equilibrium Compositions and Applications: I Analysis. *NASA Reference Publication 1311*, 1994.
- [29] Y. Guezennec and P. Gyan. A Novel Approach to Real-Time Estimation of the Individual Cylinder Combustion Pressure for S.I. Engine Control. *SAE 1999-01-0209*, 1999.
- [30] P. Gyan, S. Ginoux, J.-C. Champoussin, and Y. Guezennec. Crankangle Based Torque Estimation: Mechanistic/Stochastic. *SAE 2000-01-0559*, 2000.
- [31] M. Hafner. Model-Based Determination of Dynamic Engine Control Function Parameters. *SAE 2001-01-1981*, 2001.
- [32] G. Heider. *Rechenmodell zur Vorausrechnung der NO-Emission von Dieselmotoren*. Dissertation, Technische Universität München, 1996.
- [33] M. Henn and U. Kiencke. Estimation of In-Cylinder-Pressure Torque from Angular Speed by Kalman Filtering. *Preprints of the First IFAC-Workshop on Advances in Automotive Control*, pages 20–25, 1995.
- [34] J. B. Heywood. *Internal Combustion Engine Fundamentals*. McGraw-Hill, 1988.

- [35] S. D. Hires, R. J. Tabaczynski, and J. M. Novak. The Prediction of Ignition Delay and Combustion Intervals for a Homogeneous Charge, Spark Ignition Engine. *SAE 780232*, 1978.
- [36] M. Kao and J. J. Moskwa. Nonlinear Cylinder and Intake Manifold Pressure Observers for Engine Control and Diagnostics. *SAE 940375*, 1994.
- [37] M. H. Kao and J. J. Moskwa. Nonlinear Diesel-Engine Control and Cylinder Pressure Observation. *Journal of Dynamic Systems Measurement and Control—Transactions of the ASME*, 117(2):183–192, 1995.
- [38] J. C. Keck. Rate-controlled constrained-equilibrium theory of chemical reactions in complex systems. *Progress in Energy and Combustion Science*, 16(2):125–154, 1990.
- [39] T. Koch, K. Schänzlin, and K. Boulouchos. Characterization and phenomenological modelling of mixture formation and combustion in a direct injection spark ignition engine. *SAE 2002-01-1138*, 2002.
- [40] H. C. Krijnsen, R. B. Van Leeuwen, C. M. Van den Bleek, and H. P. A. Calis. Optimum NOx abatement in diesel exhaust using inferential feedforward reductant control. *Fuel*, 80:1001–1008, 2001.
- [41] G. A. Lavoie and P. N. Blumberg. Measurements of NO Emissions From a Stratified Charge Engine: Comparison of Theory and Experiment. *Combustion Science and Technology*, Vol 8:pp. 25 – 37, 1973.
- [42] G. A. Lavoie and P. N. Blumberg. A Fundamental Model for Predicting Fuel Consumption, NOx and HC Emissions of the Con-

- ventional Spark-Ignited Engine. *Combustion Science and Technology*, 21, 1980.
- [43] G. A. Lavoie, J. B. Heywood, and J. C. Keck. Experimental and Theoretical Study of Nitric Oxide Formation in Internal Combustion Engines. *Combustion Science and Technology*, 1:pp. 313 – 326, 1970.
- [44] F. A. Matekunas. Modes and Measures of Cyclic Combustion Variability. *SAE 830337*, 1983.
- [45] M. Mladek. *Cylinder Pressure for Control Purposes of Spark Ignition Engines*. Diss. ETH Nr. 14916, ETH Zürich, Zürich, 2003.
- [46] C. Y. Mo, A. J. Beaumont, and N. N. Powell. Active Control of Driveability. *SAE 960046*, 1996.
- [47] Y. Nilsson and L. Eriksson. A new Formulation of Multi-Zone Combustion Engine Models. In *Proc. IFAC Workshop - Advances in Automotive Control*, Karlsruhe, 2001.
- [48] C. Olikara and G. L. Borman. A Computer Program for Calculating Properties of Equilibrium Combustion Products with some Applications to I.C. Engines. *SAE 750468*, 1975.
- [49] P. J. O'Rourke. *The KIVA computer-program for multidimensional chemically reactive fluid-flows with fuel sprays*, volume 241. Springer Verlag, Berlin, 1985.
- [50] K. Pattas and G. Häfner. Stickoxidbildung bei der otto-motorischen Verbrennung. *MTZ Motortechnische Zeitschrift*, 34/1973:397 – 404, 1973.
- [51] R. R. Raine, L. Wyszynski, and R. Stone. Modelling of NO emissions from homogeneous and stratified charge spark ignition

- engines. *Proceedings of the Institution of Mechanical Engineers Part D – Journal of Automobile Engineering*, 216(5):403–412, 2002.
- [52] J. I. Ramos. *Internal Combustion Engine Modeling*. Hemisphere Publishing, New York, 1989.
- [53] M. G. Rassweiler and L. Withrow. Motion Pictures of Engine Flames Correlated with Pressure Cards. *SAE 800131*, 1980.
- [54] W. C. Reynolds. The element potential method for chemical equilibrium analysis. Implementation in the interactive program STANJAN. Technical report, Department of Mechanical Engineering, Stanford University, 1986.
- [55] G. Rizzoni. Estimate of Indicated Torque from Crankshaft Speed Fluctuations: A Model for the Dynamics of the IC Engine. *IEEE Transactions on Vehicular Technology*, 38(3):168 – 179, 1989.
- [56] M. Rublewski and J. B. Heywood. Modeling NO Formation in Spark Ignition Engines with a Layered Adiabatic Core and Combustion Inefficiency Routine. *SAE 2001-01-1011*, 2001.
- [57] Y. Shiao and J. J. Moskwa. Misfire Detection and Cylinder Pressure Reconstruction for SI Engines. *SAE 940144*, 1994.
- [58] Y. Shiao and J. J. Moskwa. Cylinder Pressure and Combustion Heat Release Estimation for SI Engine Diagnostics Using Non-linear Sliding Observers. *IEEE Transactions on Control Systems Technology*, 3(1):70–78, 1995.
- [59] J. R. Sodré. Modelling NOx emissions from spark-ignition engines. *Proceedings of the Institution of Mechanical Engineers Part D – Journal of Automobile Engineering*, 214(8):929–934, 2000.

- [60] M. Steyskal, D. Olsen, and B. Willson. Development of PEMS Models for Predicting NO_x Emissions from Large Bore Natural Gas Engines. *SAE 2001-01-1914*, 2001.
- [61] M. L. Traver, R. J. Atkinson, and C. M. Atkinson. Neural Network-Based Diesel Engine Emissions Prediction using In-Cylinder Combustion Pressure. *SAE 1999-01-1532*, 1999.
- [62] A. Urlaub. *Verbrennungsmotoren*, volume 2. Springer Verlag, Berlin, Heidelberg, New York, 1987.
- [63] G. Woschni. A Universally Applicable Equation for the Instantaneous Heat Transfer Coefficient in the Internal Combustion Engine. *SAE 670331*, 1967.
- [64] K. L. Wray and J. D. Teare. Shock-Tube Study of the Kinetics of Nitric Oxide at High Temperatures. *Journal of Chemical Physics* 36, 10:2582–2596, 1962.
- [65] Y. B. Zeldovich. The Oxidation of Nitrogen in Combustion Explosions. *Acta Physicochimica U.S.S.R.*, 21:577–628, 1946.
- [66] H. Zhao, P. Calnan, N. Ladommatos, and T. Ma. Development of an Engine Simulation Program and its Application to Stratified Charge SI Engines. *Int. Journal of Vehicle Design*, 22(3/4):159–194, 1999.

Curriculum Vitae

Personal data

Name	Daniel Brand
Date of birth	March 3, 1973
Parents	Hansrudolf Brand, Elisabeth Brand-Scheidegger

Education

1980-1984	Primary school, Langnau, Switzerland
1984-1988	Secondary school, Langnau, Switzerland
1988-1993	Gymnasium Bern-Neufeld, Bern, Switzerland
1993	Matura certificate, type B
1994	Military service
1994-2000	Studies in Mechanical Engineering, Swiss Federal Institute of Technology (ETH), Zurich, Switzerland
2000	Diploma as <i>Dipl. Masch.-Ing. ETH</i>
2000-2005	Doctoral student and research/teaching assistant at the Measurement and Control Laboratory, Swiss Federal Institute of Technology (ETH), Zurich, Switzerland.